Tidal flat thermodynamics

Jeffrey Paul Rinehimer Jr.

A dissertation
submitted in partial fulfillment of the
requirements for the degree of

Doctor of Philosophy

University of Washington

2013

Reading Committee:

James M Thomson, Chair

Alex Horner-Devine

Christopher Chickadel

Program Authorized to Offer Degree:
Civil and Environmental Engineering

University of Washington

Abstract

Tidal flat thermodynamics

Jeffrey Paul Rinehimer Jr.

Chair of the Supervisory Committee:
Asst. Professor James M Thomson
Civil and Environmental Engineering

Intertidal flats are important coastal margin environments linking the terrestrial and marine ecosystems. This dissertation studies the thermodynamic processes of tidal flats over tidal, fortnightly, and seasonal timescales through in situ field observations, remotely sensed measurements, and a numerical model of cross-flat tidal heat and mass transport.

First, seasonal variation of sediment-water heat exchange is modeled at both sites using a numerical cross-shore model of tidal flat heat and mass fluxes. The model uses a convective heat transfer coefficient to evaluate sediment-water heat fluxes. The model accurately predicts water and sediment temperatures observed at both sites and estimates that exchange of heat between the sediment and water can be as great as 20% of the incoming forcing solar shortwave radiation. Seasonal variations in the net heat flux show that the tidal flats act as a net source of heat during the summer months and a net sink during the winter. This pattern is explained by the phasing of the exposure periods and daytime solar radiation whereby maximum flat exposure during the summer occurs during the daytime whereas flat exposure during the winter months occurs at night allowing significant cooling of the flats. The model is most

sensitive to the choice of thermal conductivity indicating the importance of accurately determining tidal flat sediment thermal properties.

Next, tidal time-scales are examined by focusing on heating at the leading edge of the flooding front. Field observations indicate that during the summer under clear sky conditions, the leading edge of the flood front is nearly 5°C warmer than the sediment it inundates. Model results show that this process is related to the absorption of solar radiation in a thin film of water occurring at the front edge. This result only occurs under conditions where the light extinction coefficient is large enough to fully absorb all shortwave radiation in the water column and prevent its transmission to the sediment bed and is consistent with the qualitative observations of high turbidity at the leading edge of the front.

Finally, tidal time-scale processes on the ebb tide are studied using novel remote sensing technique to determine surface fluxes in an incised intertidal channel. Ebb flows through incised channels off the flat continue throughout the low tide period and are difficult to measure as water depths are below 10 cm. A infrared imaging technique is used to determine surface velocities during these low depth periods. Flows off the flats exhibit two distinct dynamic regimes: ebb-tide flow and post-ebb discharge. Ebb-tidal flow occurs during the receding tide when downstream water elevations control the upstream flow velocities (M1 profiles). The post-ebb discharge continues throughout the low tide period and obeys uniform open-channel flow dynamics. Calculations of total volume fluxes and the use of the tidal heat flux model support the hypothesis that remnant water from the flat surface is the source of these discharges.

TABLE OF CONTENTS

LIST OF FIGURES

LIST OF TABLES

ACKNOWLEDGMENTS

Firstly, I'd like to thank my advisor, Jim Thomson. Without his guidance and support little of this research would have been accomplished. His advice and enthusiasm for science provided me with the motivation to complete this dissertation. My committee members Chris Chickadel, Alexander Horner-Devine, Andrea Ogston, and James Riley provided excellent insight and commentary on my approach and results.

I've appreciated the support and camaraderie from the other graduate students and postdocs from the EFM group over my four years here. Many thanks to Maggie Averner, Abbas Hooshmand, Maggie McKeon, Dan Nowacki, and Stefan Talke. Special thanks to my office mates for putting up with random outbursts of frustration at various pieces of software and for accepting donations of "excess" vegetables from the garden: Roxanne Carini, Joe Graber, Mike Schwendeman, Seth Zippel, and especially Chris Bassett - his (somewhat justified) abhorrence of the default `jet` colormap in Matlab will ensure that I never use it again.

I'm also grateful for the friendships I've made outside of the lab. Rachel and Siggi Cherem, Corey and Terra Evans, Michael Hotz, Liz Manrao, Sarah McMenamin, and Andrew Wagner have all helped to keep me sane and remember that there is life outside of science (even if most you are physicists...).

None of the field work could have been accomplished without the field technicians in the AIRS Department. Alex de Klerk, Joe Talbert, and Dan Clark designed, built,

tested, and deployed all of the instrument systems used in this study. Very little would be accomplished in the field without their hard work and advice. Evan Williams (WHOI) graciously provided assistance with data collection using Britt Raubenheimer and Steve Elgar's (WHOI) LiDAR system.

I was graciously funded by the Office of Naval Research grant N000141010215, the Henry L. Gray Memorial Scholarship, and National Defense Industries Association (NDIA) fellowship. Outside data sources like the WSU AgWeathernet, METAR reports, and USGS LiDAR surveys provided invaluable baseline datasets. Our work as scientists would be immeasurable harder without organizations such as these.

The support of my parents, Jeff and Rita Rinehimer, has been instrumental in my success throughout my life. I'd especially like to thank my brother, Jared Rinehimer, who helped me settle into Seattle and provided an outline through which to vent about the world. Finally I'd like to thank my best friend and wife, Megan Rinehimer, whose love, support, and counseling kept me moving forward and whose smiling face kept me laughing.

DEDICATION

To Mrs. Nancy Reddig and Mr. Richard Pillion, my high school math teachers, who laid the foundation for my passion for math and science. "It's a great day for math!"

Chapter 1

INTRODUCTION

1.1 Motivation

Tidal flats are a common feature of estuaries and coastlines worldwide. Characterized by large intertidal areas with significant sediment supply and strong tidal forcing relative to wave forcing, these regions contain high levels of benthic microalgal biomass and production, which supply the base of coastal food webs (Colijn and de Jonge, 1984). Tidal flats are important habitats for migratory birds, commercially valuable young fishes such as salmon, and highly productive bivalve fisheries. Tidal flats also present significant navigational hazards for ships entering coastal ports and provide much of the area for land reclamation projects.

While much research has been focused on tidal flat hydrodynamics, sediment transport, and morphodynamics (See Amos, 1995; Friedrichs, 2012, for reviews.), thermodynamics in these systems has been little studied. Water temperatures often control rates of biogeochemical processes like nutrient cycling and primary productivity (Guarini et al., 1997). Alternating inundation and exposure of large regions of tidal flats creates large daily temperature variations. Johnson (1965) found that organisms living in the top 1 cm of the sediment bed of intertidal environments can experience daily temperature variations 3 times greater than those in subtidal environments, while infuana at 10 cm depth experienced daily temperatures variations as those in subtidal areas. The differences between the thermodynamic properties of

water and sediments may also play an important role in local climate and weather (Cho et al., 2000). Additionally, an understanding of the local heat budgets of these systems is important when determining the impacts of significant sources of thermal pollution such as nuclear power facilities. (Yanagi et al., 2005). This dissertation will determine sediment-water heat fluxes at tidal flats over seasonal and tidal timescales using both field measurements and a numerical model to further our understanding of the thermal environment of these regions.

1.2 Background

The heat energy H of a material defined with zero energy at absolute zero temperature is defined as

$$H = c_p \rho T = c_V T \tag{1.1}$$

where c_p is the specific heat capacity, ρ is the density, T is the temperature in Kelvin. In studies of fluids, volumetric properties are often easier to measure and manipulate in equations and hence we define the volumetric heat capacity $c_V = c_p \rho$. Assuming no internal heat source or sink the time rate of change of heat energy is dependent on the fluxes of heat through the bounding surface ∂V by

$$\frac{dH}{dt} = \int_V c_V \frac{dT}{dt} dV = \int_{\partial V} -\vec{q} \cdot \vec{n} ds \tag{1.2}$$

where $\vec{q}$ is the vector field of heat flux and $\vec{n}$ is the outward normal of surface ∂V.

Fourier's Law describes the conduction of heat through a material based on it's intrinsic thermal conductivity λ and the temperature gradient within the material ∇T as

$$\vec{q} = -\lambda \nabla T \tag{1.3}$$

where $\vec{q}$ is the time rate of heat transfer. Combining Eq. 1.2 with Eq. 1.3 and applying the divergence theorem to the right hand side yields

$$\frac{dH}{dt} = \int_V c_V \frac{dT}{dt} dV = \int_V \nabla \cdot (\lambda \nabla T)\, dV \tag{1.4}$$

This integral must apply over any surface within the volume and hence vanishes, and assuming a constant k, becomes the heat or diffusion equation

$$\frac{dT}{dt} = \kappa \nabla^2 T \tag{1.5}$$

where ∇^2 is the Laplacian and $\kappa = \lambda / c_V$ is the thermal diffusivity. In one-dimension, this is simply:

$$\frac{dT}{dt} = \kappa \frac{d^2 T}{dx^2} \tag{1.6}$$

1.2.1 Sediment thermal properties

While the heat equation (Eq. 1.6) is well studied and understood, the difficulty in applying it to tidal flat sediments lies in determining the thermal properties (conductivity, diffusivity, and heat capacity) of the sediment bed which is a complex matrix of water and organic and inorganic particles. Thermal properties of tidal flat sediments primarily depend on porosity, water content, sediment size, and mineralogy. Lovell (1985) concluded that the bulk thermal conductivity λ of saturated marine sediments was well modeled by the geometric mean of the conductivities weighted by the porosity, i.e.

$$\lambda = \lambda_s^{(1-n)} \lambda_f^n \tag{1.7}$$

where n is the porosity and λ_s and λ_f are the conductivities of the solid and fluid fractions. Miselis et al. (2012) found that, despite differences in thermal conductivities of dry sediments due to varying mineralogy and grain size, the bulk conductivity

of sediment-water mixtures was driven mainly by the porosity and resulting water content of the sediments. This is due mainly to the large difference in mineral and water conductivities. For standard quartz minerals, λ_s=8.6 W m^{-1} K^{-1} while freshwater has a thermal conductivity of $\lambda_f = 0.6$ W m^{-1} K^{-1}. The control of porosity on λ also implies that slight differences in λ_f due to salinity and temperature are also negligible.

Campbell and Norman (1998) modeled the bulk heat capacity c using a porosity-weighted arithmetic mean of the solid and fluid components

$$c = (1 - n)c_s + nc_f \tag{1.8}$$

where c_s and c_f are the volumetric heat capacities for the solid and fluid fractions. Combining Eq. 1.8 with Eq. 1.7 yields an equation for the bulk diffusivity κ

$$\kappa = \frac{\lambda_s^{(1-n)}\lambda_f^n}{(1 - n)c_s + nc_f} \tag{1.9}$$

showing the strong dependance of κ on porosity. Due to the relationship $\kappa = \lambda/c_V$, only two of the three thermal parameters are independent and the choice of which to measure lies mainly in how a particular experiment is designed.

Using harmonic analysis, Harrison (1985) found values of κ to be 0.4×10^{-6} m^2 s^{-1} in muddy sediments of Chinchester Harbor, England. Similar values have been measured in Minas Bay, Canada (Piccolo et al., 1993), Marennes-Oleron Bay, France (Guarini et al., 1997), and the Forth Estuary, Scotland (Harrison and Phizacklea, 1987), all in muddy sediments. At locations studied in this work, Willapa Bay and Skagit Bay, Thomson (2010) found values of κ between 0.4 and 1.4 m^2 s^{-1}. Sandy sites had large values for κ mainly due to the relationship of percent sand with porosity. As percent sand increased, porosity, and hence diffusivity increased as well.

1.2.2 Heat sources to tidal flats

The thermodynamic budget of tidal flats (Figure 1.1) are influenced by a variety of forcing terms including solar radiation, meteorological variables like cloud cover, wind, and humidity, and local water and sediment temperatures. The net heat balance can be represented by

$$Q_{net} = Q_s - (Q_l + Q_e + Q_h) + Q_{mw} \tag{1.10}$$

where Q_s is net shortwave radiation, Q_l is net long-wave radiation, Q_e is latent heat lost to evaporation, Q_h is sensible heat transfer, and Q_{mw} is the heat transfer between the sediment and water column. Q_{mw} is the most difficult term to observe or empirically derive and has received little attention both regarding its measurement and importance. Small tidal flat slopes create a large intertidal surface area between mean high and mean low water and the exposure of flats at low allows differential heating between the sediment bed and the water column. As the flats are inundated sediment and water temperatures may vary greatly, driving heat transfer across the interface and becoming an important contributor to water temperatures (Kim and Cho, 2009; Kim et al., 2010). Tidal velocities thus act as a mechanism to transfer heat across the flat and this cross-flat transport provides a linkage between the predominantly vertical air-water, air-sediment and sediment-water heat exchanges.

As the major external source of heat, solar shortwave radiation Q_{s0} represents the most important external forcing of tidal flat temperatures. In addition to daily extremes between solar noon and solar midnight, solar radiation varies seasonal in the mid-laditudes with maximum values in the summer of up to 1000 W m^{-2} and minimums in the winter as low as 100 W m^{-2} (Kim and Cho, 2009). The seasonal and daily patterns are further influenced by local and synoptic scale weather systems

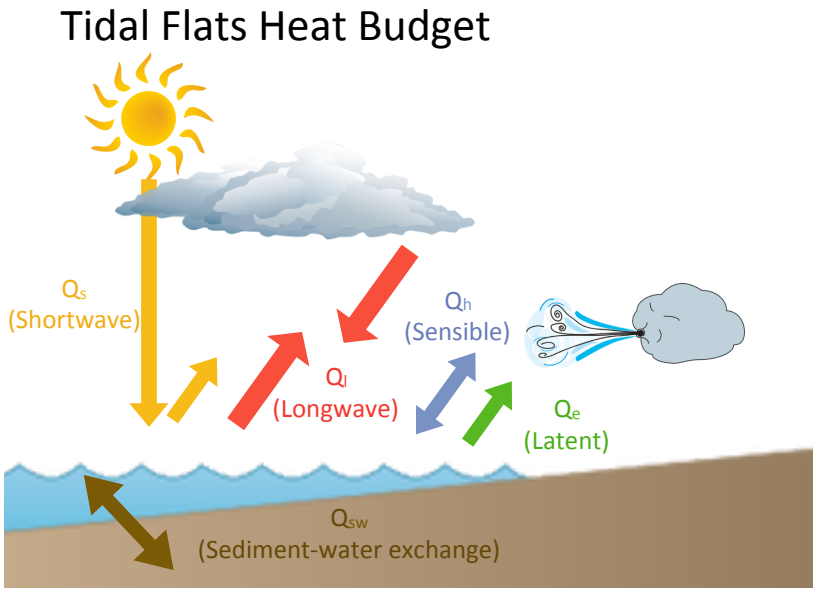

Figure 1.1 Schematic diagram of the various factors affecting tidal flat thermodynamics. The heat flux terms are net solar shortwave radiation Q_s, net longwave radiation Q_l, sensible heat flux Q_h, latent heat flux Q_e, and the sediment-water heat flux $Q_m w$. These terms are all affected by atmospheric conditions such as air temperature, cloudiness, and wind velocity. The primary heat flux terms are explained in Eq. 1.10.

driving the formation of clouds and also by atmospheric particulates that absorb and diffuse the shortwave radiation. Finally, the net solar shortwave absorbed depends on the albedo α which varies by both the material and solar angle. Typical daily mean albedos range from 0.05 for water and from 0.08 Guarini et al. (1997) to 0.3 Kim et al. (2007) for sediment.

The net longwave radiation Q_l is the difference between the infrared (IR) radiation emitted from the sediment or water surface and the downwelling IR radiation from the atmosphere and clouds. Longwave radiation emitted from a body is strongly dependent on temperature according to the Stefan-Boltzman Law describing black-

body radition

$$q_l = \sigma T^4 \tag{1.11}$$

where q_l is the black-body radiation emitted from an object with absolute temperature T and $\sigma = 5.67 \times 10^{-8}$ W m^{-2} K^{-4} is the Stefan-Boltzman constant. For real materials this is modified by an emittance ϵ equal to 0.98 for water and 0.96 for sediment (Thomson, 2010). The atmospheric component depends on water vapor content and cloudiness and is thus difficult to determine a priori, requiring the use of bulk formulations like those of Brunt (1932), May (1986) or Bignami et al. (1995). The exact formulation used for this study is described in Chapter 2.

Latent Q_e and sensible Q_h heat fluxes make up the remainder of the interaction with the atmosphere. Latent fluxes are due to phase changes of water such as condensation, freezing/melting of ice, and, most importantly for tidal flats, evaporation of water vapor, while sensible heat fluxes are due to conduction of heat between the tidal flats and the atmosphere. Both terms rely on atmospheric forcing such as air temperature, water vapor content, and wind speed, and require bulk formulations to estimate (Guarini et al., 1997). While latent fluxes are generally losses to the atmosphere due to evaporation, sensible heat fluxes can be directed towards either the atmosphere or the sediment/water of the flats based on the difference in temperature between the two media.

1.2.3 Thermodynamics of tidal flats

A limited number of studies have attempted to quantify the heat budgets of tidal flats. During sunny days exposed flats generally become warmer than embayment water while, conversely, during clear nights the sediment surface tends to cool much faster

than the water (Harrison, 1985). This can generate a large temperature differential between exposed flat and inundating water such that rapid changes in flat temperature occur during inundation and exposure (Harrison and Phizacklea, 1987). Spectral analysis of sediment temperatures show frequency peaks at 6 and 24 hr indicating that solar radiation and tidal forcing drive sediment temperatures (Piccolo et al., 1993).

Onken et al. (2007) indirectly measured the net heat flux from the tidal flats to the waters of the Hörnum Basin, German Wadden Sea. They observed water temperature and velocities at two locations within the main downstream drainage channel and inferred the net sediment-water heat fluxes by calculating a heat budget for regions upstream. During the spring and summer, the flats were a net sink of heat energy while during the fall they were a net source to the bay waters. They concluded that this pattern was based on the length of time that the flats were exposed and the correlation between exposure and solar radiation.

Field measurements alone are usually insufficient to understand the overall effects of tidal flats on heat transfer in the coastal zone. Advection of water during the tidal cycle transports heat across-flat while turbulence mixes heat throughout the water column. Guarini et al. (1997) implemented a heat-transfer model including all the terms of Eq. 1.10 within a simple 2-D model of Marennes-Oléron Bay, France. They found that mud surface temperatures varied on seasonal, fortnightly, and semidiurnal timescales and the temperature variations controlled the photosynthetic capacity of benthic algae. Mean sediment-water heat fluxes were from $\pm$10-40 W m^{-2} with positive fluxes into the water column not occurring until September.

To capture the cross-shore effects of sediment temperature on the water column

Kim et al. (2010) developed a 1.5-D model where water temperatures varied in the crosss-shore and sediment temperature varied both vertically and in the cross-shore. Their model was able to recreate observations from Baeksu tidal flats, Korea, where they found that between 300-800 Wm^{-2} were exchanged between the flat and the water during every tidal cycle. Using a fully three dimensional numerical model (FVCOM), Kim and Cho (2011) found the the flats, as a whole, represent a gain of heat energy in May and a loss in November with mean fluxes on the order of ± 10 W m^{-2}.

Kim et al. (2010) show that during spring local solar heating of exposed tidal flats in Baeksu, Korea caused temperature differences of 2 °C – 4 °C between the sediment surface and water column temperatures. Inversely, during the winter and times of limited incident solar radiation, exposed sediment temperatures were lower than water column temperatures with the coldest seawater temperatures occurring in the shallow regions of the embayment. These differences between sediment and water column temperatures create thermal gradients that drive heat exchange between the seabed and water column. Net heat transfer between the water and the sediment is thus determined by the phasing of solar shortwave radiation and periods of exposure of the tidal flats.

1.3 Overview

This dissertation examines heat transport over a variety of spatial and temporal scales using a combination of in situ and remotely sensed field observations and a simple cross-flat numerical model of heat transport. A brief overview of the field observations and numerical model is laid out in Chapter 2. These techniques are used in Chapter 3 (submitted as Rinehimer and Thomson (2013)) to analyze seasonal variations in sediment-water heat transfer at the Skagit Bay and Willapa Bay tidal

flats in Washington State. Chapters 4 and 5 then focus on tidal scale processes associated with the flood and ebb, respectively. Chapter 4 examines heating at the leading edge of the flood front during periods of high solar radiation and proposes a link between increased turbidity and absorption of heat by the water column. Chapter 5 (published as Rinehimer et al. (2013)) presents a novel method of determining velocities in shallow flows in order to quantify heat and mass transport off the tidal flats during the ebb period. Chapter 6 presents a summary of the dissertation and proposes questions arising as a result of this research such as climate change and restoration scenarios.

Chapter 2

METHODS

To answer the questions posed in Chapter 1, field observations and modeling studies were conducted on two tidal flats in Washington State, USA: Skagit Bay and Willapa Bay (Figure 2.1). This chapter provides an overview of the study sites, the sampling program and the numerical model of cross-flat heat transport.

2.1 Field Observations

2.1.1 Study Sites

Field observations and model calculations were performed for two meso-tidal flats in Washington State, USA: Skagit Bay and Willapa Bay (Figure 2.1). Willapa Bay, Washington (Figure 2.1) is a bar-built embayment located on the Pacific coast of the United States, north of the Columbia River mouth. The Long Beach Penninsula separates the estuary from the ocean with an 8 km wide inlet at the northern end of the bay. The tide is mixed semidiurnal with a mean daily range of 2.7 m, a neap tide range of 1.8, and a spring tide range of 3.7 m. The intertidal zone occupies nearly half of the bay's surface area (Anderson and Howell, 1984) and almost half of the bay's volume is flushed out of the bay on every tide (Banas et al., 2004). Extensive tidal flats composed of silt and clay sediments (Peterson et al., 1984) occupy much of the bay's intertidal region. The study sites are located in the southern portion of Willapa Bay, called Shoalwater bay, in sediments consisting of primarily silt and clay (Boldt

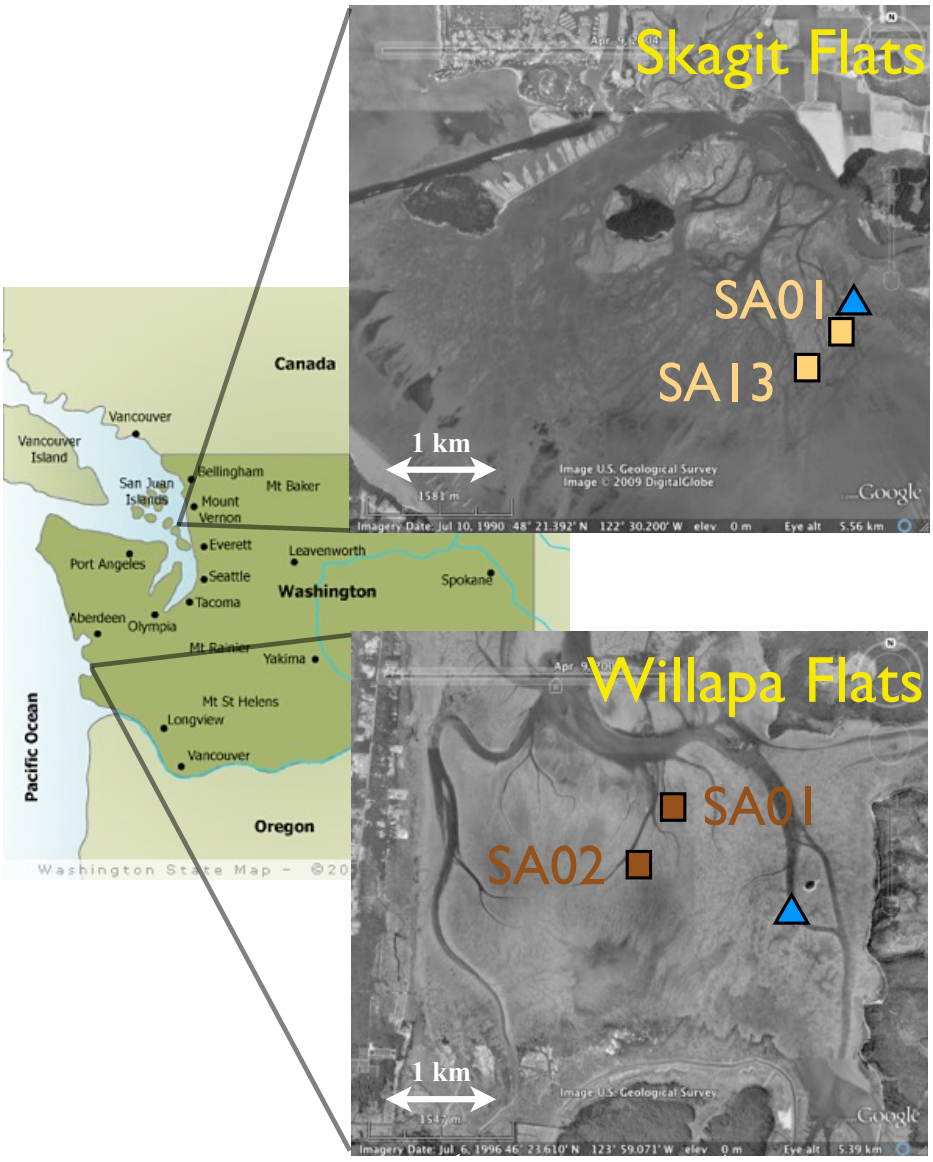

Figure 2.1 Location of field observations at Skagit Bay and Willapa Bay, WA, USA. Squares indicate the sand anchor locations at each site. Triangles are the locations of the HOBO Met station. Figure modified from Thomson (2010)

et al., 2013), while fine sand flats are found in higher energy areas, such as along the major channels and locations exposed to waves (Peterson et al., 1984).

Skagit Bay, located 230 km to the northeast of Willapa Bay, is a sub-embayment of Puget Sound and the receiving basin for the Skagit River, the largest river emptying into Puget Sound. Sediment deposits at the mouth of the Skagit River form a large intertidal delta with sand occurring nearshore and grain size fining southwestward, away from the mouth. Fine grained sediments are also located in sheltered areas north of the Swinomish Channel (McBride et al., 2006). Across-shore flat widths vary from 3 to 6 km with an along-shore distance of about 15 km.

2.1.2 Temperature observations

Sediment and water temperature observations were collected at both bays spanning a (non-continuos) period of two years (2008-2009). Hobo TempPro v2 temperature loggers affixed to a metal sand anchor (Figure 2.2) recorded temperatures in the sediment bed, spaced at 10 cm intervals spanning 10 - 50 cm depths in the sediment. At the sediment surface, a Hobo U20 water level logger measured water depth and surface temperatures. An additional TempPro logger attached to a length of string measured near-bed water temperatures during inundation at 10 cm above the sediment surface. The temperatures loggers recorded at 5 min intervals, over twice the response time of the loggers, and have an accuracy of $\pm$ 0.2 °C with a resolution of 0.02 °C. Prior studies (Thomson, 2010) have shown minimal effects due to heat conduction down the sand anchor and disturbance of the sediment bed during deployment with a RMS deviation of $<$0.15 °C between plastic and metal sand anchors. This variance is small compared to the $\pm$10 °C variations seen in the daily temperatures.

The temperature loggers were deployed at various sites throughout the flats during

the two-year study period. Long term observations at Skagit Bay occurred from November 2008 to September 2009. Short duration deployments at Willapa Bay included March and July 2009 with sampling locations throughout the flats and an intensive field experiment at D-Channel in March 2010 (See Chapter 5).

Figure 2.2 Sand anchors with affixed temperature loggers used in this study. A HOBO U20 water level logger is mounted at the top of the anchor and sits at the sediment surface with a co-located HOBO TempPro temperature logger. Four TempPro loggers are affixed at 10 cm intervals from 20 - 50 cm below the surface.

2.1.3 Acoustic and infrared measurement of velocities

Hydrodynamic measurements included a bed-mounted uplooking 2 MHz Nortek Aquadopp Acoustic Doppler Current Profiler (ADCP), deployed at D Channel, Willapa Bay to observe shallow ebb flows off of the flats (Chapter 5). The ADCP was deployed in HR (pulse-coherent) mode and measured velocity profiles at 1 Hz with a vertical resolution 10 cm. Due to the HR mode, the vertical profiling distance was limited to 1 m.

As the flows off of the flats during the ebb become quite shallow, an infrared

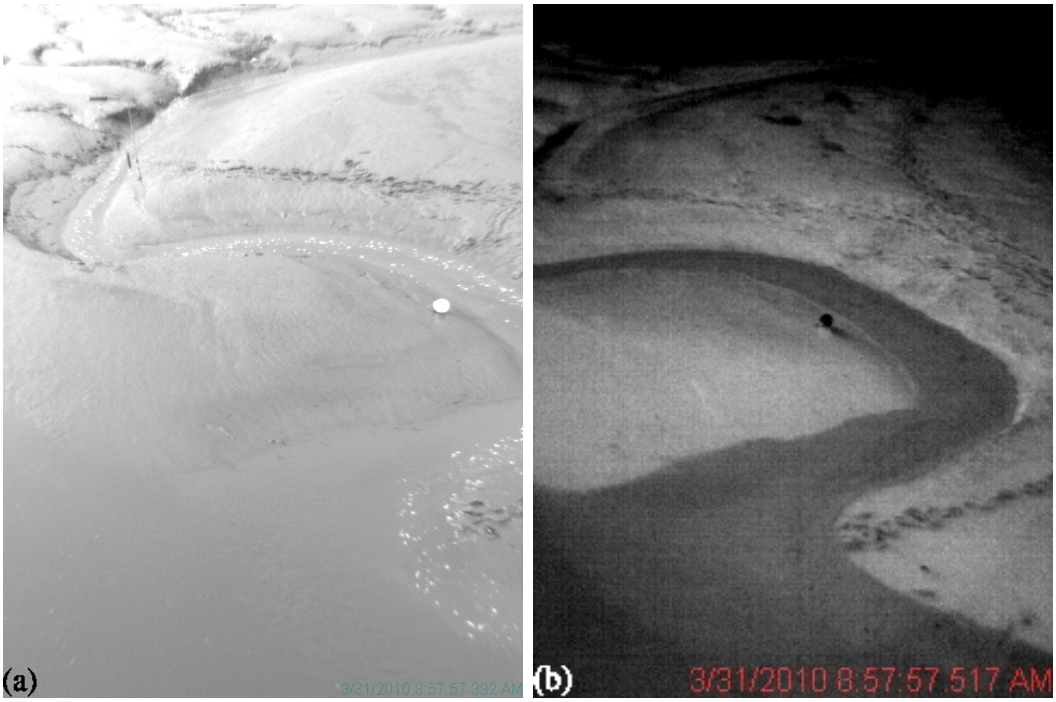

Figure 2.3 (a) Visual and (b) infrared imagery at Willapa Bay D Channel. Note how the contrast in the IR image is greater due to the large temperature differential between the exposed flats (lighter) and the water flowing out the channel (darker)

(IR) imaging system was used to estimate surface velocity within D-Channel. The IR camera was positioned on a 10 m tower attached to the D Channel piling. IR data were collected at 7.5 Hz with a 320 x 240 pixel, 16 bit, 8-12 μm thermal camera (FLIR A40) with a 39° horizontal field of view lens oriented along the channel axis. A 66° incidence angle provided an imaged area of approximately 100 m by 40 m and a horizontal resolution of O(1 cm) in the near-field degrading to O(2 m) in the far-field. An example of visual and infrared imagery can be seen in Figure 2.3.

The infrared images were georectified and an array of pixels aligned with the channel axis was extracted and converted into a "time-stack" image with along-channel distance varying across one image dimension and time across the other. A brief

summary of the technique follows with the full technique reported in Chapter 5. A two-dimensional Fourier transform technique was then performed in order to convert the image into frequency-wavenumber space. An additional transformation was applied to generated velocity-wavenumber images which are then integrated over the appropriate wave numbers to derive a velocity spectrum. This method provides accurate estimates of the surface water velocities and compares well with the limited observations from the acoustic instruments.

2.1.4 Additional observations

Meteorological, hydrodynamic, and remote-sensing observations were also used in various parts of this study. HOBO U30 meteorological stations located near the study sites collected 5 minute observations of air temperature, wind speed and direction, solar shortwave radiation, and relative humidity. The meteorological stations were attached to a 1.5 m tripod and located on the nearby Craft Island at 28 m elevation at Skagit Bay. At Willapa Bay it was affixed to a piling near Round Island at 7 m elevation. Nearby Washington State University AgWeatherNet stations (Long Beach at Willapa and Fir Island at Skagit) were used to provide meteorological data during brief data gaps. Hourly METAR reports from nearby airports (KAST, Astoria, OR for Willapa and KBVS, Burlington, WA for Skagit) were used to estimate cloud cover. As METAR observations report cloud cover values in oktas at various elevations, the maximum okta value over all reported elevations for each hourly report was used to determine the percent cloud cover.

2.2 Numerical model

A 1-dimensional (cross-flat) numerical model, following Kim et al. (2010), was developed to simulate the tidal wetting and drying of the flats and the heat fluxes to the water and sediment. The model considers horizontal, cross-flat advection of mass and heat as well as the vertical diffusion of heat in the sediment bed. The cross-flat resolution is 50 m and the water column is represented by a single, vertically homogenous cell at each cross-flat location. Pavel et al. (2012) indicate that some stratification occurs on the Skagit Bay flats, however, it is generally intermittent, occurring when the leading edge of the flood or ebb tidal front pass over the site. Mass and heat fluxes are assumed to be dominated by advective processes and cross-flat diffusion is not modeled. Along flat processes are considered homogenous.

2.2.1 Water column model

The model is forced at the open boundary by a tidally varying sea surface elevation η_t. Assuming a constant water elevation over the modeled domain allows calculation of the mass flux and velocity using only the continuity equation:

$$F_t^i = \sum_{k=i}^{M} \left(\frac{\eta_t - \eta_{t-\Delta t}}{\Delta t} \right) dx \tag{2.1}$$

where F_t^i is the volume flux between cells $i-1$ and i at time t, Δt is the time-step size, dx is horizontal cell size, and M is the total number of cross-channel cells in the domain. No fluxes are permitted through the onshore boundary. Subscripts indicate time indices while superscripts indicate space indices. Figure 2.4 graphically depicts the calculation of volume flux through each element. F_t^i is equivalent to the increase in the water elevation upstream of element i.

The water temperature $T^i_{w,t}$ at location i and time t is calculated by:

$$T^i_{w,t} = \Delta T_{local} + \Delta T_{adv} + \Delta T_{ext} \tag{2.2}$$

where ΔT_{local} is the local change in temperature due to the changing cell size (i.e. water elevation), ΔT_{adv} is due to the advective heat flux, and ΔT_{ext} is due to the external heat fluxes through the water surface or sediment-water interface. The local and external terms are calculated through first order, backward differences (in time) as

$$\Delta T_{local} = T^i_{w,t-\Delta t} \frac{H^i + \eta_{t-\Delta t}}{H^i + \eta_t} \tag{2.3}$$

$$\Delta T_{ext} = \frac{Q^i_{w,t} \Delta t}{C_w \left(H^i + \eta_t\right)} \tag{2.4}$$

where C_w is the volumetric heat capacity of water and $Q^i_{w,t}$ is the net heat flux into the water column (see below)

The advective term depends on the flow direction and is determined by

$$\Delta T_{adv} = \begin{cases} \left(T^{i-1}_{w,t-\Delta t} F^i_t - T^i_{w,t-\Delta t} F^{i+1}_t\right) \frac{\Delta t}{dx(H^i+\eta_t)} & \text{during flood} \\ \left(T^i_{w,t-\Delta t} F^i_t - T^{i+1}_{w,t-\Delta t} F^{i+1}_t\right) \frac{\Delta t}{dx(H^i+\eta_t)} & \text{during ebb} \end{cases} \tag{2.5}$$

At the open boundary, an offshore water temperature T_{sea} is specified while no fluxes occur through the landward boundary.

2.2.2 Sediment model

Vertical transport of heat within the sediment bed is modeled at each x-location according to the diffusion equation

$$\frac{dT}{dt} = \kappa \frac{dT s^2}{d^2 z} \tag{2.6}$$

where κ is the thermal diffusivity of the sediment and T_s is the sediment temperature, which varies with depth. The diffusion equation is solved at each modeled cross-flat location and no horizontal mixing is allowed between locations. Eq. 2.6 is modeled using a 2$^{\text{nd}}$-order Rung-Kutta method. The lower boundary condition assumes that dT/dz is constant with the layer above, while the boundary at surface interface is given by

$$\frac{dT}{dt} = \frac{Q_s}{\lambda_s} \tag{2.7}$$

where Q_s is the heat flux through the surface and λ_s is the thermal conductivity of the sediment. The bed is modeled from the surface down to 2 m depth.

Thermal diffusivity κ and conductivity λ_s depend on the the sediment type, porosity, and water content (Thomson, 2010). Kim et al. (2007) summarize prior studies with values of κ between 0.4-1.1 $\times 10^{-6}$ m^2 s^{-1} and λ between 0.8-3.1 W m^{-1} K^{-1}. For this study, $\kappa = 1.0 \times 10^{-6}$ m^2 s^{-1} was chosen for the Skagit Bay site and $\kappa = 0.5 \times 10^{-6}$ m^2 s^{-1} was chosen for Willapa Bay based on Thomson (2010) which found values of κ between 0.6-1.4 $\times 10^{-6}$ m^2 s^{-1} for Skagit Bay sand and 0.4-0.6 $\times 10^{-6}$ m^2 s^{-1} for Willapa Bay mud. A range of conductivity between $\lambda = 1 - 5$ W m^{-1} K^{-1} were used to tune the model and test sensitivity.

2.2.3 Heat fluxes

The net heat flux into the water column (Q_w) or the sediment (Q_s) is determined by

$$Q_w = Q_{ws} + Q_{wl} + Q_{wh} + Q_{we} + Q_{mw} \tag{2.8}$$

$$Q_s = Q_{ss} + Q_{sl} + Q_{sh} + Q_{se} - Q_{mw} \tag{2.9}$$

where Q_{xs} is the net shortwave radiation, Q_{xl} is the net long wave radiation, Q_{xh} is the sensible heat flux, Q_{xe} is the latent heat flux, and the first subscript x indicates

whether the flux is to the sediment (s) or the water column (w). Solar shortwave radiation is calculated according to

$$Q_s = (1 - \alpha_x)Q_{s0} \tag{2.10}$$

where Q_{s0} is the incoming shortwave radiation, Q_s is the net shortwave radiation, and α_x is the albedo of the appropriate substance. Despite seasonal variations in albedo due to changing solar angle Kim et al. (2007), constant mean values of $\alpha_s = 0.20$ and $\alpha_w = 0.05$ were used for the model (Thomson, 2010).

During exposure of the flats, all net radiation is absorbed by the sediment bed such that $Q_{ss} = Q_s$. During inundation, however, some of the incident solar shortwave radiation may still reach the seabed. The fraction of radiation that reaches the bed can be computed by the Beer-Lambert law:

$$T = e^{-K_d d} \tag{2.11}$$

where d is the depth, T is the transmissivity, and K_d is the extinction coefficient. The amount of shortwave radiation that is absorbed by the water column is $Q_{ws} = (1 - T)Q_s$ and the seabed $Q_{ss} = TQ_s$. The extinction coefficient varies as a function of wavelength, with longer wavelength radiation generally having higher extinction coefficients Jerlov (1976). Extinction coefficients of 1-10 m^{-1} are common for moderate turbidities from 10-100 mgL^{-1} within the 400 μm-700 μm photosynthetically active radiation (PAR) range. Nearly half of the solar shortwave radiation is outside this range, however, and within the more quickly attenuating IR range. Studies of the Hudson River plume indicate values of K_d >100 m^{-1} within the plume (Cahill et al., 2008). For this study, a bulk value will be used to estimate the qualitative impacts of absorption coefficient.

The long-wave heat flux, Q_{xl} is calculated following May (1986)

$$Q_{xl} = \left[\epsilon\sigma T_a^4 \left(0.4 - 0.05 e_a^{1/2}\right) + 4\epsilon\sigma T_a^3 \left(T_x - T_a\right)\right] \cdot \left(1 - 0.75 C^3.4\right) \tag{2.12}$$

where ϵ is the emisivity, σ is the Stefan-Boltzmann constant ($5.6705 \times 10^{-8} \mathrm{Wm}^{-2}\mathrm{K}^{-4}$), T_a is the air temperature, C is the fractional cloud cover from 0-1, and T_x is the water temperature T_w or the sediment surface temperature T_s.

Calculation of sensible heat transfer, $Q_w h$ is given by Guarini et al. (1997):

$$Q_{xh} = \rho_a C_{Pa} C_h \left(1 + U\right) \left(T_x - T_a\right) \tag{2.13}$$

where ρ_a is the density of air, C_{Pa} is the specific heat of air at standard pressure, C_h is the bulk transfer coefficient for conduction, and U is the wind speed in m/s.

Latent heat transfer, Q_{xe} is given following Guarini et al. (1997):

$$Q_{se} = \xi V_s \tag{2.14}$$

$$Q_{we} = V_w \tag{2.15}$$

where ξ is the water content of the flat surface with V_s and V_w defined as:

$$V_x = \rho_a L_V C_v \left(1 + U\right) \left(q_s - q_a\right) \tag{2.16}$$

$$L_V = \left[2500.84 - 2.35 \left(T_x - 273.15\right)\right] \times 10^3 \tag{2.17}$$

$$q_s = \frac{\lambda p_{sat}^V}{p_{atm} - (1 - \lambda) p_{sat}^V} \tag{2.18}$$

$$p_{sat}^V = \exp\left\{2.3 \left[\frac{7.5 \left(T_x - 273.15\right)}{237.3 + \left(T_x - 273.15\right)} + 0.76\right]\right\} \tag{2.19}$$

where ρ_a is the density of air (1.29 kg m^{-3}), C_v is the bulk transfer coefficient for conduction (0.0014), U is the wind speed (m s^{-1}) at 10 m, L_v is the latent heat of

evaporation, q_s is the specific humidity of saturated air at the (pore) water temperature, q_a is the absolute air humidity, p_{atm} is the atmospheric pressure and p_{sat}^V is the saturation vapor pressure

The heat flux through the sediment-water interface is denoted by $Q_{mw}$where positive values indicate heat flux to the water column and negative values indicate heat flux to the sediment. The sediment-water heat flux is estimated using a convective heat-transfer coefficient h_{sw} (Incropera and DeWitt, 2002)

$$Q_{mw} = h_{sw} \left(T_s - T_w \right) \tag{2.20}$$

Previous studies (Kim et al., 2010; Losordo and Piedrahita, 1991) have used a formulation of Q_{mw} which requires the determination of an effective sediment thickness, however, no guidance for the determination this parameter is presented. The use of a heat-transfer coefficient is common in convective transfer between a fluid and a solid (Incropera and DeWitt, 2002) and is straightforward to estimate empirically. Calibration and discussion of the importance of h_{sw} is presented in Chapter 3.

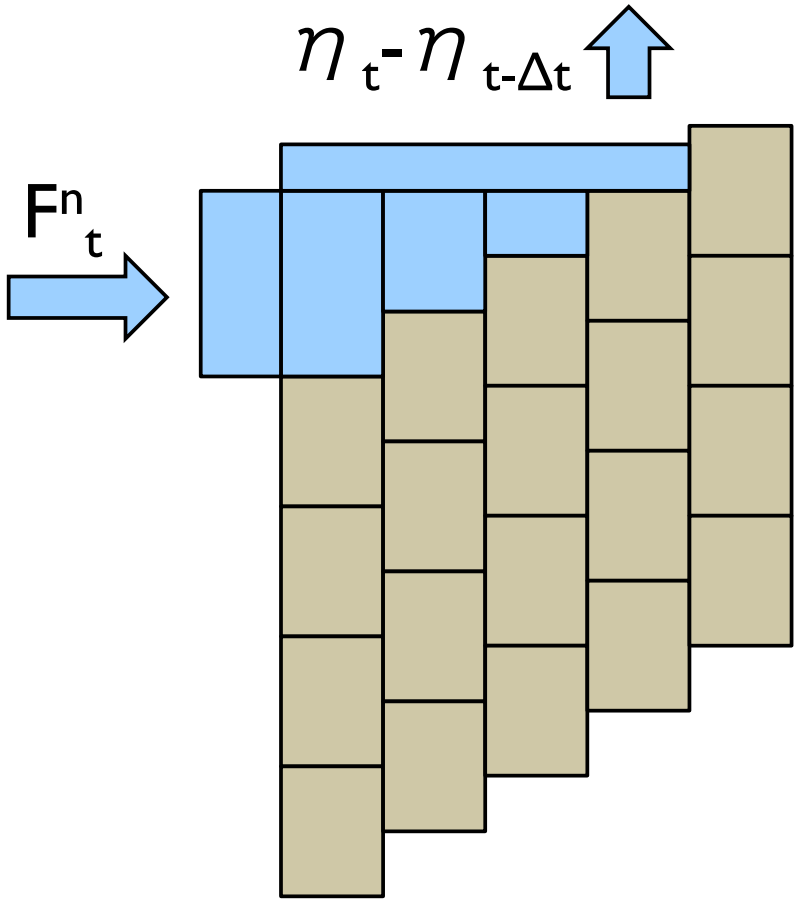

Figure 2.4 Graphical depiction of the model coordinates and continuity equation used to calculate volume fluxes at cell i (i.e. Eq. 2.1. The brown rectangles represent the elements of the sediment bed while the blue rectangles are the individual water column cells. The water column at each x-location is modeled by a single cell in the vertical while diffusion of heat is modeled vertical through the sediment bed. No cross-flat diffusion is allowed. The volume flux F_t^i through element i is balanced by the increase in water elevation upstream $\eta_t - \eta_{t-\Delta t}$.

Chapter 3

SEASONAL VARIABILITY OF SEDIMENT-WATER HEAT EXCHANGE ON TIDAL FLATS[1]

3.1 Introduction

Temperature is an important driver of both hydrodynamic and ecological processes, controlling rates of chemical reactions such as photosynthesis (Guarini et al., 1997) and, along with salinity, is an important control on water density. The temperature of the sediment and water column in tidal flat regions experiences rapid changes caused by alternating periods of exposure and inundation of the flats. Due to differences in thermal properties of water and sediments, exposed tidal flats temperatures can react much differently from water column temperatures. This temperature difference can drive heat exchange between the tidal flats and the water and is an important part of the heat budget in these areas.

Solar radiation represents the most important external forcing of tidal flat temperatures. Losordo and Piedrahita (1991) developed a numerical model to study the thermal structure of aquaculture ponds. During the spring, incident solar radiation heated the lake surface resulting in thermal stratification. There was sufficient mixing within the lake, however, such that heat exchange between the sediment and water column was important in determining the thermal budget. Warm water was mixed from above and the sediment bed acted as a net sink of heat. This was reversed

[1]Portions of this chapter and chapter 4 submitted as: Rinehimer, J.P. and Thomson, J. Seasonal and tidal variations of heat fluxes on tidal flats. Journal of Geophysical Research.

during the fall when diminished solar radiation and lower air temperatures resulted in the mixing of cold water to depth and the loss of heat from the sediment bed to the water column.

Similar seasonal cycles are apparent on tidal flats as well as in aquaculture ponds. Kim et al. (2010) found that, during spring, local solar heating of exposed tidal flats in Baeksu, Korea caused temperature differences of 2 °C – 4 °C between the sediment surface and water column temperatures. Inversely, during the winter and limited incident solar radiation, exposed sediment temperatures were lower than water column temperatures with the coldest seawater temperatures occurring in the shallow regions of the embayment. These differences between sediment and water column temperatures create thermal gradients that drive heat exchange between the seabed and water column. Net heat transfer between the water and the sediment is thus determined by the phasing of solar shortwave radiation and periods of exposure of the tidal flats.

The study of Kim et al. (2010) used a similar method to that of Losordo and Piedrahita (1991) to calculate the net heat flux between the sediment bed and the water column. They assume an effective sediment thickness (H_{sed}) over which heat exchange occurs to calculate the net sediment-water heat flux, following

$$Q_{mw} = C_s \frac{2\kappa}{H_{sed}} (T_w - T_s) \tag{3.1}$$

where Q_{mw} is the sediment-water heat exchange, T_w is the water temperature, T_s is the sediment surface temperature, H_{sed} is the 'effective' sediment thickness, and κ and C_s are the thermal diffusivity and volumetric specific heat capacity of the seabed. Values for H_{sed} are usually not given, however, nor are empirical methods of

their determination presented. While the effective thickness seems to be reasonable for sediments that are always inundated, it may be inappropriate for the dynamic depth changes occurring on tidal flats. These prior studies also required the specification of sediment temperatures at depth in order to accurately replicate their observations. Given that the major forcing for tidal flat areas is from surface heating and offshore advection, accurate predication of tidal flat temperatures should be possible without knowledge of the absolute temperatures at depth.

This chapter adapts the previous work and aims to improve thermodynamic process modeling for tidal flats. The results of in-situ measurements and modeling studies are described at two locations: Skagit Bay and Williapa Bay, Washington, USA during summer and winter 2009. The field data is used to calibrate and force a one-dimensional, cross-flat model of tidal flat mass and heat fluxes including heat exchange between the tidal flat sediment and water column. Times scales of seasonal, and fortnightly tidal variations are addressed. Estimates of net sediment-water heat fluxes for each season are determined and the sensitivity of the fluxes to sediment and water parameters is evaluated.

3.2 Methods

Field observations and model calculations were performed for two study sites in Skagit Bay and Willapa Bay (Figure 2.1). Sediment and water temperature observations, as outlined in Section 2.1, from January, March, and July of 2009 were used to determine the seasonality of the heat exchange between the water column and the sediment bed. The field observations were used both to calibrate the sediment-water heat transfer coefficient h_{sw} and to determine the effectiveness of the model in predicting the observations.

The 1-dimensional (cross-flat) numerical model, as described in Chapter 2 was used to simulate heat transfer processes across the flats. The cross-flat resolution is 50 m and the water column is represented by a single, vertically homogenous cell at each cross-flat location. Mass and heat fluxes are assumed to be dominated by advective processes and cross-flat diffusion is not modeled. Along flat processes are also ignored. Model bathymetry H^i is assigned according to the average slope of the flats, about 0.79 m/km at Skagit Bay and 0.76 m/km at Willapa Bay. The offshore boundary depth was -5 m for each site.

3.2.1 Calibration of h_{sw}

The heat flux through the sediment-water interface is denoted by $Q_{mw}$where positive values indicate heat flux to the water column and negative values indicate heat flux to the sediment. The sediment-water heat flux is estimated using a convective heat-transfer coefficient h_{sw} (Incropera and DeWitt, 2002)

$$Q_{mw} = h_{sw} \left(T_s - T_w \right) \tag{3.2}$$

Estimations of h_{sw} were obtained by the "heat storage" method (Harrison, 1985). To determine the change in heat content of the sediment bed, observations of sediment temperature with depth were integrated vertically according to:

$$Q_{mw} = \frac{\partial}{\partial t} \int_{z_0}^{0} C_v T(z) dz + \lambda_s \frac{\partial T}{\partial z}\bigg|_{z_0} \tag{3.3}$$

where C_v is the volumetric heat capacity of the sediment bed, λ_s is the thermal conductivity of the sediment, and z_0 is the depth of integration into the bed. The first term of the right hand side of Eq. 3.3 represents the change in storage of heat

in the upper portion of the sediment bed while the second term represents the flux of heat into the lower layers. $z_0 = 0.5$ m was taken as the lowest elevation of the sediment temperature measurements. Eq. 3.3 was discritized by a forward difference in time and a backward difference at $z = z_0$ to estimate heat transfer below z_0. h_{sw} was then estimated by fitting:

$$Q_{mw} = \frac{\Delta H_{sed}}{\Delta T} = h_{sw} \left(T_{sed} - T_w \right) \tag{3.4}$$

where H_{sed} was calculated using Eq. 3.3. Regressions were performed at each field location using the full time series of observations (Nov. 2008 – Sept. 2009) and by binning the data into 0.1 °C ΔT bins. Conditions were limited to periods of inundation were the depth was greater than 1 m in order to eliminate the potential interference of solar radiation reaching the bottom of the water column and providing an extra heat source to the sediment bed.

Examples of these regressions are shown in Figure 3.1 for characteristic sites at both Skagit Bay and Willapa Bay). Values of h_{sw} for both Skagit and Willapa Bays range from 2.0 to 20 $Wm^{-2}K^{-1}$, depending on the composition of a specific location. Correlations at both sites were quite good with $r^2 = 0.86$ for Skagit Bay and $r^2 = 0.85$ for Willapa Bay.

3.3 Results

Each location was modeled for 15-20 days during the winter and summer months in order to observe the spring-neap tidal cycle. Model time periods were based on observational time periods. The summer model time period for Skagit Bay was from 7-27 July 2009 and the winter period was from 9-29 January 2009. For Willapa Bay, the summer modeled time period was from 18-31 July 2009 and, due to the

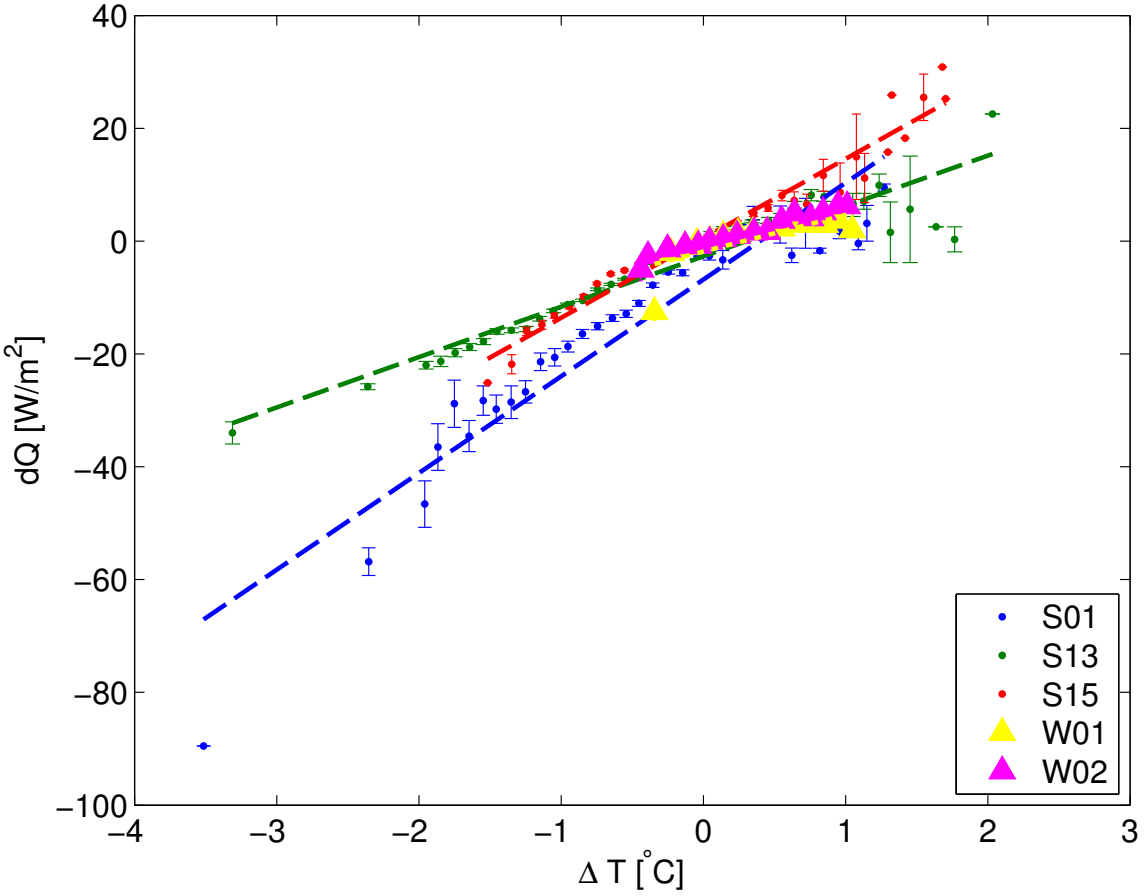

Figure 3.1 Example regression for h_{sw} for Skagit Bay (S01,S13,S15) and Willapa Bay (W01,W02). dQ is the heat difference as calculated by Eq. 3.3. Data have been binned into 0.1 °C intervals with the vertical error bars showing the standard error in dQ for each bin.

unavailability of winter data, the "winter" run was during 2-22 March 2009.

Figure 3.2 shows the observations and model results of water and sediment temperatures for Skagit Bay during summer 2009 (9-24 July). The strong summer solar shortwave radiation drives the sediment and water column temperatures during this time period. A fortnightly signal is evident, which is specific to the seasonal modulation of tidal phasing in the Pacific Northwest. During the spring tides (9-11 and 21-23 July), exposure of the seabed occurs during the day causing the surface of the flats to absorb the incident solar radiation and heat up. The heat then diffuses vertically down into the sediment. When the site becomes inundated, with cooler water above the surface of the flats, heating stops and the sediment cools as heat is conducted into the water column (i.e. Q_{mw} positive). During the neap tides (13-18 July), daytime exposures are brief and hence the sediments do not warm up. Instead the water column absorbs the solar shortwave radiation and Q_{mw} is then directed into the sediment. These sediment-water heat fluxes are generally 10-20% of the incoming solar-shortwave radiation.

The tidal phasing is reversed in the winter, and cooling results, as shown in Figure 3.3. In the winter spring tides, tidal flat exposure occurs during the night when no solar shortwave radiation is incident on the flats. This exposure leads to cooling of the sediments and the subsequent inundation of warmer water over cold flats. Sediment water heat fluxes are then directed towards the sediment bed during this entire time period. These sediment-water heat fluxes generally exceed the incoming solar-shortwave radiation.

For both seasons the model accurately represents the sediment temperatures. The root-mean-square errors (RMSE) in sediment temperature are 2.72 °C and 3.98 °C

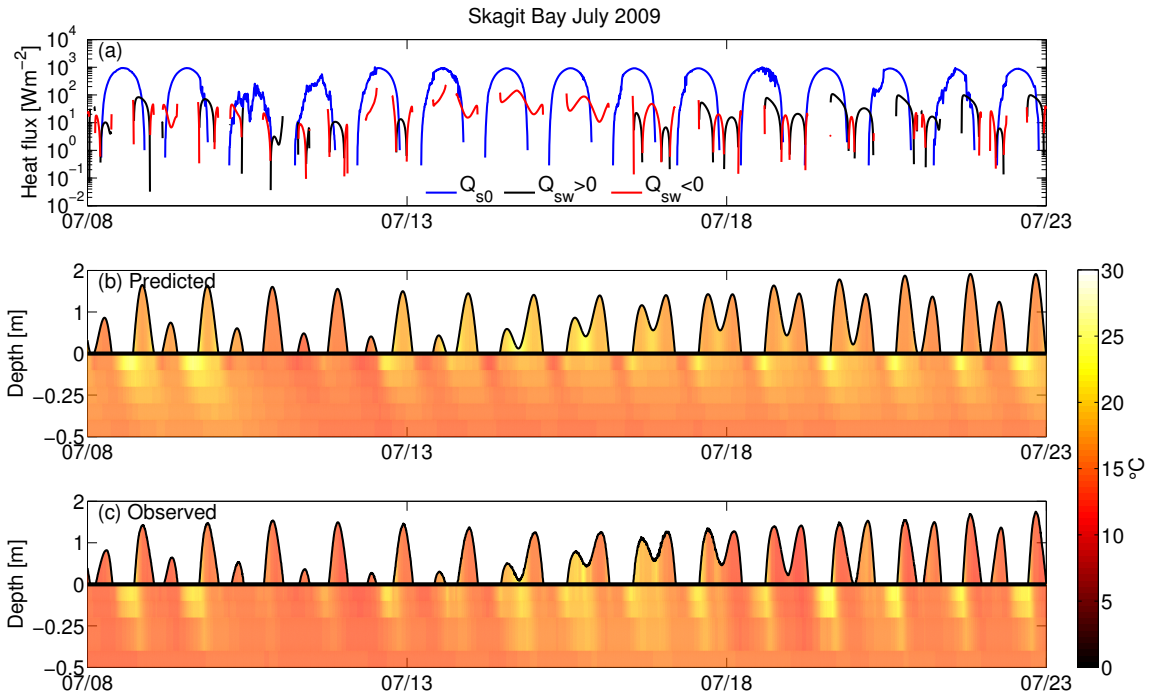

Figure 3.2 Modeled and observed results for 9-24 July 2009 at Skagit Bay S13. (a) Observed incoming shortwave radiation Q_{s0} (yellow), and modeled sediment-water heat fluxes Q_{mw} (red/black). Black lines indicate positive (into water) fluxes while red lines are negative (into sediment) fluxes. (b) Modeled and (c) observed sediment and water column temperatures. The sediment bed is represented by negative depths and is exaggerated 4x.

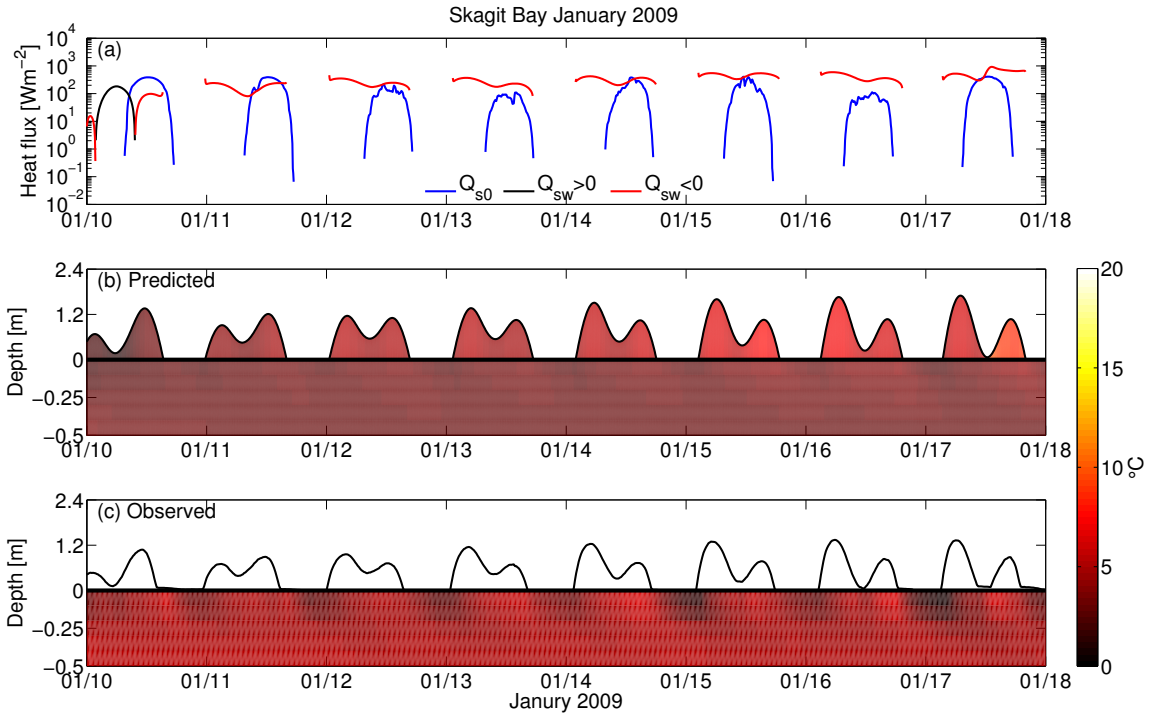

Figure 3.3 Modeled and observed results for 10-20 January 2009 at Skagit Bay S13. (a) Observed incoming shortwave radiation Q_{s0} (yellow), and modeled sediment-water heat fluxes Q_{mw} (red/black). Black lines indicate positive (into water) fluxes while red lines are negative (into sediment) fluxes. (b) Modeled and (c) observed sediment temperatures. The sediment bed is represented by negative depths and is exaggerated 4x. Water column observations were unavailable for this period.

for the summer and winter, respectively. The RMSE in water temperatures is 2.54 °C for the summer; no water temperature data was available for the winter. These errors are small relative to the 20 °C diurnal variations. The model is unable to reproduce some of the higher frequency variability (e.g., during the summer neap tides 13-18 July). This is likely due to circulation and along-flat variations, including changes in offshore temperature and river input.

Similar patterns are apparent at the Willapa Bay site for summer 2009 (July 21-28), as shown in Figure 3.4. Strong solar shortwave radiation heats up the exposed flats during summer low tides. The Willapa site has greater exposure during the smaller semidiurnal tide than the Skagit site due to the larger diurnal inequality in Puget Sound than on the coast. Minimal cooling occurs during these smaller tides, however, and the dominate summer time signal is the heating of the tidal flats. During the late winter (March 2-22), shown in Figure 3.5, night time cooling dominates the sediment temperatures causing sediment-water fluxes to be directed towards the sediment bed. Model RMSEs are 4.46 °C and 2.9 °C for the summer and winter water temperatures and 3.56 °C and 0.96 °C for the summer and winter sediment temperature, respectively. Despite the similar magnitude of Q_{s0} during July and March, Q_{mw} is directed into the sediment bed (from the water) for most of the winter results, because the exposure of the flats and high daytime shortwave radiation are out of phase.

3.3.1 Mean cross-flat temperatures and heat fluxes

Time-mean temperatures and heat fluxes were calculated along the cross-flat axis for each of the modeled periods. At Skagit Bay (Figure 3.6) summer mean sediment and water temperatures are in near equilibrium with temperature increasing upflat from 14

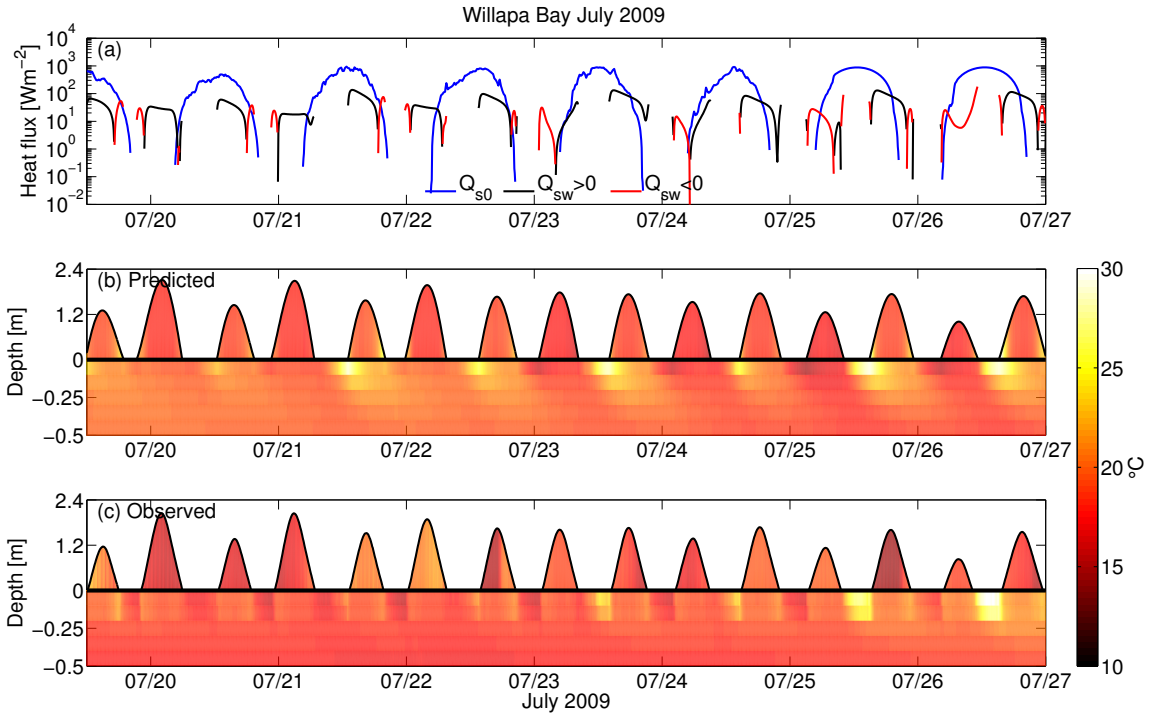

Figure 3.4 Modeled and observed results for 21-28 July 2009 at Willapa Bay W02. (a) Observed incoming shortwave radiation Q_{s0} (yellow), and modeled sediment-water heat fluxes Q_{mw} (red/black). Black lines indicate positive (into water) fluxes while red lines are negative (into sediment) fluxes. (b) Modeled and (c) observed sediment and water column temperatures. The sediment bed is represented by negative depths and is exaggerated 4x.

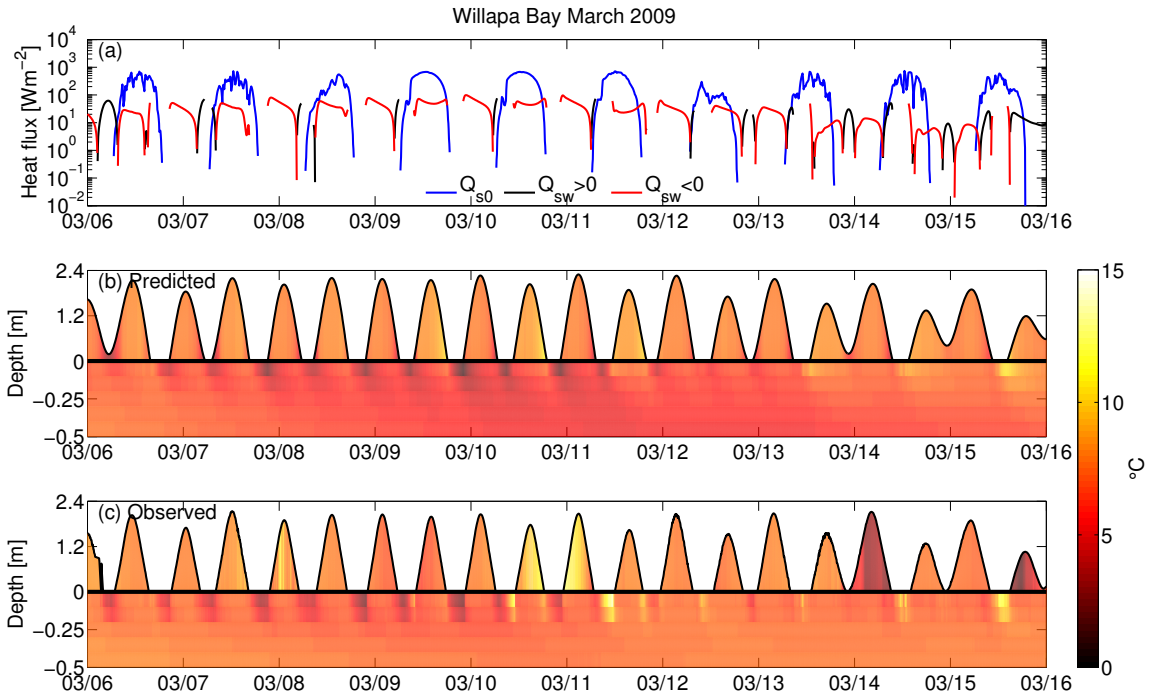

Figure 3.5 Modeled and observed results for 6-16 March 2009 at Willapa Bay W02. (a) Observed incoming shortwave radiation Q_{s0} (yellow), and modeled sediment-water heat fluxes Q_{mw} (red/black). Black lines indicate positive (into water) fluxes while red lines are negative (into sediment) fluxes. (b) Modeled and (c) observed sediment and water column temperatures. The sediment bed is represented by negative depths and is exaggerated 4x.

°C to 16 °C. Sediment temperatures from 1.5 - 4 km were greater than water column temperatures likely as a result of the increased period of exposure of the sediments as one moves upflat. Near the edge of the model domain at 4 km, sediment and water temperatures are once again near equal. As mean heat flux to the water is negative in this region, local heating cannot be responsible for the increased temperatures upflat and instead advective heat fluxes must be responsible.

Winter mean water temperatures at Skagit show a reverse trend to the summer temperatures with temperature decreasing from 10°C to 7°C from offshore to on shore. Sediment temperatures remain about 2.5°C below water temperatures throughout the flats resulting in Q_{mw} being negative across the whole tidal flat. This contrasts with the summer case where the mean sediment-water heat flux changes sign from negative at the offshore and onshore edges and positive in the midflat region. Also, the magnitude of Q_{mw} during the winter is larger at -30 W m^{-2} versus the summer at ± 5 W m^{-2}.

The spatial pattern of the total heat flux to the sediment bed Q_m varies between the summer and winter as well despite being positive during both seasons. During summer Q_m increases onshore while during winter the pattern is reversed and it decreases onshore. This is driven by the spatial pattern in the solar heat fluxes directly to the sediment. The solar and atmospheric fluxes increase upflat during the summer and decreased during the winter reflecting the fact that periods of exposure increase upflat.

Patterns at Willapa (Figure 3.7) are generally similar, with temperatures increasing upflat in the summer and decreasing in the winter. During the Willapa sumer period, however, sediment temperature is greater than water temperatures at all

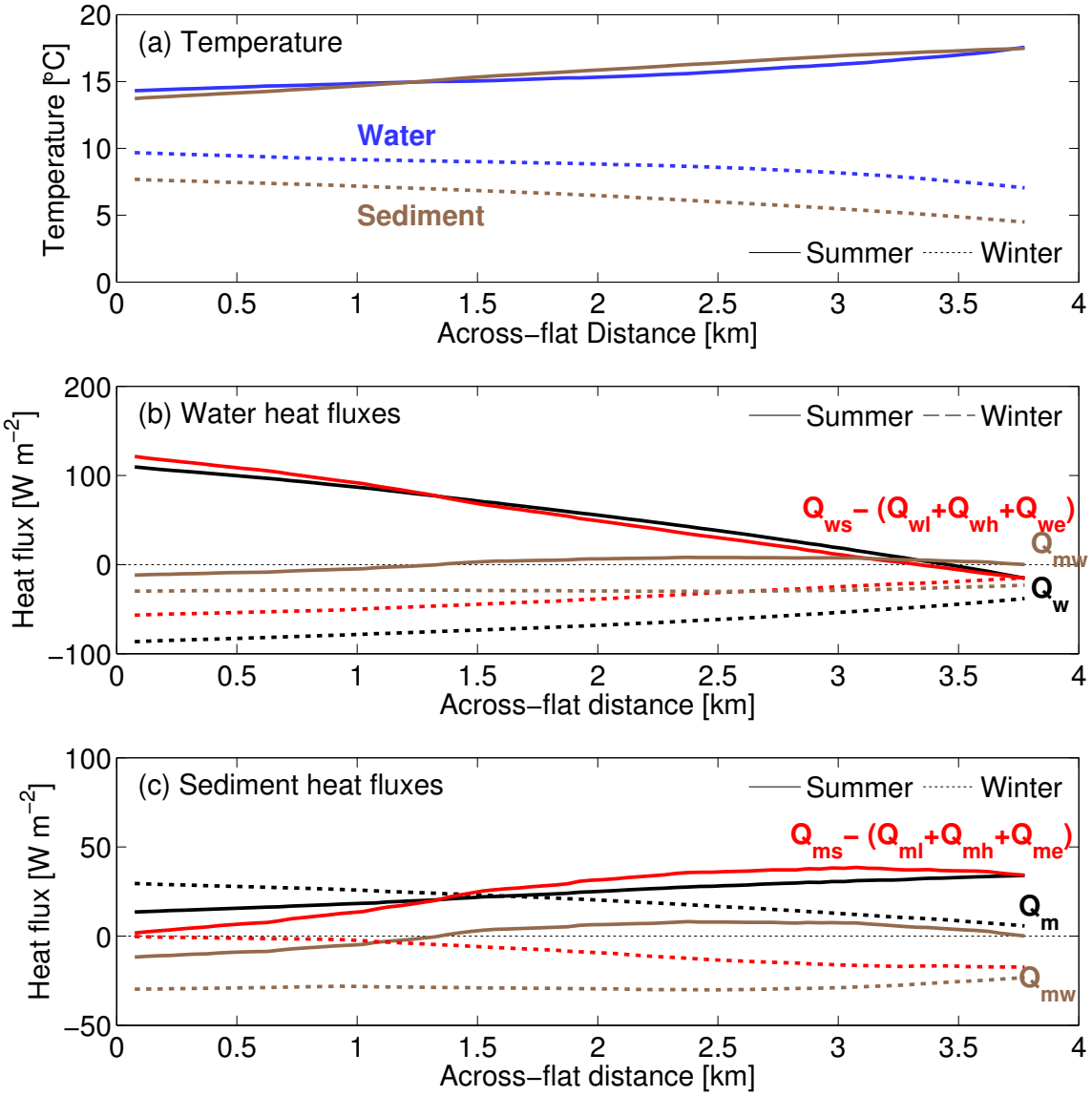

Figure 3.6 (a) Cross-flat profile of time-averaged (blue) water and (brown) sediment temperatures at Skagit Bay from (solid line) 7-27 July 2009 and (dashed line) 9-29 January 2009. (b) Cross-flat profile of time-averaged (black) total heat flux to the water, (red) sum of shortwave, longwave, latent and sensible heat fluxes, and (brown) sediment-water heat flux Q_{mw}. (c) Cross-flat profiles of time-averaged heat fluxes to the sediment. Colors the same as in (b).

cross-flat locations and thus Q_{mw} is directed towards the water everywhere. Also, the upflat region of heat loss in the water column occurs much closer to mid flat at 2.5 km as opposed near the upper limit of the flats. While the patterns of increasing and decreasing Q_m as you move upflat is similar to Skagit Bay, unlike at Skagit Bay, the sediment does not uniformly gain heat during both the summer and winter periods with upflat net losses during the winter and gains during the summer.

3.3.2 Cumulative Heat Fluxes by Season

To determine the long-term influence of sediment-water heat fluxes on the water column, Q_{mw} was integrated over each of the modeled periods for the the summer and winter cases. The cumulative heat fluxes for Skagit Bay are shown in Figure 3.8. During the summer, the sediment acts as a minor net source of heat to the water column, providing about 5 MJ m^{-2} of heat over a fortnight. During the winter, however, the sediment bed is a net sink, absorbing about 25 MJ m^{-2} of heat over a fortnight. The relationship between the phasing of the exposure of the flats and the incident shortwave radiation is clearly seen in panels (a) and (b) of Figure 3.8.

While the net Q_{mw} is slightly positive (from the sediment to the water) during the summer, the fluxes are modulated by the tidal signal: positive during spring tides and negative during neap tides. During spring tides maximum exposure and solar radiation are in phase, while during neap tides minimum exposure and solar radiation are in phase. Each tidal cycle, heat is transferred to or lost from the water at high tide depending on the conditions of the previous low tide. The opposite fortnightly signal is evident during the winter, and the net effect is a loss of heat from the water column to the sediment surface.

The effects of the coincidence of flat exposure and daytime solar radiation are

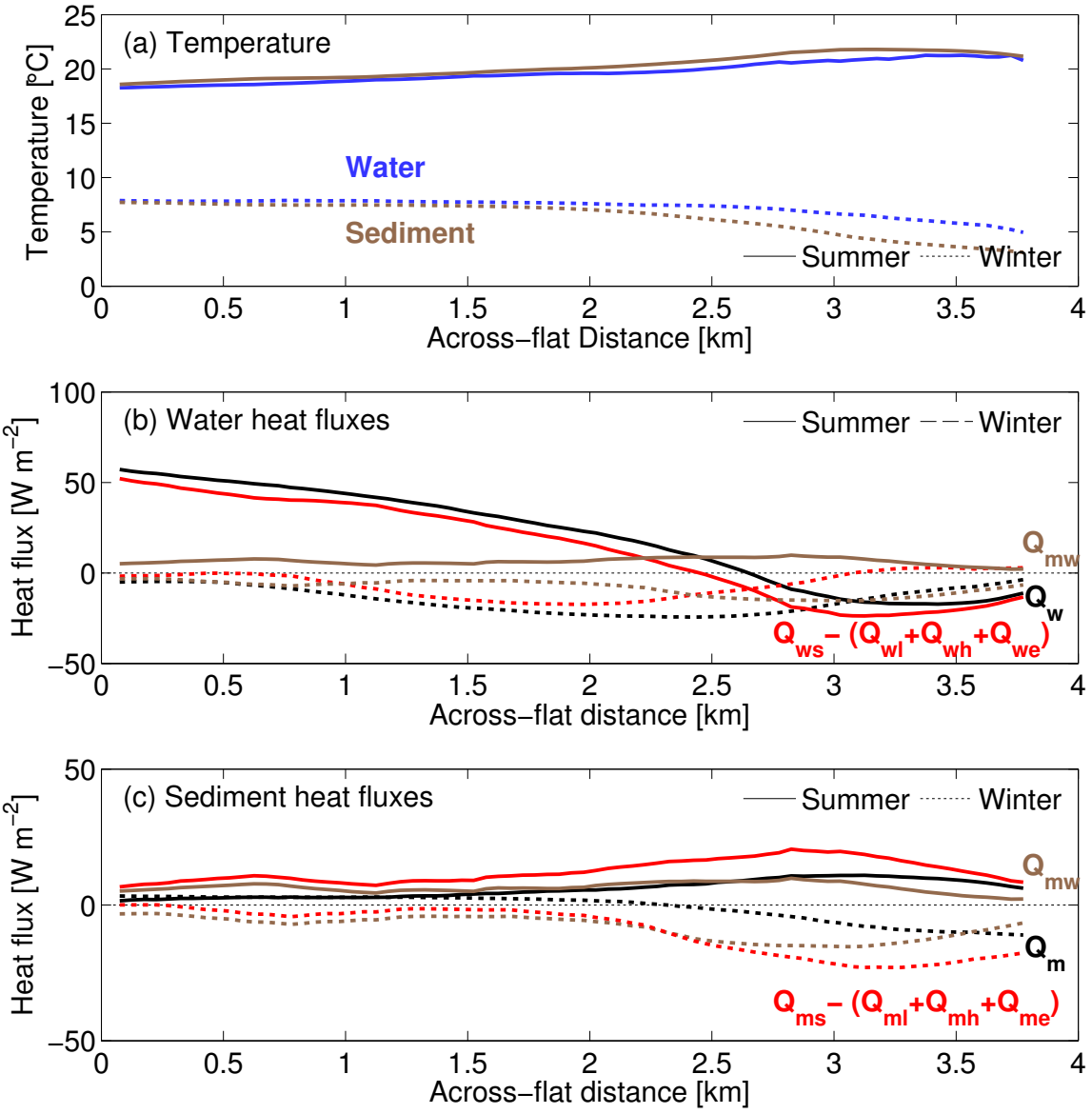

Figure 3.7 (a) Cross-flat profile of time-averaged (blue) water and (brown) sediment temperatures at Willapa Bay from (solid line) 18-31 July 2009 and (dotted line) 2-22 March 2009. (b) Cross-flat profile of time-averaged (black) total heat flux to the water, (red) sum of shortwave, longwave, latent and sensible heat fluxes, and (brown) sediment-water heat flux Q_{mw}. (c) Cross-flat profiles of time-averaged heat fluxes to the sediment. Colors the same as in (b).

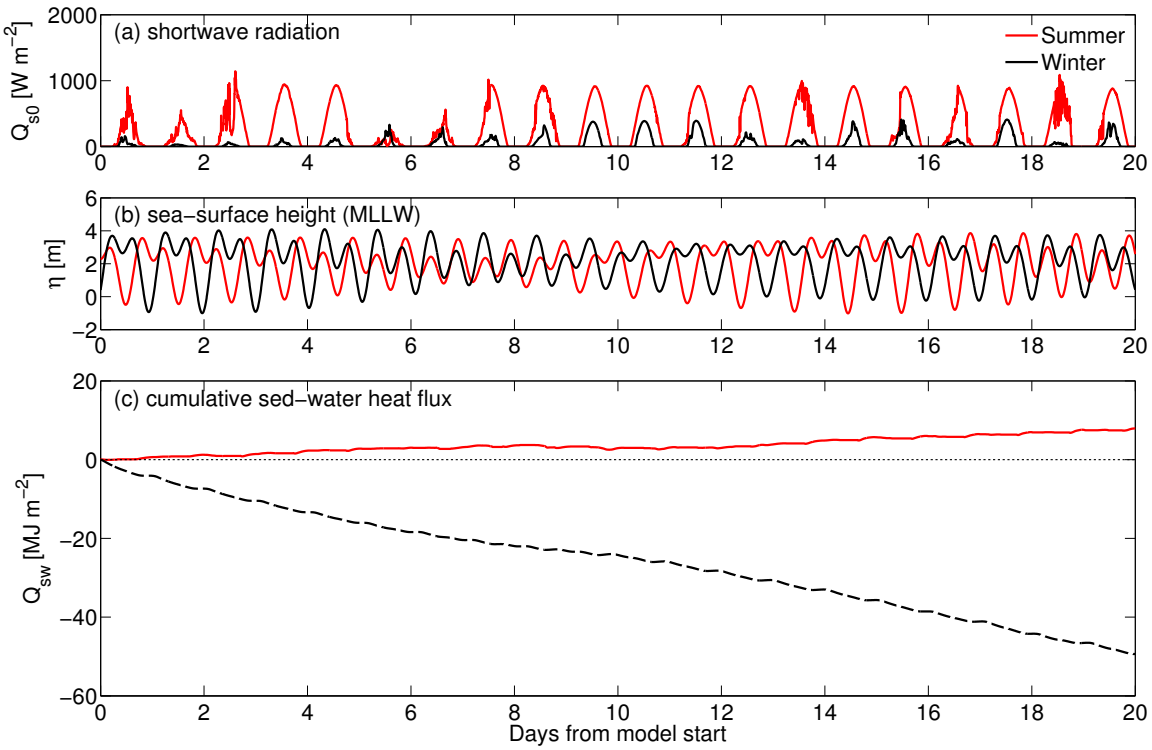

Figure 3.8 Modeled (a) Solar shortwave radiation, (b) sea-surface height, and (c) cumulative sediment-water heat fluxes for July (red lines) and January (black lines) 2009 at Skagit Bay S13.

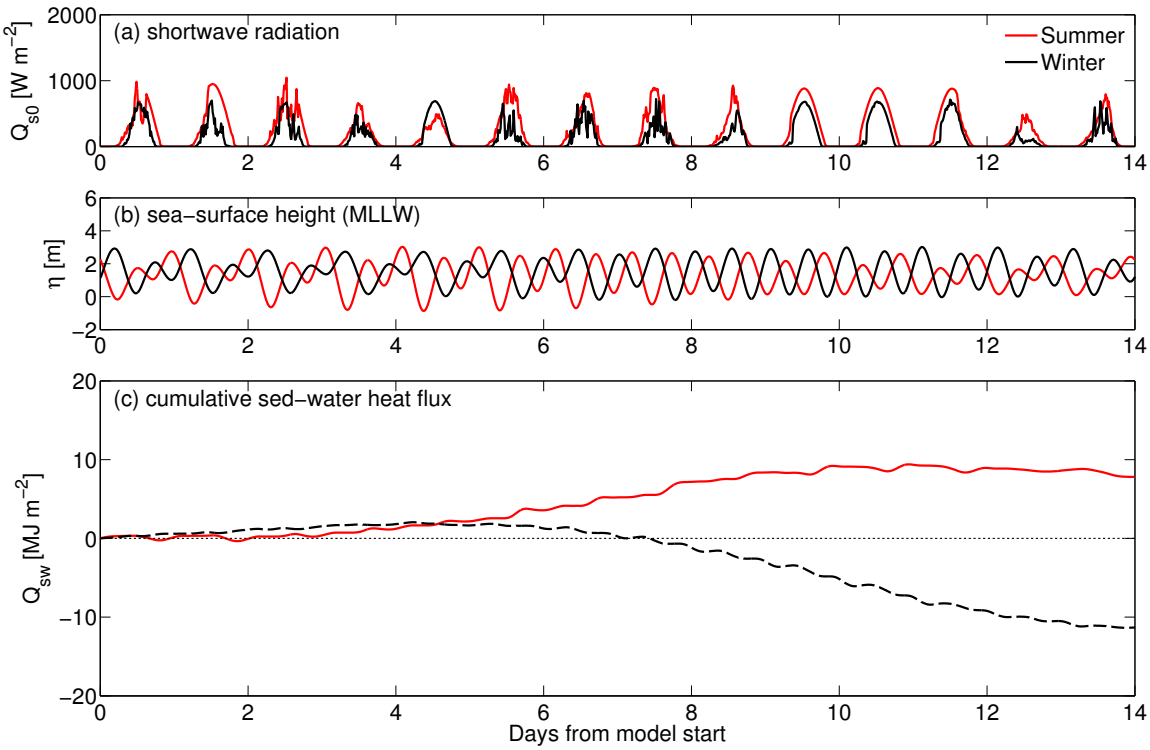

Figure 3.9 Modeled (a) Solar shortwave radiation, (b) sea-surface height, and (c) cumulative sediment-water heat fluxes for July (red lines) and March (black lines) 2009 at Willapa Bay S02.

even more apparent at Willapa Bay, as shown in Figure 3.9. Incidence shortwave radiation during March is 70% of the July values, because it is late in the winter, but the seasonal difference is still evident. The net cumulative heat flux during the July fortnight is only about +2 MJ m^{-2}, while net cumulative heat flux during the March fortnight is about -25 MJ m^{-2}.

3.3.3 Influence of solar-tidal phasing on sediment-water heat transfer

Phasing between flat exposure times and daily solar radiation was determined by calculating ΔT_{MLLW} as

$$\Delta T_{\mathrm{MLLW}} = T_{\mathrm{MLLW}} - T_{\text{solar noon}} \tag{3.5}$$

where T_{MLLW} is the time of Mean-Lower-Low Water (MLLW) and $T_{\text{solar noon}}$ is the time of local solar noon. Negative values of ΔT_{MLLW} indicate solar noon occurring before MLLW while if MLLW follows local solar noon, ΔT_{MLLW} is positive. The daily mean total sediment-water heat fluxes $\overline{q}_{mw}$ were determined by

$$\overline{q}_{mw} = \frac{1}{L_x} \int_0^{L_x} \int_{\text{daily}} Q_{mw}(t,x) dt dx \tag{3.6}$$

where the time integral is taken over each day. $\overline{q}_{mw}$ represents the mean of the total sediment-water heat transfer over all the cross-flat locations. Daily values of ΔT_{MLLW} and $\overline{q}_{mw}$ are shown in Figure 3.10 for each site and season. As the difference in time between MLLW and solar noon increases, sediment-water heat transfer falls and becomes directed from the water column to the sediment. The highest total sediment-water heat transfers occur when ΔT_{MLLW} is about 1to 2 hours following local solar noon. This lag is likely explained by local meteorological conditions. While the potential shortwave radiation is at a maximum at local solar noon, daily air

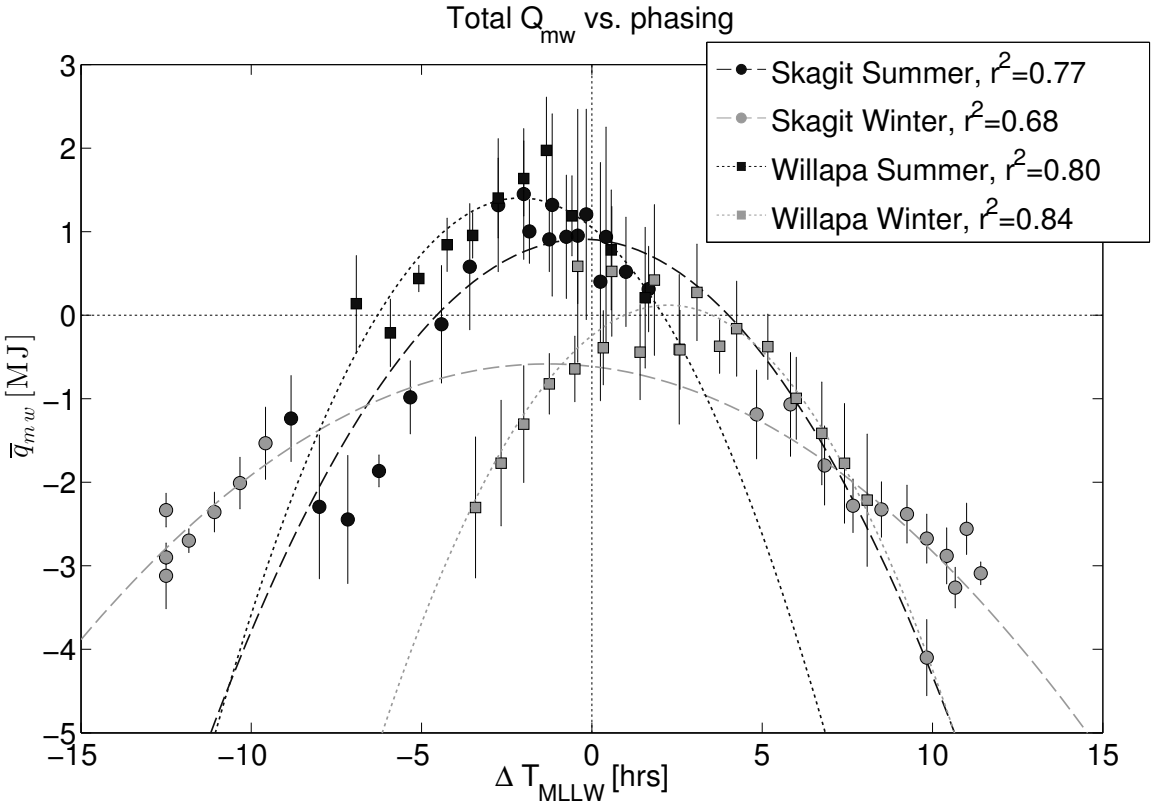

Figure 3.10 Modeled mean daily total sediment-water heat transfer $\overline{q}_{mw}$ vs. the time difference between MLLW and local solar noon ΔT_{MLLW}. Skagit Bay sites are circles and Willapa Bay sites are squares. Summer is in black and winter in gray. The errorbars are the standard deviation over all the modeled x-locations while the curves are least-squares fit lines using a 2^{nd} order polynomial.

temperatures, which control loss of heat from the sediment surface through longwave, latent, and sensible fluxes, do not peak until later in the day. Additionally the lag is more apparent during the summer months when a shallow marine layer generates morning cloudiness which generally gives way to clear skies by the afternoon. This diurnal cloudiness variation would strongly inhibit morning solar shortwave radiation and the subsequent increase in heat uptake by the exposed flats. In either case, MLLW occurrence during the morning would be less effective at storing heat than afternoon exposure.

The seasonality of the phasing is also apparent in Figure 3.10 as in the summer ΔT_{MLLW} is concentrated from -5 to 2 hrs while winter ΔT_{MLLW} ranges between $\pm$12 hrs. Interestingly, the range of $\overline{q}_{mw}$ seems independent of season with values between $\pm$3 MJ during both seasons at each site. Willapa Bay during the summer is an exception with a negative $\overline{q}_{mw}$ occurring only once, however this may just be due to the lack of data as ΔT_{MLLW} during WIllapa summer does not fall outside of -7 to 2 hrs where negative $\overline{q}_{mw}$ would be expected.

3.4 Discussion

The model results indicate that sediment and water column temperatures can be accurately predicted using a sediment-water heat flux coefficient and without the need of sediment temperatures at significant depths. The sensitivity of the results to λ_s, h_{sw}, and T_{sea} was tested by varying these parameters and calculating RMSE for the predicted sediment and water temperatures. Tables 3.1 and 3.2 lists the RMSE deviations for these temperatures at Skagit Bay and Willapa bay respectively. RMSE values vary slightly over the observed range of empirically determined (via regression) h_{sw}. As h_{sw} determines the rate at which the sediment and water exchange heat, it is

Table 3.1 RMSE error estimates for the Skagit Bay site. Bold numbers indicate values used for the "best" model runs.

	λ_s (W m^{-1} K^{-1})				h_{sw} (W m^{-2} K^{-1})				T_{sea}(°C)				
	1	5	8	10	5	10	15	20	6	8	10	12	14
Water July	2.85	2.64	**2.54**	8.04	2.77	2.63	**2.54**	2.48	-	4.06	3.09	6.69	**2.54**
Sediment July	6.06	3.57	**2.72**	2.87	2.73	2.73	**2.72**	2.71	-	1.83	2.06	2.28	**2.72**
Sediment January	5.53	4.21	**3.98**	3.88	4.69	4.37	4.14	**3.98**	5.04	4.68	4.32	**3.98**	-

Table 3.2 RMSE error estimates for the Willapa Bay site. Bold numbers indicate values used for the "best" model runs.

		λ_s (W m^{-1} K^{-1})				h_{sw} (W m^{-2} K^{-1})				T_{sea}(°C)					
		1.5	3	5	7	5	10	15	20	4	6	8	10	12.5	15
Water	July	4.49	4.47	4.46	**4.46**	**4.46**	4.41	4.37	4.35	-	-	-	8.05	6.12	**4.46**
	March	2.98	2.93	2.91	**2.90**	**2.90**	2.87	2.84	2.82	3.89	3.01	**2.90**	3.63	-	-
Sediment	July	5.11	4.14	3.73	**3.56**	**3.56**	3.60	3.65	3.71	-	-	-	3.76	3.64	**3.56**
	March	2.38	1.62	1.17	**0.96**	**0.96**	0.93	0.91	0.90	1.21	1.04	**0.96**	0.99	-	-

likely that this parameter is most important in determining temperatures immediately after inundation and becomes less important as the water and sediment temperatures equilibrate. There seems to be little significant difference between the choice of h_{sw} at either site.

It is also important to consider the role of advection of heat by tidal currents on the flats. As shown in Figures 3.6 and 3.7, the cross-flat pattern of total heat flux to the water column is inverse to the spatial pattern water temperatures. In the summer, temperatures increase upflat while fluxes decrease and vice-versa in the winter. In the absence of advection, temperatures at any given cross-flat location would depend only on local heat fluxes. Considering the initial conditions of the model are spatially

constant and the pattern of local heat fluxes and local temperatures are reversed, advection must be important in redistributing the local heat fluxes.

Advective processes also play a role in the importance of the offshore boundary condition. The role of the offshore temperature T_{sea} is evident by the greatest variability in RMSE under changes of T_{sea}. For the short time periods modeled in this study, constant T_{sea} values were sufficient, but long term measurements would be required to accurately model annual changes or climate scenarios. The offshore boundary condition also controls the rate of heat energy advection by currents over the flats.

3.5 Conclusion

A simple model of cross-shore tidal flat heat transport captures the basic patterns of temperature variations in both the water column and sediment bed for muddy and sandy sites during winter and summer months. Sediment-water heat fluxes are an important component of the heat budget, representing up to 20% of the incoming solar radiation and being larger than latent and sensible heat fluxes. The phasing of tidal flat exposure and daylight is important in controlling the sediment-water heat exchange. During the summer months, net heat flux is from the sediment bed to the water column as the longest periods of exposure occur during the daytime and result in the uptake of heat by the tidal flats. The heat stored in the flats is then released to the water column during inundation. Under winter conditions, the phasing is reversed with maximum flat exposure occurring during the night time, causing a loss of heat to the atmosphere and a net transfer of heat from the water column to the sediment.

Chapter 4

HEAT EXCHANGE AT THE THIN FLOODING FRONT

4.1 Introduction

Tidal currents are the most important energy source on tidal flats driving turbulent mixing (Ralston and Stacey, 2005), shaping flat morphology (Friedrichs, 2012), and transporting salt, heat and sediments. As explored in Chapter 3, advection of heat energy due to tidal currents is an important process in the spatial variation of the heat budget of tidal flats. As the tide rises a thin flooding front advects over the tidal flats wetting previously exposed sediments and providing a mechanism to transmit heat between the flat surface and the flowing water. This chapter and the next (Chapter 5) will evaluate the thermodynamic processes that occur during the flood and ebb tides to determine the importance of advection in determining water temperatures on tidal flats.

Onken et al. (2007) studied the advective heat flux off of tidal flats to the waters of the Hörnum Basin, German Wadden Sea. They observed water temperature and velocities at two locations within the main downstream drainage channel and inferred the net sediment-water heat fluxes by calculating a heat budget for regions upstream. During the spring and summer, the flats were a net sink of heat energy while during the fall they were a net source to the bay waters. Tidal currents provided the medium to transport the heat energy from the flats back into the embayment.

Using the three dimensional numerical model FVCOM, Kim and Cho (2011) stud-

ied the heat budget of a tidal flat in coastal Korea. The authors calculated the net transport of heat from the intertidal zone to offshore waters over a one year period. While seasonal mean sediment-water heat fluxes were small ($\pm$ 5 W m^{-2}) compared to the air-water heat fluxes ($\pm$ 100 W m^{-2}), net mean heat fluxes were small ($\pm$ 5 W m^{-2}) due to the near balance between the air-water heat fluxes and advective fluxes ($\pm$ 100 W m^{-2}) implying that an accurate understanding of all parts of the heat budget are necessary to determine net effects. Heat transfer occurring during the flooding and ebbing tides is the link between offshore water and sediment-water heat exchange on the flats.

Airborne IR (Figure 4.1) observations at Skagit Bay taken during our study period show pronounced heating at the leading edge of the flooding front. Instantaneous photographs from individual flight paths were complied over roughly 1 hour to generate a near-synoptic image of the flood tide. During these observations, tidal elevations in Skagit Bay are rising and cooler Skagit Bay water is inundating the tidal flats. Onshore, exposed tidal flats appear light and therefore warmer due to solar heating during exposure. Incised channels on the flats can also be seen where cold water from the Skagit River is emptying into Skagit Bay.

At the leading edge of the flood front, there is a bright (warm) region that consists of water with temperatures elevated far above the tidal flat sediment temperatures. Because the water temperatures are significantly higher than the sediment temperatures in this region, sediment-water heat exchange would be occurring in the opposite direction to that necessary to heat the edge of the flooding front. Therefore some combination of local and advective process is required to create and maintain this signal over the flood tide.

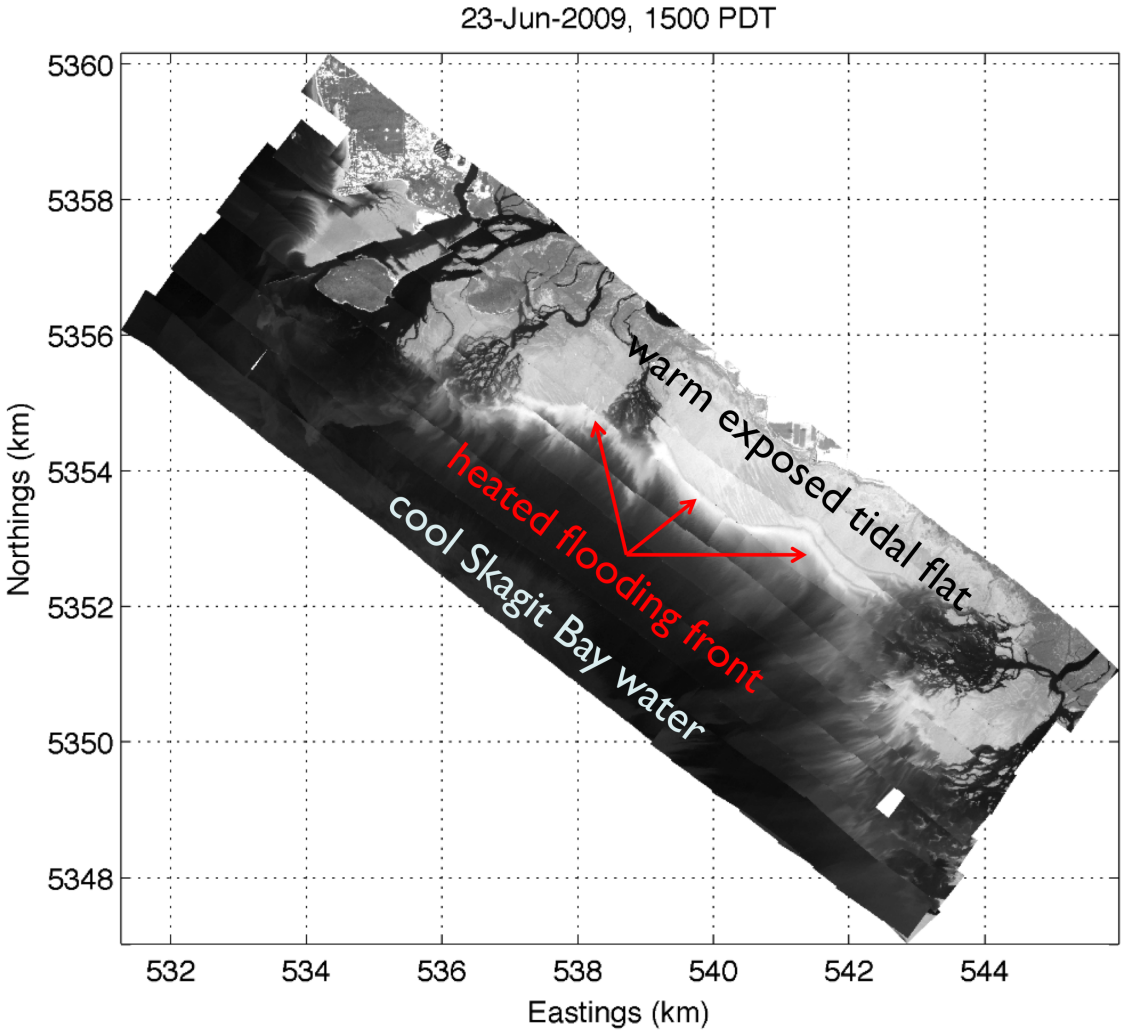

Figure 4.1 Mosaic of aerial IR imagery. Brighter regions are areas of higher thermal emission and generally correlate to higher temperatures. The exposed flats are bright and to the top and right of the figure while Skagit bay water is dark and to the left and bottom of the figure. The edge of the heated front is notated.

As local heating is driven by the sun, a potential source for heating of the front leading edge is due to increased absorption of solar shortwave radiation in the water column. As the front is only centimeters deep, much of the solar radiation would pass through the thin layer of water and encounter the sediment bed. Therefore, in order to heat the water column more than the sediment would require high extinction coefficients K_d such that most of the solar radiation is absorbed in the water column.

In this chapter the source of heating during the flood tide is investigated. The role of the extinction coefficient (i.e., higher solar absorption by the water column) is tested by alternate model runs varying the value of K_d. Observations of periods immediately following inundation are presented and modeled to determine the heat fluxes involved. A Lagrangian approach is then considered to estimate the fluxes into a water parcel on the edge of the front.

4.2 Methods

As covered in Chapter 2, during tidal flat inundation the fraction of solar shortwave radiation that reaches the seabed is computed from the Beer-Lambert law:

$$T = e^{-K_d d} \tag{4.1}$$

where d is the depth, T is the transmissivity, and K_d is the extinction coefficient. The amount of shortwave radiation that is absorbed by the water column is $Q_{ws} = (1 - T)Q_s$ and the seabed $Q_{ss} = TQ_s$. For this study, two bulk values of $K_d = 1$ m^{-1} and $K_d = 1000$ m^{-1}were tested. While extinction coefficients vary as a function of wavelength, with longer wavelength radiation generally having higher extinction coefficients (Jerlov, 1976), a bulk value provides an average over all wavelengths and is more compatible with the available observational data. Most studies of light extinc-

tion are focused on its effects on photosynthetic activity and only measure radiation in the photosynthetically active (PAR) range of 400 μm-700 μm. Values for K_d of 1-10 m^{-1} are common for moderate turbidities from 10-100 mgL^{-1}. Nearly half of solar shortwave radiation is outside this range and within the more quickly attenuating IR range. Studies of the Hudson River plume indicate values of K_d >100 m^{-1} within the plume for the full range of solar shortwave radiation (Cahill et al., 2008). Our choice of extinction coefficients was meant to provide end-member results of near-total absorption and transmittance by the water column and provide a qualitative examination of the processes involved.

Field observations (discussed in Chapters 2 and 3) from both the summer and winter at Willapa and Skagit Bays were used in this chapter. The model setup was the same but model calculations were performed for two different cases of K_d values in order to test the differences in absorption of solar energy between these conditions.

4.3 Results

4.3.1 Observations and modeling of the leading edge of the flood front

Figure 4.2 shows the spatial distribution of modeled sediment and water column temperatures in Skagit Bay during the summer period. The highest water column temperatures are seen at the leading edge of the flooding front and at the trailing edge of the ebb tide. These are the periods that the water column is the shallowest, indicating that local heating processes are likely responsible. As the heat fluxes along the cross section at any one moment in time are generally similar due to synoptic-scale forcing, temperature differences would be driven by the differences in volume at each location. Patterns of sediment temperatures are generally based periods of

inundation and exposure. When nightly exposures occur, the flats cool, while they heat up when exposed during the daytime.

Winter patterns (Figure 4.3), on the other hand, show cooling at the leading edge of the flat. Changes in sediment temperature during exposure are also not as extreme. This is likely due to the sediment temperature reaching a relative equilibrium with the water column. Winter sediment temperatures range from 2-6°C with water temperatures in a similar range.

Cross-shore patterns at Willapa Bay (Figures 4.4 & 4.5) are similar to Skagit Bay. The leading edge of the flood and ebb fronts exhibit the largest temperature gradients in the water column. Behind the leading edges, water temperatures become nearly uniform approaching the offshore temperatures T_{sea}. During the summer, the leading edge exhibits local heating while during the winter the leading edge is cooled down compared to the bulk of the flooding water behind it.

During the summer period at Skagit Bay, water column temperatures immediately after inundation are ~ 5°C warmer than the sediment bed surface temperatures. This can be seen more clearly by phase-averaging the results at each of the sand anchor locations by the time after inundation. Figure 4.6 presents the phase-averaged observations and model results for both extinction coefficient during the summer at each site. The modeled large extinction coefficients more closely match the observational results in both cases.

At Skagit Bay, the phase-averaged temperatures show the initially high water temperatures immediately after inundation followed by the cooling later in time. By 1 hour after inundation water temperatures become lower than the sediment temperatures. The sign of the difference between the water and sediment temperatures

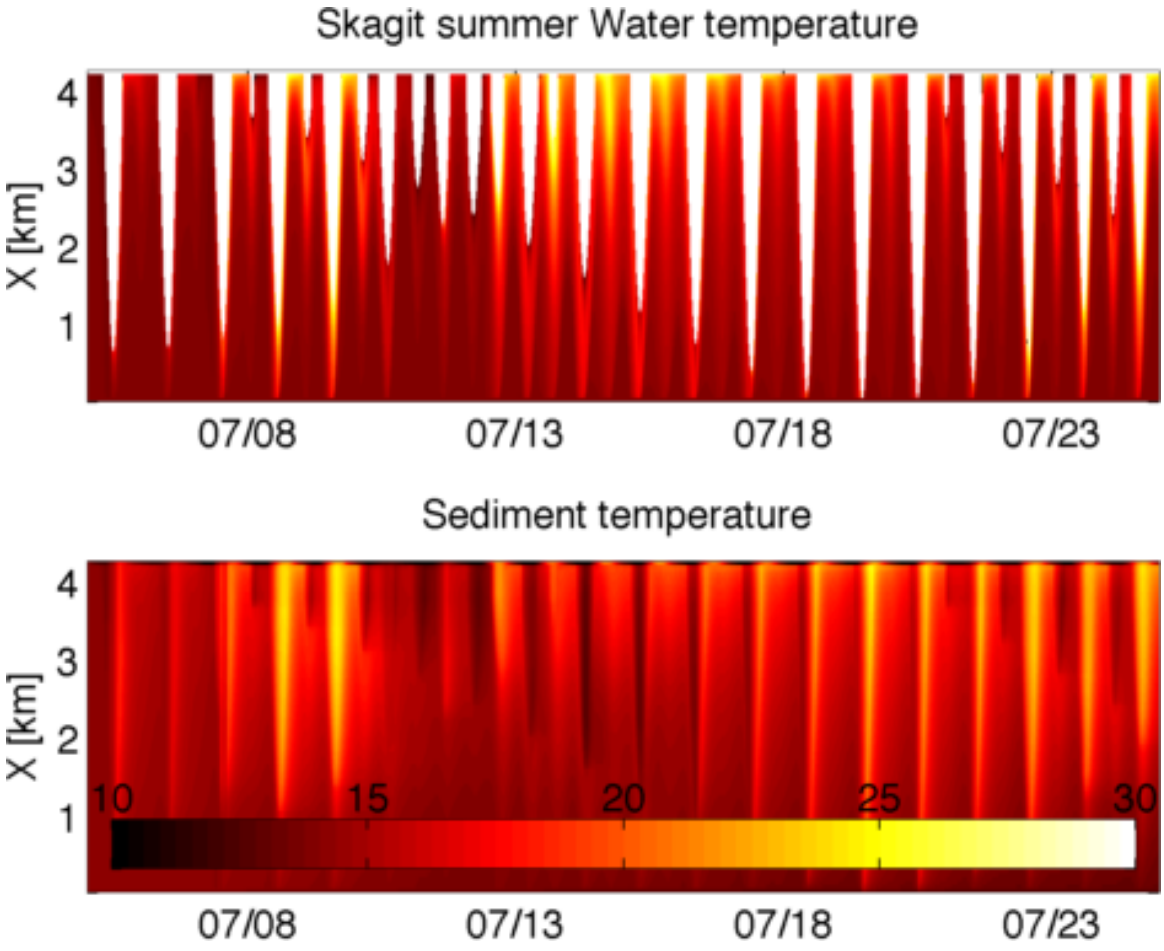

Figure 4.2 Model Skagit Summer (a) water and (b) sediment temperatures varying in time and cross-shore distance with $K_d = 1000$ m^{-1}. White areas in the water temperatures indicate the cell is dry.

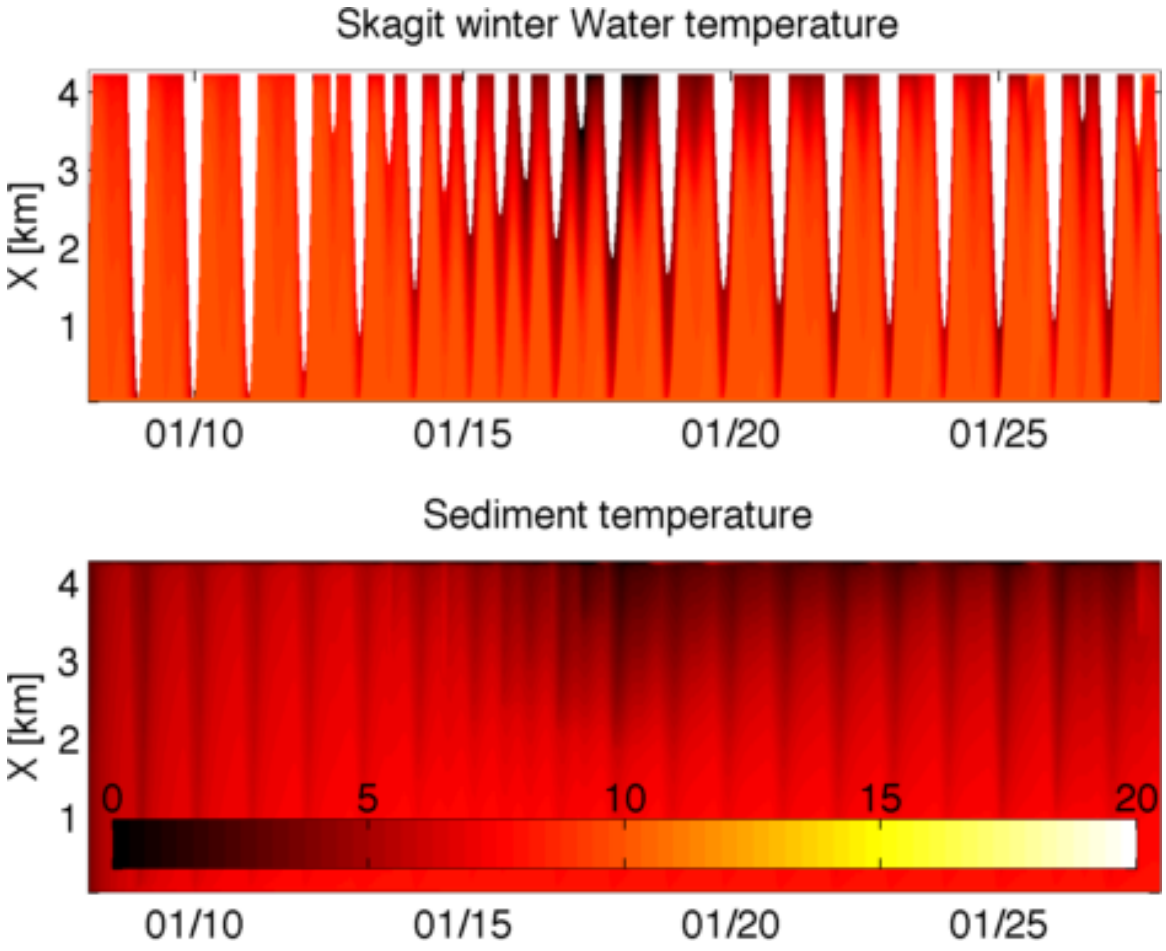

Figure 4.3 Model Skagit Winter (a) water and (b) sediment temperatures varying in time and cross-shore distance with $K_d = 1000$ m^{-1}. White areas in the water temperatures indicate the cell is dry.

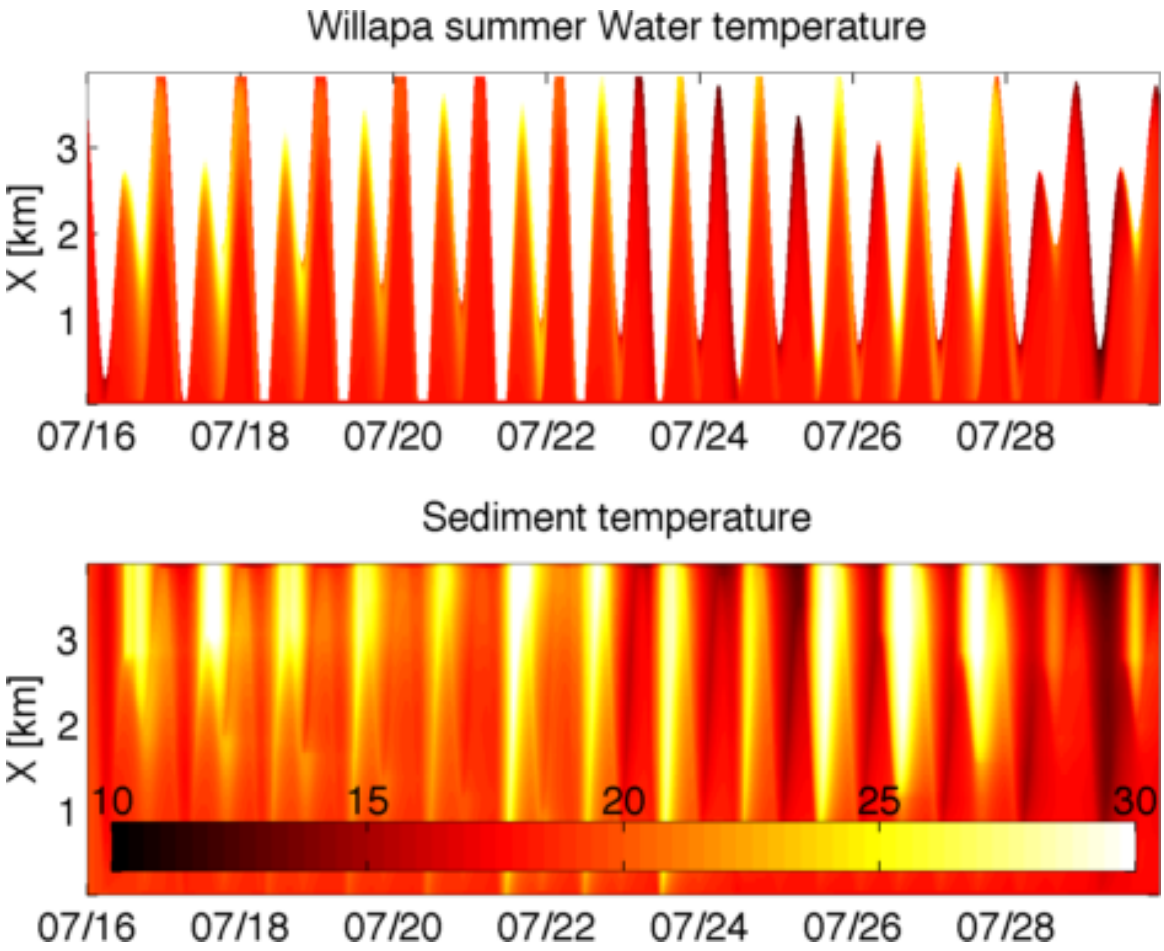

Figure 4.4 .

Model Willapa summer (a) water and (b) sediment temperatures varying in time and cross-shore distance with $K_d = 1000$ m^{-1}. White areas in the water temperatures indicate the cell is dry.

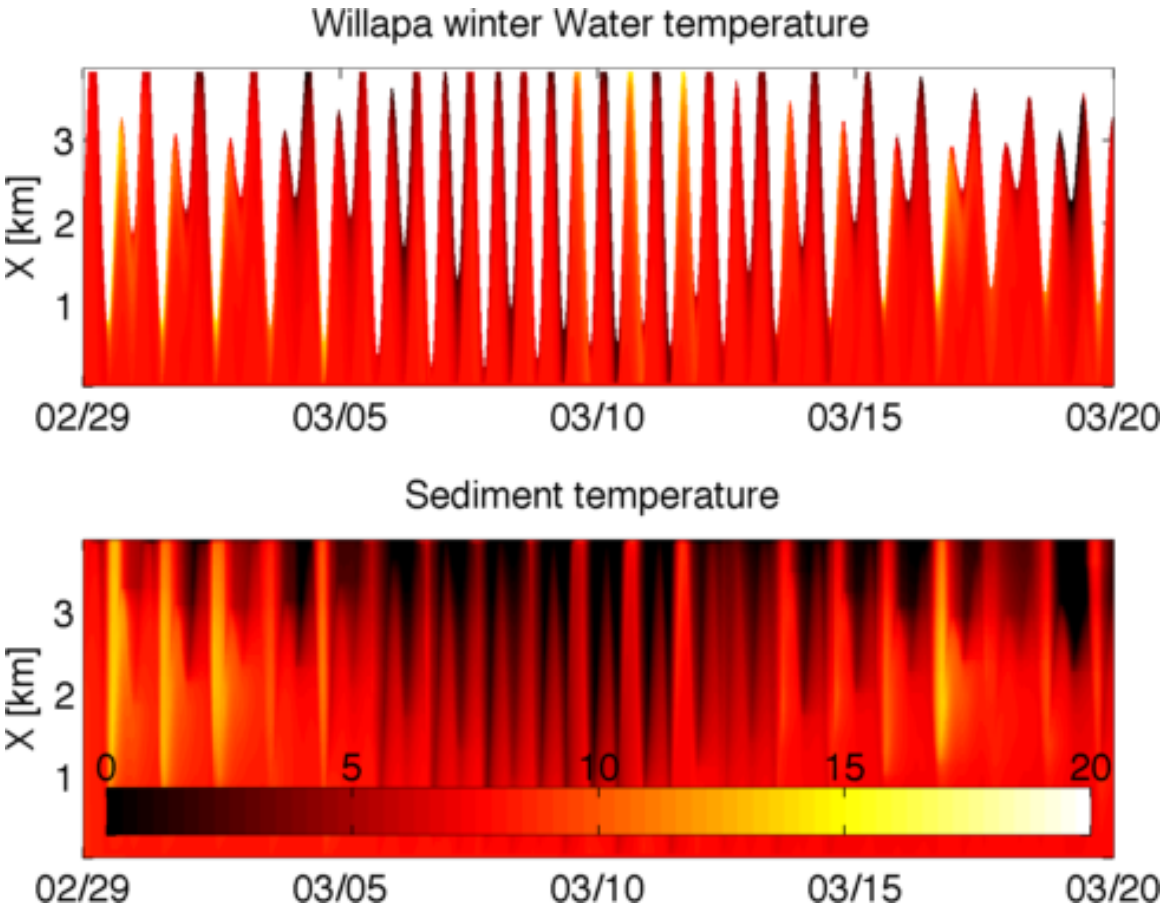

Figure 4.5 Model Willapa winter (a) water and (b) sediment temperatures varying in time and cross-shore distance with $K_d = 1000$ m^{-1}. White areas in the water temperatures indicate the cell is dry.

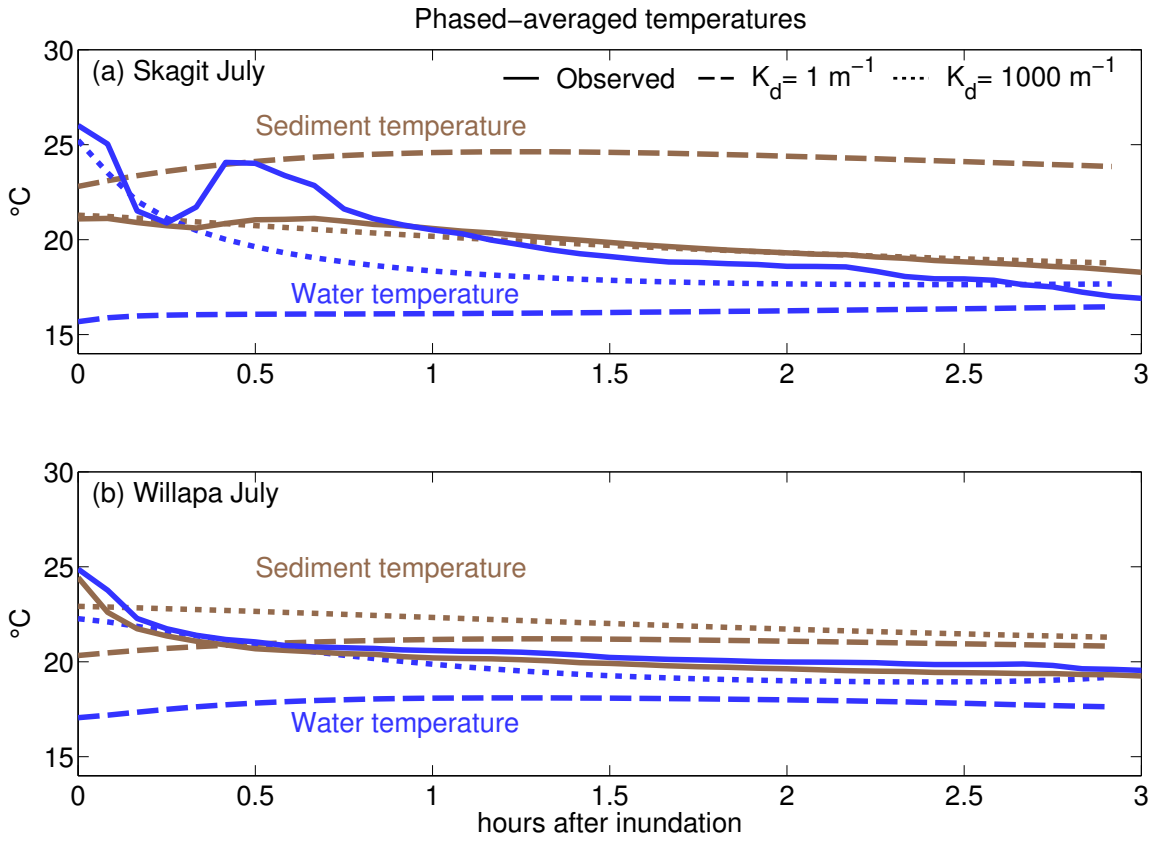

Figure 4.6 Tidally phase-averaged water (blue) and sediment (brown) surface temperatures for (a) 13-18 July 2009 at Skagit Bay and (b) 21-28 July 2009 at Willapa Bay. The x-axis increases from 0 at the time of inundation to 3 hrs after inundation. Solid lines are the observed temperatures, dashed lines indicate an extinction coefficient of K_d =1000 m^{-1}, and dotted lines K_d = 1000 m^{-1}.

indicates the direction of sediment water heat flux. This pattern indicates that initially, water flooding over the flat is transferring heat into the sediment bed, but as time goes on the direction of transfer reverses with the sediments acting as a heat source. Under the low K_d conditions, however, this pattern does not occur. Water temperatures do not get much higher than the offshore temperature and then show only a slow increase in the hours following inundation. Sediment temperatures during the low K_d case are much higher than the observed values and stay high despite the inundation.

At Willapa Bay, observed sediment and water column temperatures track more closely together. Water temperature at inundation is only about 0.5°C greater than the sediment temperature and remains so throughout the following 3 hours. Initially both are high and decrease as time advances. Both the high K_d and the low K_d models are unable to capture this feature. Overall, however, modeled temperatures for the high K_d model are closer to the observed values with model-observation differences of about 1°C by 1 hour after inundation. For the low K_d model, the water and sediment temperature difference is much greater than observed and continues throughout the whole period.

4.3.2 Lagrangian heating at the front edge

Lagrangian averaging of the model results at the front edge allows us to determine the source of heating at the flooding front. The distance from the leading edge of the front was determined and then the model results were averaged over each of these distances. This process was performed for both sets of K_d values. This allows us to follow heating of the average water parcel with time as it moves across the flat surface.

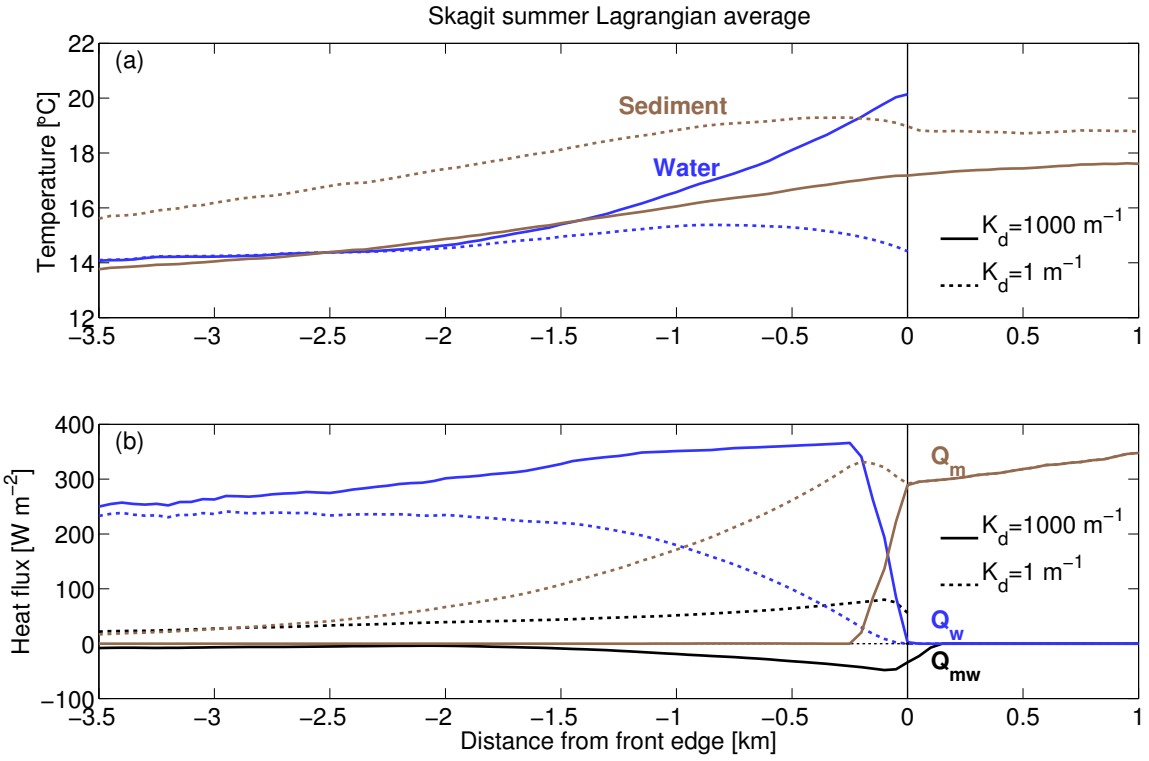

Figure 4.7 Langrangian average of Skagit summer temperatures and heat fluxes. (a) (blue) Water and (brown) sediment temperatures. (b) Total heat flux to (blue) water column and (brown) sediment. (black) Sediment-water heat flux. Solid lines indicate K_d =1000 m^{-1} while dashed lines indicate $K_d = 1$ m^{-1}

Figure 4.7 shows the Lagrangian average of the water and sediment temperatures and associated heat fluxes at Skagit Bay during the summer period for each K_d value. At the leading front edge water column temperatures are on average 3°C warmer than the sediment temperatures. About 1 km behind the front edge, water temperatures become cooler than the sediment temperatures. Strong water column heating at the front edge is the source for this increased temperature. As the distance from the front increases the water and sediment temperatures return to the offshore average values.

For the decreased K_d case, sediment temperatures are 2 °C warmer than for the high K_d case. Water column temperatures cool as nearer the front edge. The high and low K_d cases converge about 2 km behind the front edge for the water temperatures where they approach the offshore value.

During the winter Figure 4.8, the difference between the two K_d cases is much less pronounced. As incident solar shortwave radiation is much lower during this period, water temperatures are less than 1°C different between the two cases. Sediment temperatures are nearly the same. Also, both cases show increased cooling at the leading edge of the front cause water temperatures to be less than sediment temperatures in both cases.

Lagrangian water temperatures at Willapa Bay during the summer (Figure 4.9) are similar to those at Skagit Bay, but Willapa Bay sediment temperatures remain higher than the water temperatures even in the high K_d model. As you move back from the edge of the front, water temperatures increase in the low K_d case and decrease in the high K_d case. The mechanism behind this is revealed in the plots of averaged solar shortwave radiation with very little shortwave radiation absorbed at the front edge during the low extinction coefficient run. Because there's little input of energy at the front edge, the leading edge cools as the sediment-water heat exchange is not great enough to balance loss of heat due to longwave, sensible, and latent fluxes. As expected, sediment-water heat fluxes are also greater during the low K_d model due to the large differences in sediment and water temperature, but they're not large enough to offset the losses from other sources and temperatures drop.

Winter results at Willapa (Figure 4.10) have a similar pattern to Skagit with temperatures decreasing towards the front edge, however sediment and water column

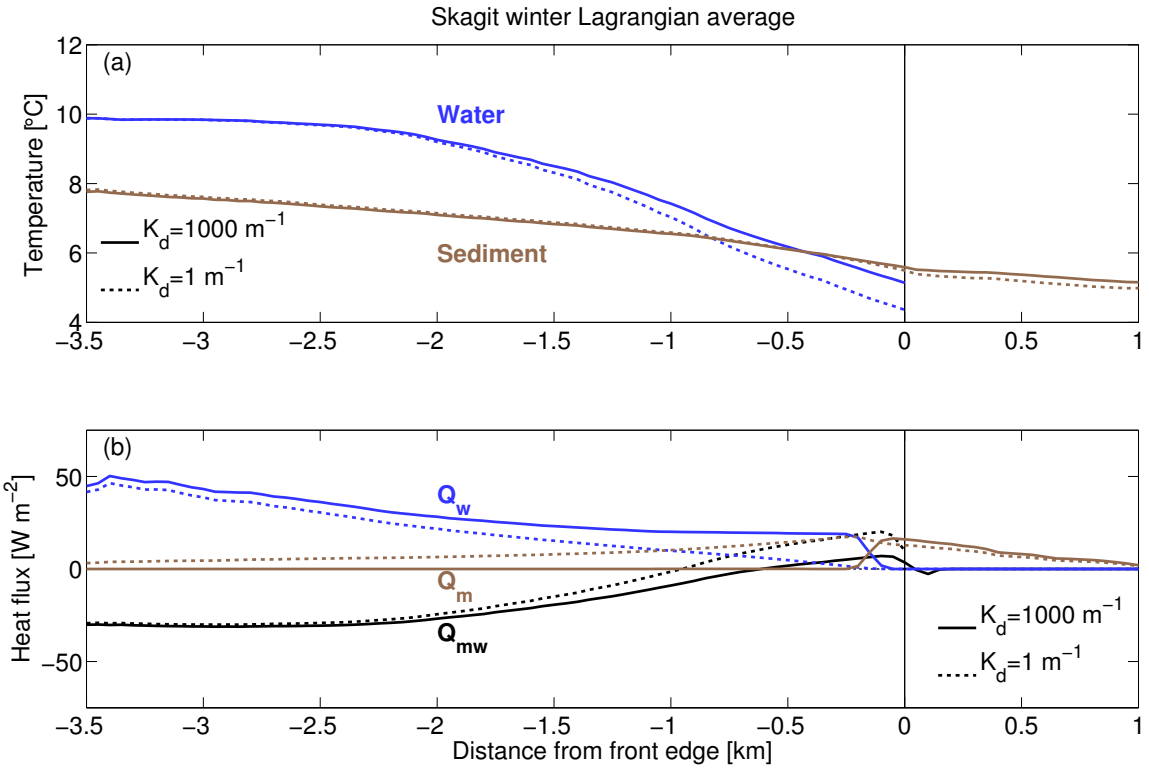

Figure 4.8 Langrangian average of Skagit winter temperatures and heat fluxes. (a) (blue) Water and (brown) sediment temperatures. (b) Total heat flux to (blue) water column and (brown) sediment. (black) Sediment-water heat flux. Solid lines indicate K_d =1000 m^{-1} while dashed lines indicate K_d = 1 m^{-1}

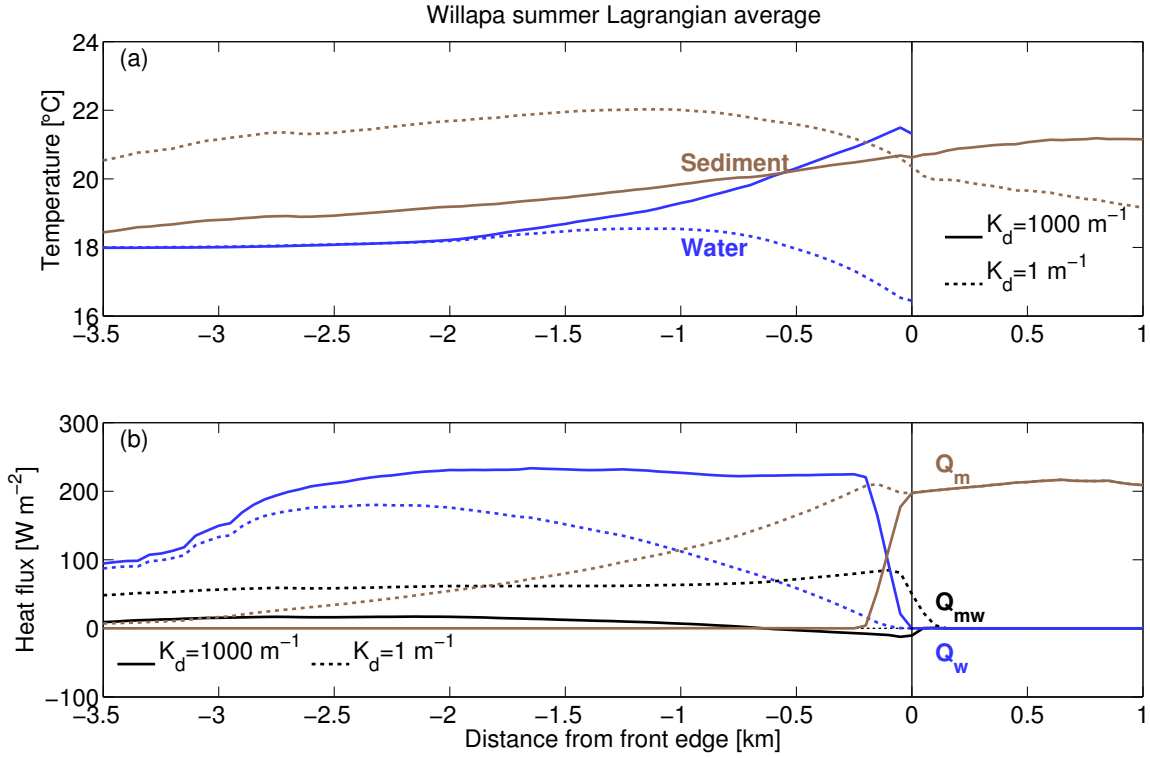

Figure 4.9 Langrangian average of Willapa summer temperatures and heat fluxes. (a) (blue) Water and (brown) sediment temperatures. (b) Total heat flux to (blue) water column and (brown) sediment. (black) Sediment-water heat flux. Solid lines indicate K_d =1000 m^{-1} while dashed lines indicate $K_d = 1$ m^{-1}

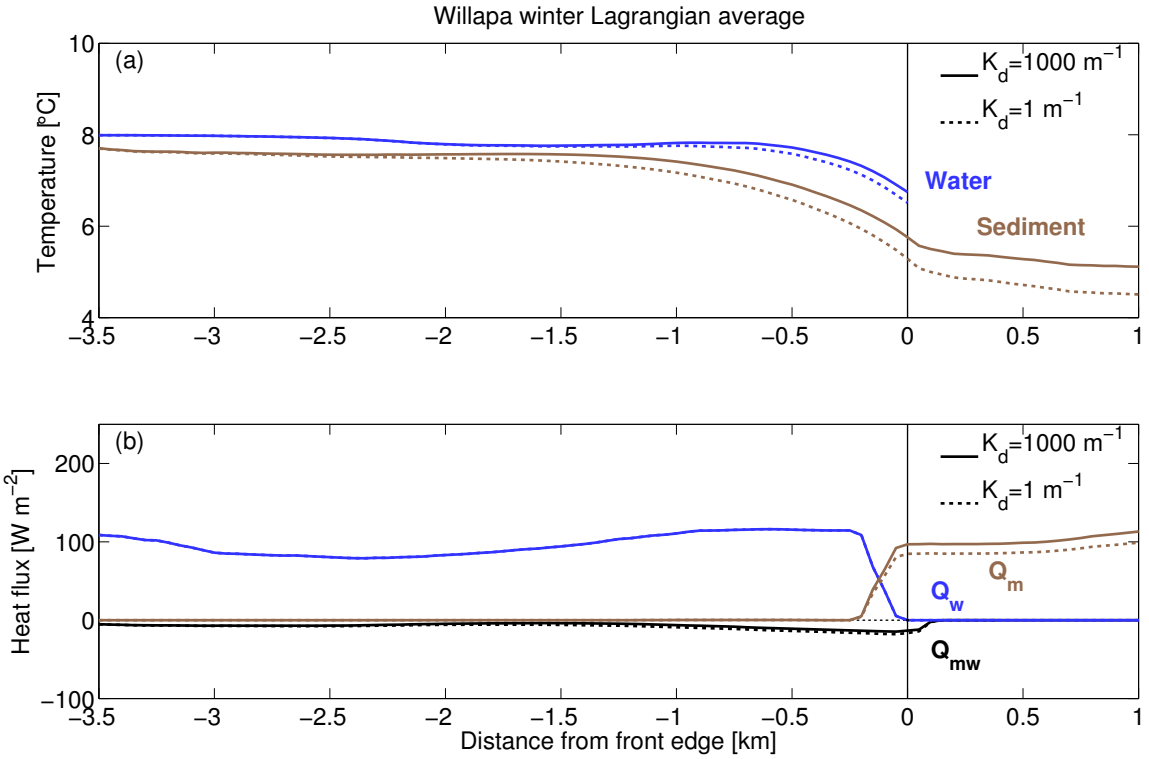

Figure 4.10 Langrangian average of Willapa winter temperatures and heat fluxes. (a) (blue) Water and (brown) sediment temperatures. (b) Total heat flux to (blue) water column and (brown) sediment. (black) Sediment-water heat flux. Solid lines indicate K_d =1000 m^{-1} while dashed lines indicate K_d = 1 m^{-1}

temperature difference is lower, only about 1°C over most the distance. Sediment water temperature differences increase around 1 km behind the flat and reach a maximum of about 2°C at the front edge. Because the "winter" model at Willapa occurs during March, solar forcing is stronger than during the winter Skagit run in January. This likely explains the relatively constant temperatures between -3 and -1 km from the front.

4.4 Discussion

Interstingly, the results of the low extinction coefficient models during the summer share the same patterns as the winter runs with either high or low extinction coefficients. This likely follows from the limited solar radiation during the winter periods. As the low K_d models would limit shortwave radiation being taken up by the water column, it should mimic periods, like the winter, where shortwave radiation is at it's minimum. During the Willapa "winter" model this effect is diminished due to the relatively high solar radiation in March versus the Skagit winter period of January. Despite the large sediment-water temperature differences, h_{sw} is too small to rapidly equilibrate the sediment and water temperatures causing both winter and low K_d summer water temperatures to drop at the front edge.

While high K_D were necessary to accurately determine the post-inundation water and sediment temperatures the use of a constant attenuation coefficient in both space and time was necessitated by available observations. Phase-averaged water temperatures at Skagit Bay show a distinct double peak at the initial inundation and 30 minutes afterwards which the model is unable to replicate. It is likely that along flat convergence during the flood tide or the effects of river outflow, processes not included in the model, create a double peak in turbidity that causes enhanced absorption of shortwave radiation. Aerial photography (Figure 4.11) taken in the same region of the flat, but at a different time, clearly shows the interaction of two fronts and a double peak in turbidity near the site. Spatial and temporal variability of K_d, i.e. by assigning a turbidity dependent value would be required to capture this signal.

It is also important to note that the K_d values necessary to replicate the enhanced water temperatures at the edge of the front are an order of magnitude above

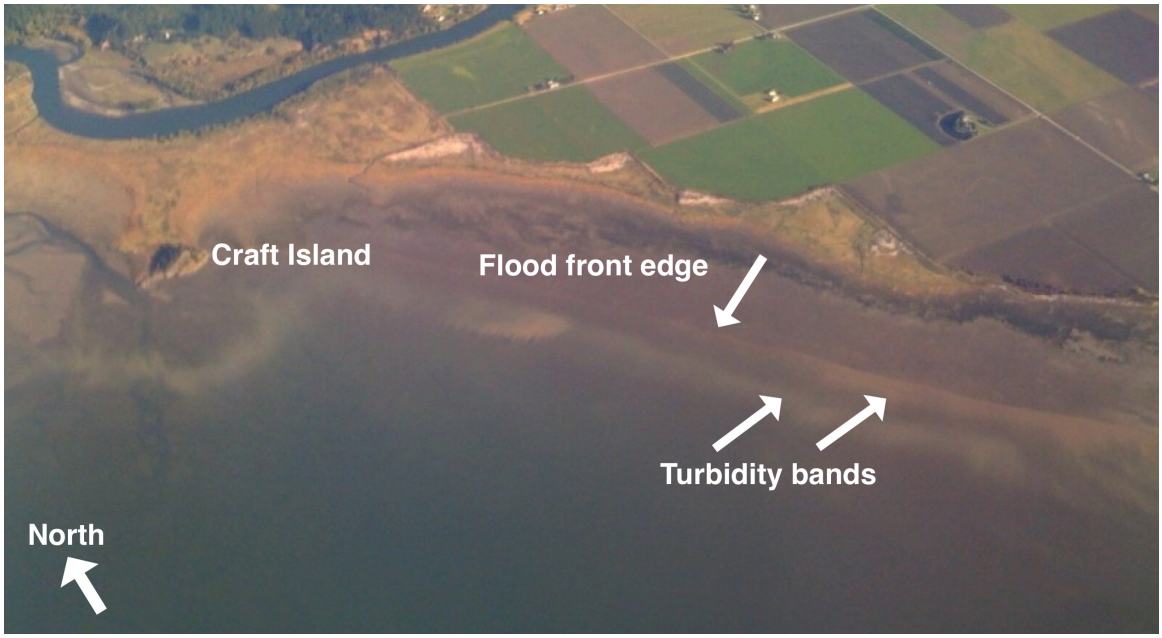

Figure 4.11 Oblique aerial photograph of North Skagit Bay showing turbid water near the flooding front. Two bands of turbidity associated with the edge of the front are indicated.

the greatest values (100 m^{-1}) reported for just the infrared portion of the incoming radiation. Most observations of light extinction coefficient occur in water depths O(1-10m) where back-radiation of shortwave energy is less than 1% of the incoming radiation (Stefan et al., 1983). Considering the extremely shallow, centimeter scale flows that occur at the edge of the flooding front, it's likely that back-radiation and reabsorption of shortwave radiation occurs causing the simple one-directional model of Eq. 4.1 to under predict the fraction of shortwave radiation absorbed by the water column and hence require larger extinction coefficients.

4.5 Conclusions

This chapter examined the heat fluxes at the leading edge of the flooding front and the role of the extinction coefficient K_d in controlling the uptake of shortwave radiation. Two different end-member cases of extinction coefficient values were used, K_d= 1 m^{-1} and K_d=1000 m^{-1}. Model results using the high extinction coefficient more closely matched the observed values, suggesting that strong solar absorption due to turbid flooding waters could be an important mechanism to maintain high water temperatures at the edge of the front.

Water temperatures during the summer low K_d cases more closely resemble winter water temperatures with the leading edge of the front cooling compared to a few km behind the front. Without significant solar forcing of the front edge, longwave, latent, and sensible fluxes are strong enough to cool the thin layer of water.

Chapter 5

HEAT AND MASS TRANSPORT DURING EBB DRAINAGE AND RUNOFF [1]

5.1 Introduction

Fine-grained intertidal flats provide habitat for many aquatic species and economic value for fisheries, but their complex environment makes field observations of water and sediment dynamics difficult. Variations in water depth during the tide transform the hydrodynamic environment between a shallow embayment at high tide and a drainage basin at low tide (Le Hir et al., 2000). Within this complex spatial arrangement and varying scales of motion, incised channels convey water and sediment throughout the system (Ralston and Stacey, 2007). It is well known that channels play an important role in the later stages of receding ebb tidal flow (Wood et al., 1998; Nowacki and Ogston, 2012) conveying water on the flats downstream. Water continues to flow out through these channels long after the ebb tide has passed (i.e., after the tide water is below a given location on the flats) (Whitehouse et al., 2000). Although this 'post-ebb discharge' is common, there has been limited quantitative description or dynamic understanding of these flows.

Recent work suggests that post-ebb discharge in channels results from the runoff of remnant water on the surface of the tidal flat (Mariotti and Fagherazzi, 2011;

---

[1]This chapter published as: Rinehimer, J.P., Thomson, J. and Chickadel, C.C. (2013). Thermal observations of drainage from a mud flat. Continental Shelf Research, http://dx.doi.org/10.1017/j.csr.2012.11.001.

Whitehouse et al., 2000; Allen, 1985) and that runoff patterns control the distribution of many aquatic species (Gutiérrez and Iribarne, 2004). Other studies suggest the post-ebb drainage results from porewater discharge from with the flats, although it is a much slower process (Anderson and Howell, 1984). From either source, these studies agree that post-ebb drainage can be an important mechanism for the transport of water, sediment, and heat.

The drainage of remnant surface water via nearly parallel, ridge-separated channels located on the flat surface called runnels may be particularly important for off-flat transport (Fagherazzi and Mariotti, 2012; Gouleau et al., 2000). Thus, a mass budget for a tidal flat system is incomplete without quantification of post-ebb drainage. For example, in a study of a nearby channel in Willapa Bay, Nowacki and Ogston (2012) find that an equilibrium sediment budget requires additional export that is missing from their analysis of purely tidal flows. Although post-ebb channel discharge appears small by qualitative (visual) observation, recent work by Fagherazzi and Mariotti (2012) has shown that shear stresses due to this process are higher than the critical stress for erosion and that suspended sediment concentrations are greater than during tidal flows. Kleinhans et al. (2009) found post-ebb surface velocities of 0.1-0.2 ms^{-1} and showed that the post-ebb flow controlled channel meandering, as well as bank and backward step erosion in the incised channels.

Estimation of channel discharge requires knowledge of depth and cross-sectionally averaged velocities at all stages of the drainage. One reason that post-ebb drainage has not been well described is the difficulty in measuring very shallow (depth less than 10 cm) flows. Here, we utilize a novel technique to measure shallow flows remotely with infrared (IR) images. The IR method is combined with conventional acoustic

Doppler measurements during periods of greater depth, and there is good agreement between the two approaches during these periods. The integration of these data sets provides a continuous time series of the channel discharge velocities. Furthermore, the IR imagery measures the horizontal (cross-channel) variations in surface velocity allowing greater detail on the flow structure to be observed in addition to the vertical velocity profiles from the in situ measurements. Parametric fits for these profiles are then used to make continuous estimates of the volume flux discharged from the channel.

In addition to describing the structure and magnitude of the channel drainage, we compare the temperature of the drainage water to a model prediction for the temperature of remnant surface water (i.e., the hypothetical source of the post-ebb drainage). The model formulation follows Kim et al. (2010), in which the terms of surface heat fluxes are prescribed and the heat exchange between water and sediment is modeled explicitly. The model predicts remnant surface water temperatures that match the observed drainage temperatures and thus support the hypothesis of surface runoff. The corresponding total transport of heat is placed in context with previous observations of low tide heat budgets in muddy tidal flats.

5.2 Methods

5.2.1 Site description

Willapa Bay, Washington (Figure 5.1) is located on the Pacific coast of the United States, north of the Columbia River mouth. The Long Beach peninsula separates the estuary from the ocean with an 8-km-wide inlet at the northern end of the bay. The tide is mixed semidiurnal with a mean daily range of 2.7 m, varying between 1.8

m (neap) and 3.7 m (spring). The intertidal zone occupies nearly half of the bay's surface area (Andrews, 1965) and almost half of the bay's volume is flushed out of the bay each tide (Banas et al., 2004). Extensive tidal flats occupy much of the bay's intertidal region. Silt and clay sediment predominates in the southern bay and lower energy environments, while fine sand flats are found in higher energy areas, such as along the major channels and locations exposed to waves (Peterson et al., 1984).

The study site is located at the mouth of "D Channel" (46° 23′ 26.12″ N, 123° 57′ 43.26″ W) in the southern portion of the bay near the Bear River Channel. The Bear River Channel is the tidal extension of the Bear River which drains into the bay approximately 2 km south of D Channel. D Channel is a branching, dead end channel (Ashley and Zeff, 1988) that drains 0.3 km^2 of tidal flats into the Bear River channel. At our study site, the channel is incised into the flat about 0.7 - 1 m deep and 1 - 2 m wide.

The focus of study is a single spring tide on 31 March 2010. Lower-low water occurred at 10:00 (all times referenced in this paper are local, Pacific Daylight Time) while the period where the regional water level was below the mouth of D channel and all the surrounding flats exposed, (see Figure 5.1), lasted approximately 1.5 hours, from 09:15 to 10:45. During this period water was observed to continually drain out from D channel. We define this as the 'post-ebb discharge', because the ebb tide effectively finished (i.e., passed the site) at 09:15 and the flood tide did not inundate D channel until 10:45 . This period is distinct from the ebb-tide pulse which occurred earlier (approximately 08:00) when the tidal elevation was near the flat elevation.

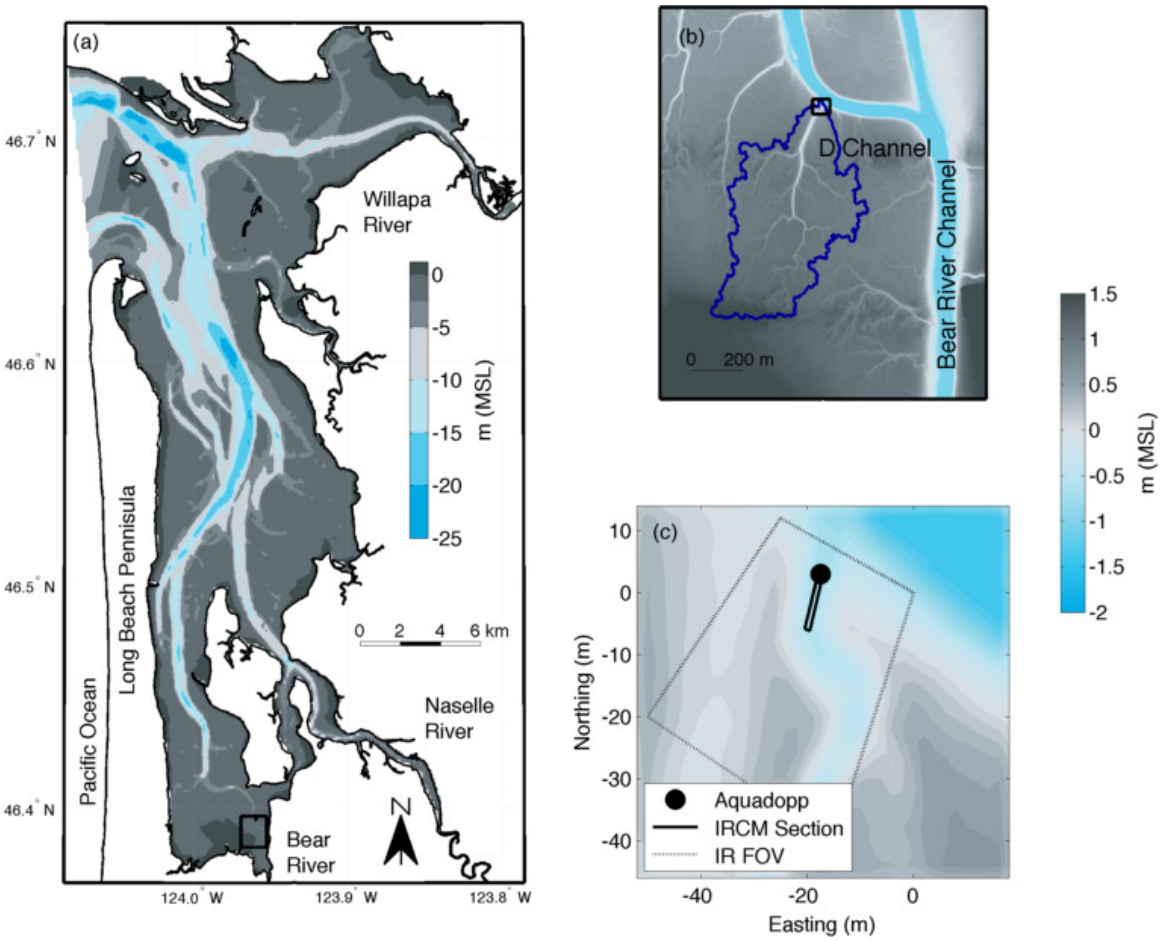

Figure 5.1 (a) Willapa Bay bathymetry. The black box indicates the region of sub panel (b) bathymetry of D Channel from LiDAR survey and the calculated drainage area. The black box indicates the D Channel mouth shown in (c) Close-up of D Channel mouth with locations of field instruments. The circle indicates the location of the Aquadopp ADCP, the line is where the IRCM timeslices were taken (See Section 5.2), and the trapezoid is the infrared camera field of view from the imaging tower at the local origin [0,0]. Bathymetry for (a) is indicated by the inset color bar whereas the right color bar shows the scale for (b) and (c).

5.2.2 In-situ measurements: velocity, temperature, and meteorology

A bed-mounted uplooking 2 MHz Nortek Aquadopp Acoustic Doppler Current Profiler (ADCP) located at the mouth of D-Channel recorded velocity profiles at 1 Hz with a vertical resolution of 3 cm and a 10 cm blanking distance. The Aquadopp was used in HR (high resolution) pulse coherent mode to obtain fine-scale vertical resolution, with a vertical profiling distance of 1 m. Aquadopp measurements with a pulse correlation below 40 (out of 100) are excluded from analysis, as are the two bins nearest the surface water level (as determined from the Aquadopp pressure gauge). The Aquadopp also measured water temperature in the channel.

Meteorological data were collected from an Onset HOBO met station mounted to a piling at the mouth of D channel, as well as from a Washington State University AgWeatherNet station approximately 5.5 km southwest of D channel (on land). Meteorological data include rainfall, which is known to enhance runoff from tidal flats (Uncles and Stephens, 2011). For the period surrounding the low tide of 31 March 2010, there was trace rainfall (less than 0.25 mm) during two 15 minute periods for a maximum possible rainfall of 0.5 mm.

Time series of sediment temperature profiles were collected with ONSET HOBO Temp Pro v2 temperature data loggers mounted on sand anchors and buried both within D channel at the Aquadopp location and on the flanking flats (Figure 5.1). In addition, a HOBO U20 water level and temperature logger was positioned on the sand anchors at the flat's surface (0 cm) to obtain temperature and pressure measurements. The temperature was sampled every 5 minutes, which is more than twice the response time of the instruments. A string of temperature loggers was also attached to a piling at the mouth of D Channel to measure conditions in the Bear

River Channel. Pressure loggers at the top and bottom of the logger string were used to correct the pressure measurements from the Aquadopp and HOBO pressure loggers for atmospheric pressure to obtain accurate measurements of flow depth.

5.2.3 Remote sensing measurements: infrared images and LiDAR scans

An infrared (IR) imaging system was deployed on a 10 m tower attached to the D Channel piling. IR data were collected at 7.5 Hz with a 320 x 240 pixel 16 bit 8-12 μm thermal camera (FLIR A40) with a 39° horizontal field of view lens oriented along the channel axis. A 66° incidence angle provided an imaged area of approximately 100 m by 40 m and a horizontal resolution of O(1 cm) in the near-field degrading to O(2 m) in the far-field. The gradient in resolution is a result of perspective (Holland et al., 1997).

To calculate the surface velocities when the local water depth was below the Aquadopp 0.1 m blanking distance, a Fourier transform based method was used to convert the infrared signal into a time-series of surface velocities. This Optical Current Meter method has been successfully used to compute nearshore surface currents (Chickadel, 2003) and breaking wave speeds (Thomson and Jessup, 2009). This study extends the method to computing surface velocities in the shallow channel using the infrared video and is renamed the Infrared Current Meter (IRCM). Traditionally, IR techniques rely on the cool-skin effect to provide flow signatures. Because this study was performed during daytime with significant solar heating, the cool-skin effect was not observed. Instead, surface bubbles advecting with the flow formed the major signal during the deployment. The thin film of the bubble cools faster than the surface water creating a strong signal against the warm channel outflow. The IRCM technique follows the Optical Current Meter (OCM) of Chickadel (2003) and therefore

only a brief overview will be given below.

The infrared data were georectified to a local coordinate system (Holland et al., 1997) to obtain a two-dimensional time series of pixel intensity with a resolution of 3.8 cm. After georectification, a 4 m slice (pixel array) of the imagery along the channel axis and just upstream of the Aquadopp was taken and converted into time stacks $I(t,x)$ (Figure 5.2). Time stacks show the evolution of the video along a single line of pixels in time. In practice, multiple lines are used to determine the surface currents at different positions across the channel. The pixel intensities were transformed into the frequency-wavenumber domain $\hat{I}(f,k)$ using a two dimensional Fourier transform,

$$\hat{I}(f,k) = \int\int B(t,x)I(t,x)e^{-i2\pi ft}e^{-i2\pi kx}dtdx \tag{5.1}$$

where f is the frequency (Hz) , k is the wavenumber (m^{-1}), and $B(t,x)$ is a two dimensional Bartlet filter (Press et al., 2007) to reduce spectral leakage. The spectral power, $S(f,k) = \hat{I}(f,k)\hat{I}^*(f,k)$, where the star (*) indicates the complex conjugate, was then computed and the spectrum was converted to velocity-wavenumber space using the mapping $v = fk^{-1}$. The transformation is

$$var\{S(f,k)\} = \int\int S(f,k)dfdk = \int\int S(v,k)|k|dvdk \tag{5.2}$$

where $|k|$ is the Jacobian determinant and $S(v,k)$ is the velocity-wavenumber spectrum. Following this transformation preserves the variance of the signal. The frequency and wavenumber are constrained during this integration so that the velocities lie between ± 2 m s^{-1}.

Following the transformation to velocity-wavenumber spectrum $S(v,k)$, the velocity spectrum $S(v)$ is then obtained by

$$S(v) = \int_{k_{min}}^{k_{nyq}} S(v,k)dk \tag{5.3}$$

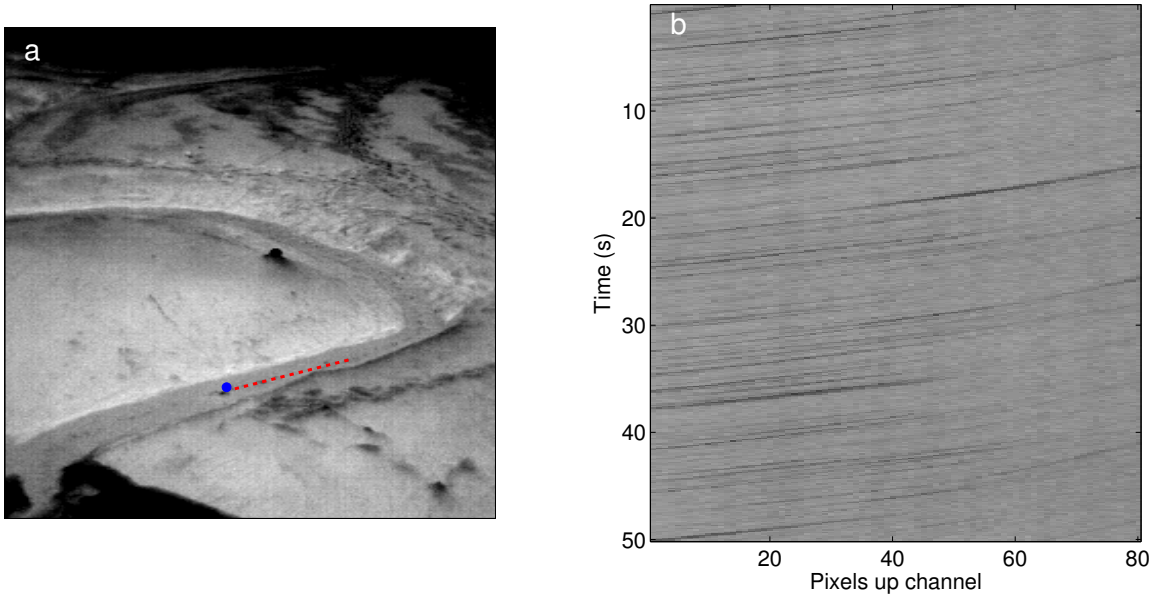

Figure 5.2 (a) Example (unrectified) IR imagery of D Channel from the tower at 10:30. Warmer regions are brighter. D channel curves from the left edge of the image to the right and drains into the cold (black) Bear River Channel at the bottom of the image. Dark spots within the channel are bubbles on the water surface while the dark spots on flats are footprints from the instrument deployment the previous day. The dark object in the center is a buoy on the flat surface used for rectification and the blue dot is the location of the Aquadoppp. The red dashed line represents the pixel array used to generate the (b) timestack (time-series of pixel intensities) from the same time. The black streaks moving through the time stack are bubbles on the water surface.

where $k_{nyq} = 1/2\,dy = 13$ m^{-1} is the Nyquist wavenumber and $k_{min} = 0.33$ m^{-1} was chosen to minimize bias from low wavenumber noise. The $S(v)$ spectrum was then fit to a model assuming a Gaussian velocity distribution combined with white noise to obtain an estimate of velocity for that spectrum and a 95% confidence interval for the velocitiy was determined from a nonlinear least squares fit (See Chickadel, 2003, for details). The video data were binned into 256 sample timestacks with 50% overlap and the above procedure run on each segment of video providing a timeseries of velocities with a period of 17.1 s from the initial 7.5 Hz video.

Additionally, a Riegl LMS-2210ii, (905 nm) LiDAR was used to measure the elevation of the tidal flats. A scan was performed at low tide and gridded to a resolution of 10 cm. These data provided accurate measurements of the channel cross-sectional area to perform volume flux calculations (see Section 5.3). A larger-scale LiDAR dataset, obtained from USGS was used to estimate the size of the drainage basin captured by the 'D' channel during low tide exposure.

The channel bathymetry was constructed from the LiDAR scan taken at maximum low tide. As the 905 nm LiDAR cannot penetrate the water surface, some additional interpolation was required to reconstruct the full channel bathymetry. The portion of the channel occupied with water was identified and the center of the channel was assigned the measured water depth at the sand anchor that was co-located with the Aquadopp. The bathymetry of the inundated portion of the channel was then interpolated as a cubic spline fit to the exposed channel area.

5.3 Results

5.3.1 Channel currents and temperature

Along channel velocities from the co-located Aquadopp and IRCM measurements are shown in panels (a) and (b) of Figure 5.3, along with tidal elevation. During the ebb, maximum observed velocities occur as the water level approaches the flat elevation of about 1 m relative to the channel bed at 08:00. This is consistent with the maximum rate of change in the instantaneous tidal prism (i.e., the volume of tide water) going from the flat to the channel and corresponds to the ebb pulse (Nowacki and Ogston, 2012). Across-channel velocities (not shown) in the lower meter are typically small, but may increase in the region above the 1 m sampling distance when the tidal elevation is above the flats and the tide propagates across the flats, as seen in Nowacki and Ogston (2012) and Mariotti and Fagherazzi (2011). At 09:15, the ebb passes the Aquadopp site and the measured water depth in the channel becomes constant at 0.1 m (the surrounding flats are exposed). The water in the channel continues to flow seaward, however the 0.1 m flow depth is within the acoustic blanking distance of the instrument. Although the pressure and temperature measurements are still valid, no useful Doppler velocity data are collected during this shallow flow. The IRCM shows that channel drainage continues and is characterized by a slow decrease in velocity (until the next flood tide when water from the Bear River Channel enters D Channel).

When both the IRCM and Aquadopp measurements are valid, the measurements from the top bins of the Aquadopp compare well with the results of the IRCM technique (Figure 5.4a). The overall correlation between the currents speeds is $r^2 = 0.82$. (Figure 5.4). The 95% confidence intervals around the IRCM calculations span from ± 0.5 cm s^{-1} to ± 2.5 cm s^{-1} with a median of ± 1.7 cm s^{-1}. This is significantly smaller

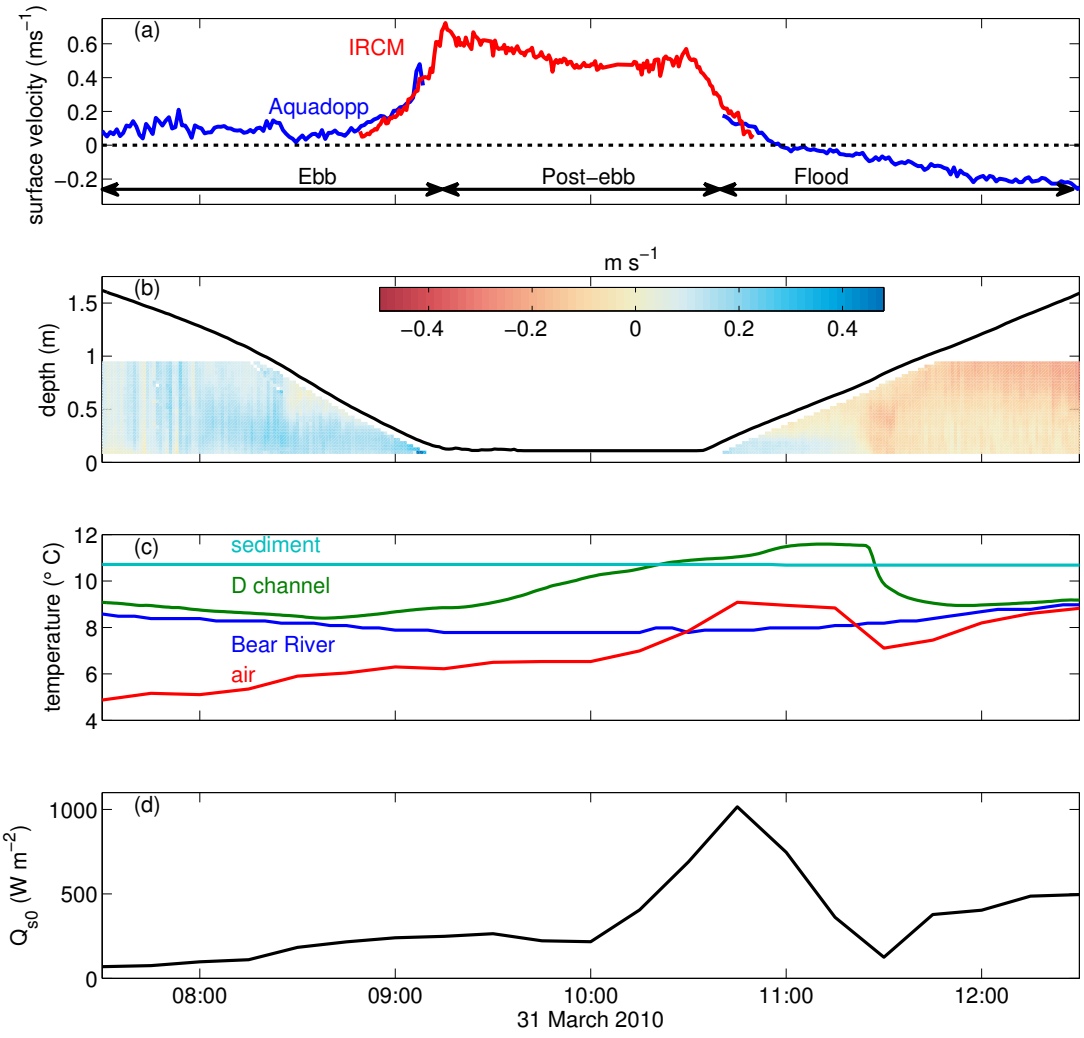

Figure 5.3 Observed time series of (a) Aquadopp near-surface (blue) and IRCM surface (red) velocities, (b) water depth and along-channel velocity measured by the Aquadopp ADCP (c) temperature of the air (red), drainage water in D channel (green), sediment at depth (cyan) and in Bear River channel (blue), (d) incoming solar shortwave radiation Q_{s0}.

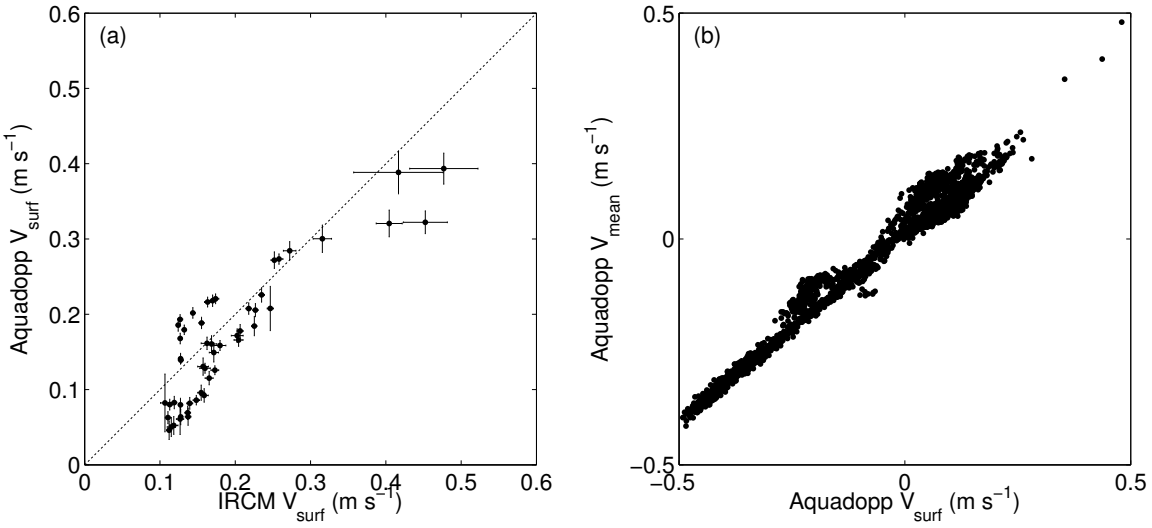

Figure 5.4 (a) Comparison of Aquadopp and IRCM measured surface velocities. Error bars are 95% confidence intervals around the modeled IRCM velocities and the dashed line indicate one-to-one correspondence. (b) Comparison of Aquadopp surface velocities to depth-averaged velocities.

than the errors expected from the raw (1 Hz) Aquadopp which are O(10 cm s^{-1}). Figure 5.4b also shows that surface velocities are well correlated with depth-averaged flow (panel b), suggesting that IRCM values, which are surface values by definition, can be used to estimate total discharge.

Also shown in Figure 5.3 are water temperatures (panel c), which vary notably in the D channel during low tide relative to the values downstream in the Bear River. The temperature signal is useful to constrain the source of the drainage, which is either remnant surface water, exfiltrating porewater, or rainfall. Remnant water is expected to have a strong thermal response to external heat fluxes, because of a small thermal mass and direct exposure to solar heating, convection by wind, etc. Figure 5.3 shows strong solar forcing (panel d) during the later stages of the post-ebb period. Thus, there are valid mechanisms for remnant water on the flats to undergo both the cooling

and the heating necessary to produce the observed channel outflow temperatures. Porewater, by contrast, is expected to have a very weak thermal response, because saturated muddy sediment within the flats are well-insulated from external heat fluxes and have a large thermal mass (Thomson, 2010).

5.3.2 Channel current profiles

For the purpose of estimating the total discharge and associated open-channel flow dynamics, the important parameter is the depth and cross-sectionally averaged channel velocity $\bar{v}(t)$. Here, we use observations of the depth and cross-channel profiles, when available, to scale factors such that the mid-channel surface velocities $v_{surf}(t)$ can be applied at all times to obtain

$$\bar{v}(t) = \frac{1}{A}\int_A v(x,y,t)dA = C_x C_z v_{surf}(t) \tag{5.4}$$

where the integral is taken over the channel area A and C_x and C_z are the horizontal and vertical scale factors, respectively. As only a small subset of the data has observations with both cross-channel and depth profiles simultaneously, the scale factors are necessary to obtain volume flux measurements.

The Aquadopp measures vertical profiles of the velocity, as shown in Figure 5.5 for select times. The profiles show unexpected sub-surface velocity maxima. Similar profiles have been observed in the late stages of channel drainage on other flats (Wells et al., 1990). Bottle samples taken from the channel outflow during these times show high suspended sediment concentrations, from 1.2 - 8.9 gL^{-1} at 08:42 and 10:15. Increased ADCP backscatter during these periods also suggests the presence of high suspended sediment concentrations indicating the possibility of suspended sediment supported gravity flows. Although our sparse observations of suspended

sediment concentration are insufficient to investigate the details of gravity flows, the quadratic fit describes the observations well and the high concentrations motivate the quantification of post-ebb drainage. Alternatively, surface stresses from wind and cross-channel circulation may be responsible for these sub-surface maxima.

The normalized velocity profiles are used to find the scalar constant C_z, which relates the observed surface velocity to the depth-averaged velocity, such that $\frac{1}{h}\int v(z)dz = C_z v_{surf}$. The factor C_z is thus the slope of the comparison in Figure 5.4b. This depth correction factor is assumed to apply across the entire channel, however the surface velocities v_{surf} are allowed to vary across the channel.

The cross-channel variations in surface velocity v_{surf} are quantified using multiple IRCM lines are shown in Figure 5.6 for selected times. The cross-channel profiles show an expected maxima mid-channel and a quasi-symmetric reduction near the channel side-walls, consistent with a no-slip condition along the walls. The normalized profiles are used to define a scalar constant C_x, which relates the observed surface velocity to the cross-channel-averaged velocity, such that $\frac{\int v(x)dx}{\int dx} = C_x v_{surf}$. The cross-channel correction factor is assumed to apply at all depths, however the velocity may vary with depth (as determined in the preceding definition of C_z).

5.3.3 Total channel discharge

The discharge (i.e., volume flux) outflowing from D channel is estimated using the measured surface velocities and applying the scaled profile coefficients, such that

$$\mathcal{V}(t) = \int\int v(y,z,t)dydz = \bar{v}(t)A(t) = C_y C_z v_{surf}(t)A(t), \tag{5.5}$$

where $v_{surf}(t)$ is the mid-channel surface measurement (from either the IRCM or the Aquadopp) at a given time, A is the channel cross-sectional area (determined from

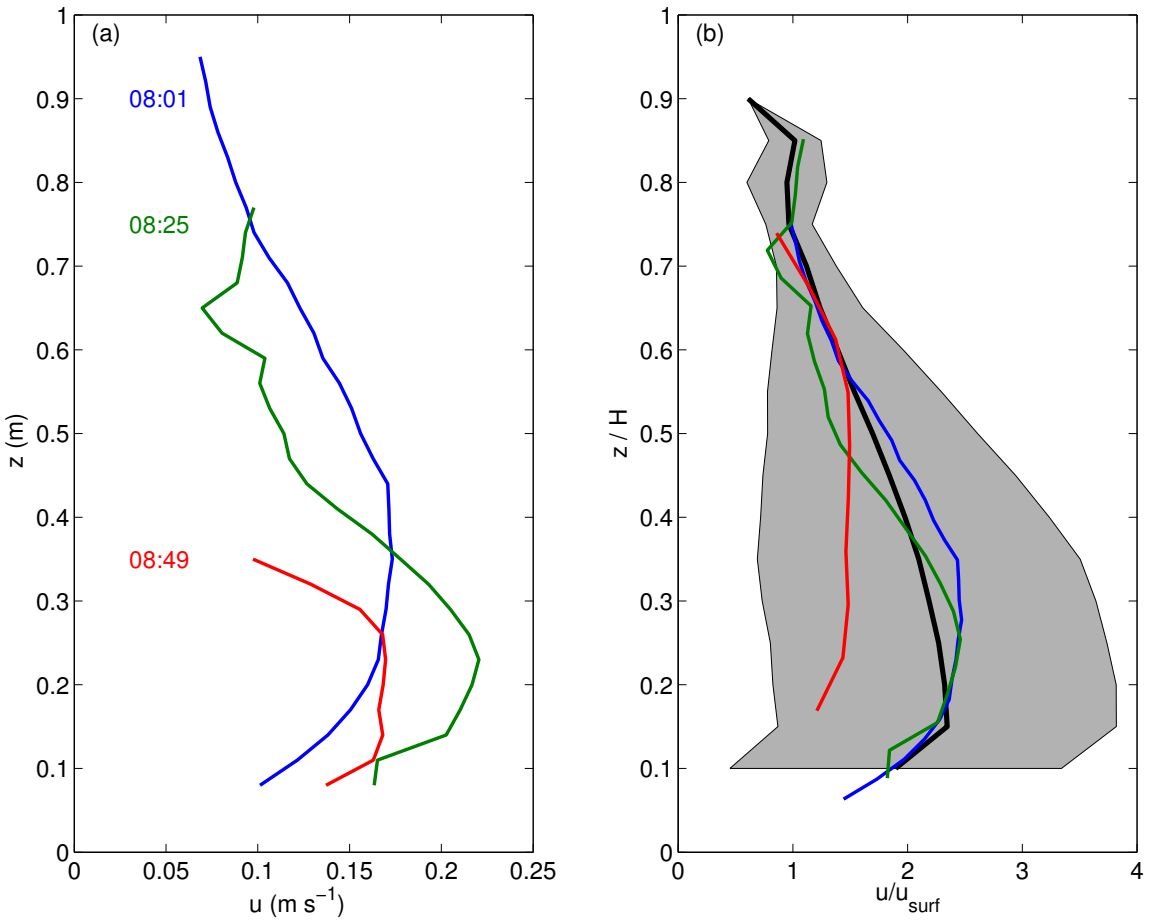

Figure 5.5 (a) Depth profiles of surface outflow velocity from the Aquadopp at various times, and (b) corresponding normalized profiles. The thick black line is the mean for all profiles and the gray shading is the standard deviation.

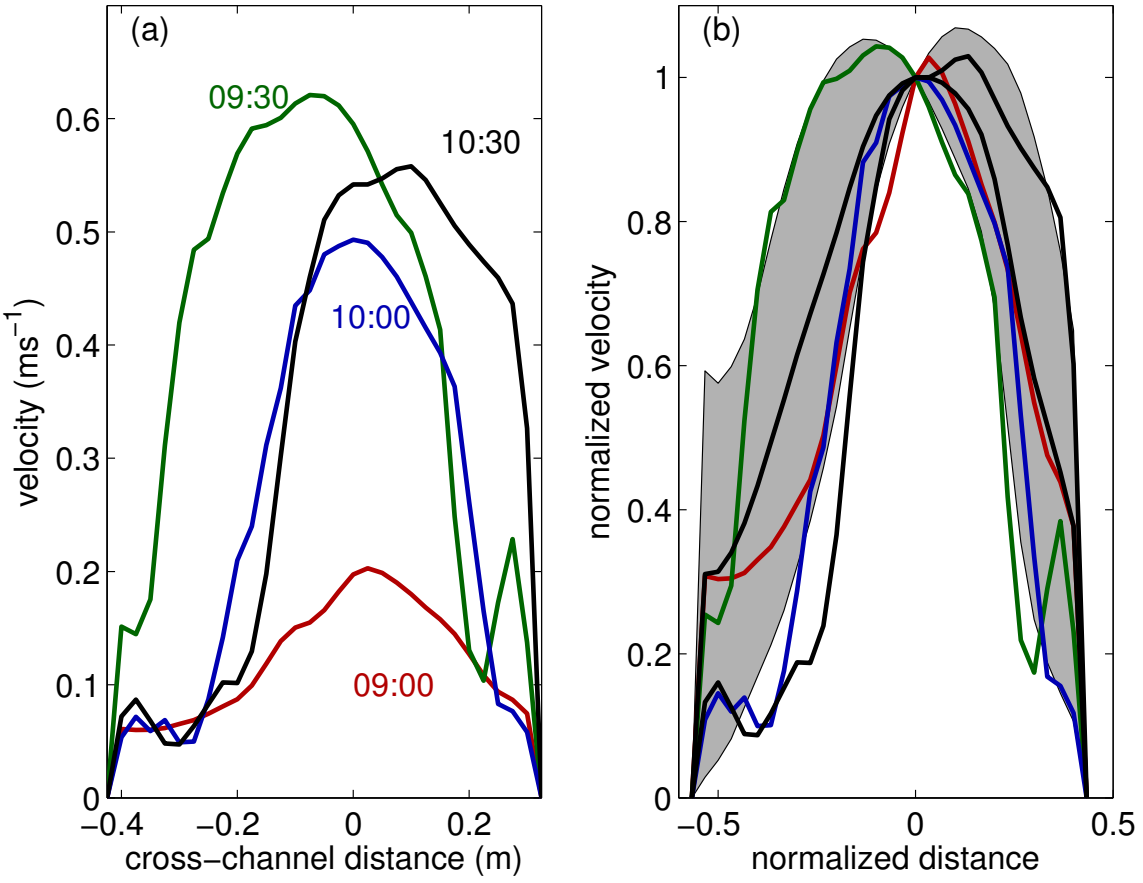

Figure 5.6 (a) Cross-channel profiles of surface outflow velocity from the IRCM at different times, and (b) corresponding normalized profiles. The thick black line is the mean for all profiles and the gray shading is the standard deviation.

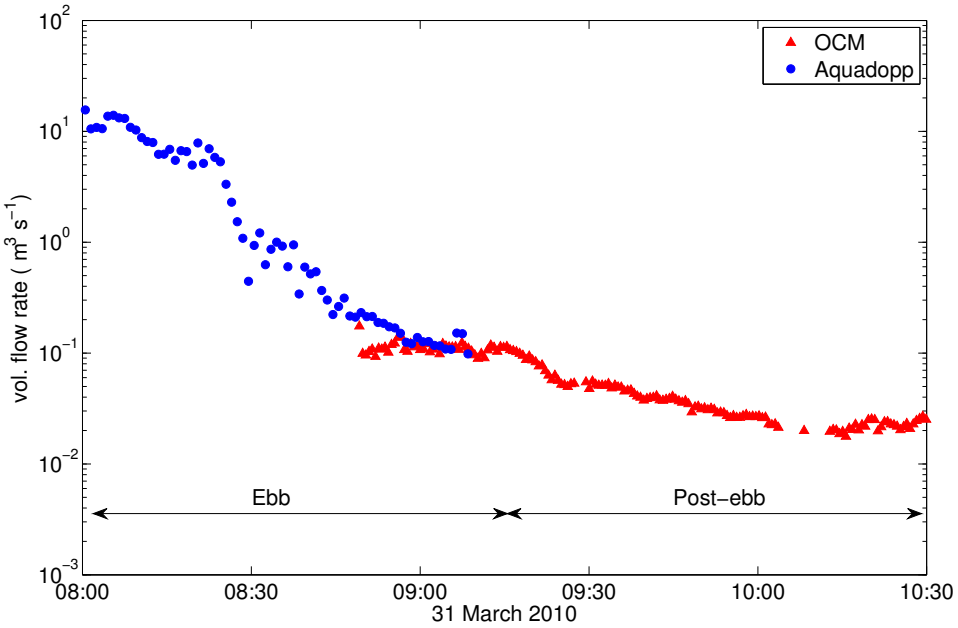

Figure 5.7 Time series of discharge (total volume transport) as calculated from the Aquadopp (dots) and IRCM (triangles) techniques. Ebb and post-ebb discharge periods are indicated by the labelled arrows.

the Aquadopp pressure gauge and the extrapolated LiDAR scan) at a given time, and C_x, C_z are the scale factors adjusting the observed surface velocity to a channel- and depth-averaged value.

The channel discharge from Eq. 5.5 is shown in Figure 5.7 on a log axis as a function of linear time. Discharge rapidly decreases during the end of the ebb and the rate of decrease slows during the post-ebb period. Generally, there is an exponential decay with time, consistent with the hydrographic recession of a drainage basin (Jones and McGilchrist, 1978; Brutsaert, 2005).

$$\mathcal{V}(t) = \mathcal{V}_0 e^{-\alpha t}. \tag{5.6}$$

Here the exponent α is determined to be approximately 3.7 hours^{-1} $\pm$ 0.54 during

the ebb and 1.5 hours^{-1} $\pm$ 0.08 for the post-ebb flow. This change in exponent indicates a change in the underlying dynamics from the ebb-tidal-elevation driven flow to a uniform open channel flow regime during the post-ebb period. While a visual inspection of the plot seems to indicate a change in slope somewhere between 08:45 and 09:15, the dynamic analysis in section 5.4.1 suggests 09:15 as the change in dynamic regime. For the purpose of this study, however, the exact time period does not significantly alter the results.

Integrating in time under the post-ebb discharge portion of the volume flux estimates gives a total outflow volume of approximately 400 m^3. Using the LiDAR data to delineate the upstream drainage basin, the upstream area is $A_{total} = 3 \times 10^5$ m^2 (see Figure 5.1b). Combining these estimates indicates that the observed drainage in the D channel would require a skim of approximately $d \sim 1.3$ mm deep remnant water on the surface of the flats. Of course, it is unlikely that the remnant water is uniformly distributed across the observed flats, because ridges and runnels are common to muddy tidal flats (O'Brien et al., 2000; Gouleau et al., 2000; Whitehouse et al., 2000). A more realistic guess at the distribution of remnant water thickness is $d \sim$ 13-26 mm over 5-10% of the exposed flats, and this estimate is used in subsequent thermodynamic modeling of the remnant water (to predict channel discharge temperatures, see §5.4.2).

Porewater and rainfall are potential alternate sources of the post-ebb discharge. Estimating the total major channel length from the LiDAR as 2 km and a mean channel depth of 0.5 m, the hydraulic conductivity along the channel flanks would need to be 10^{-3} cms^{-1} (assuming unit hydraulic gradient, i.e. 1 m change in head over 1 m horizontal distance) to generate the observed fluxes of 0.2 m^{3}s^{-1} via porewater

discharge. This is well above the 10^{-6} to 10^{-9} cms^{-1} estimates of hydraulic conductivity within Willapa mud flats (B. Boudreau, pers. commun.), and thus is unlikely to contribute noticeably to the source of post-ebb drainage. Another potential source is rainwater. During this low tide two trace rainfall events occurred of less than 0.25 mm each for a maximum possible 0.5 mm. While its unlikely that the total rainfall was this high, this would still represent only half of the observed discharge.

5.4 Discussion

5.4.1 Dynamic separation of tidal versus post-ebb discharge flows

A simple description for steady open-channel flow is the Gauckler-Manning Equation (Gioia and Bombardelli, 2002),

$$\bar{v} = \frac{k}{n} R_h^{2/3} S_f^{1/2} \tag{5.7}$$

where $\bar{v}$ is the mean velocity (depth- and cross-sectionally averaged), n is the Gauckler-Manning coefficient indicating the roughness of the channel, R_h is the hydraulic radius (the ratio $\frac{A}{p}$ of the cross-sectional area A to the wetted channel perimeter p), k is a unit conversion factor equal to unity for SI units, and S_f is the friction slope, a function of the changing channel depth and the bed slope. This equation represents a balance between gravity (via slope) and friction (via roughness), assuming turbulent stress varies linearly as a function of distance to the channel boundary. Here, we use a Gauckler-Manning coefficient of $n = 0.02$ (a typical value for natural mud), unit conversion $k = 1$, a LiDAR-based estimate of R_h, and $\bar{v} = \mathcal{V}(t)/A(t)$ where $\mathcal{V}(t)$ is calculated as in section 5.3.3. The friction slope is then the only unknown variable.

The velocities $\bar{v}$ as a function of friction and hydraulic radius $nR_h^{-2/3}$ are shown in Fig. 5.8a, and the inferred friction slopes as a function of time in Fig. 5.8b. During

the ebb period (prior to 09:15), the flow is directly proportional to $nR_h^{-2/3}$. From 09:00 to 09:15, S_f increases until the post-ebb discharge period. This increase in slope is consistent with the receding tide controlling the downstream water elevation creating a backwater effect at the measurement location.

As the downstream tidal elevation falls, the friction slope approaches a near constant value of $S_0 = 0.005$ during the post-ebb discharge period. If the flow is uniform in depth along the channel, then bed slope S_0 is equivalent to the friction slope, i.e. $S_0 = S_f$ and under these conditions the velocity is inversely proportional to $nR_h^{-2/3}$ with the slope of the regression equivalent to $S_0^{1/2}$. During the post-ebb period (after 09:15), the observations are consistent with uniform open channel flow and with an inferred bed slope of $S_0 = 0.005$, consistent with nearby calculations of the actual channel slope by Mariotti and Fagherazzi (2011).

Following the post-ebb discharge period, the flood period shows a similar pattern to the ebb with $\bar{v}$ decreasing with $nR_h^{-2/3}$. The friction slope again decreases as the flooding tide increases downstream tidal elevations. It should be noted that while the velocities during the ebb and flood periods are influenced by the downstream tidal elevations they should still follow open-channel flow dynamics. In these situations, however, the flow depth is no longer uniform along the channel, nor is the flow steady. Instead, gradually varied flow dynamics would need to be considered and the friction slope would no longer be equivalent to the surface slope. Without precise measurements of the downstream elevations calculating the exact backwater conditions is difficult and beyond the scope of this experiment.

A simple schematic shown in Fig. 5.8 shows how the tidal flow influences the water elevation in the channel through the backwater effect of the downstream water

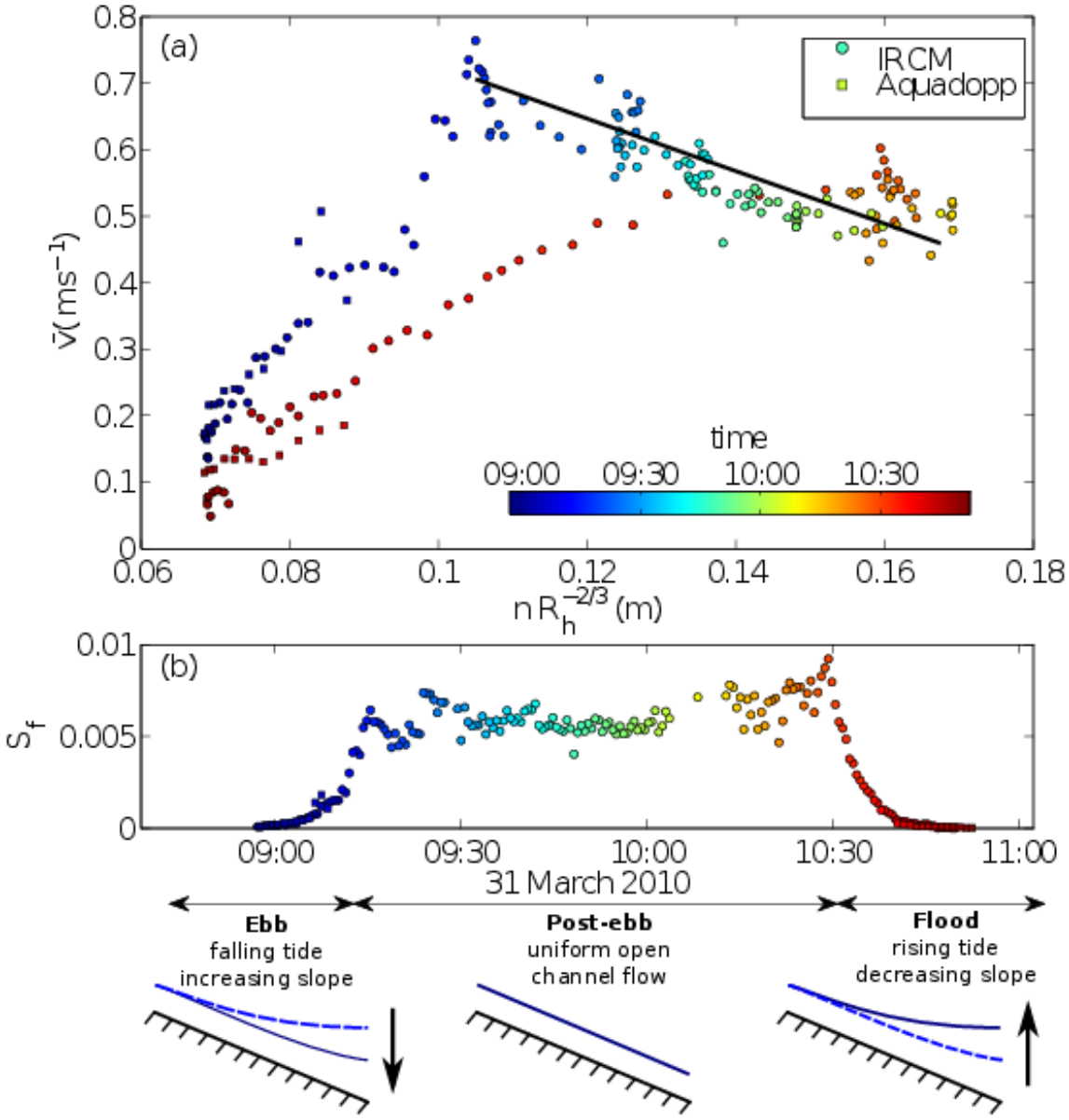

Figure 5.8 (a) Depth-mean velocity vs $nR_h^{-2/3}$ from the Aquadopp (circle) and IRCM (square) datasets. Color corresponds to observation time. The line is a best-fit line for Eq. 5.7 for the post-ebb discharge period (after 09:15). (b) Calculated dynamic slope S_f during the same time period and schematic diagrams of the channel and water depth showing the influence of tidal elevation on channel slope. The dashed lines indicate the prior tidal elevation with the arrows showing rising or falling tide. The falling tide increases the friction slope S_f while the rising tide decreases S_f. During the post-ebb period, water elevation is steady and uniform throughout the channel with $S_f = S_0$.

elevation. As the tide recedes, the downstream elevation falls and S_f increases due to the increase in the water surface slope. This occurs until uniform open channel flow is established where the flow depth is the same everywhere and the water slope matches the bed slope. When the tide rises again the downstream tidal elevation reduces S_f and decelerates the flow. Dynamically, the ebb and post-ebb flow regimes differ in the importance of the bed and surface slopes in controlling the pressure gradient forcing. During normal tidal flow, the varying tidal elevation creates a water surface slope and hence a pressure gradient driving the flow. During the post-ebb discharge, however, when the flow depth is uniform along the channel, bed friction is the main dynamic control on the pressure gradient.

5.4.2 Remnant water heat flux model

To further assess the hypothesis of remnant water on the flat surface as the source of post-ebb discharge in the channel, a heat-flux model is applied to predict the temperature of remnant water and then the predictions are compared with observed outflow temperatures. The model is necessary because remnant water temperatures on the flats were not measured directly, owing to the difficulties in measuring thin (O(1) mm) layers without disturbing the hydrodynamic system. Remnant water temperatures were not measured remotely, because the infrared field of view was too small to capture even a small fraction of the remnant water up on the flat.

Applying the model of Kim et al. (2010) and using the meteorological measurements, we estimate the near surface heat flux Q_{net} as

$$Q_{net} = Q_s + Q_l + Q_e + Q_h + Q_{mw} \tag{5.8}$$

where Q_s is net shortwave radiation, Q_l is net longwave radiation, Q_e is latent heat

flux due to evaporation and freezing, Q_h is sensible heat flux, and Q_{mw} represents heat exchange between the sediment and water column during inundation of the flats. The main source of heat is the net shortwave radiation $Q_s = (1 - \alpha)Q_{s0}$ where Q_{s0} is the incoming solar shortwave radiation and α is the albedo of the water surface. A constant albedo of $\alpha = 0.08$ was used for this model, consistent with prior heat modeling experiments (Guarini et al., 1997). Q_l, Q_e, and Q_h generally represent losses of heat and are empirical functions of local meteorological conditions, modeled following Kim et al. (2010).

The sediment temperatures with depth in the sediment bed were also modeled following Kim et al. (2010) using the one-dimensional heat conduction equation

$$\frac{\partial T_s}{\partial t} = \kappa \frac{\partial^2 T_s}{\partial z^2} \tag{5.9}$$

where $T_s(z)$ is the sediment temperature with depth in the sediment z and κ is the sediment heat diffusivity. Previous work by Thomson (2010) found sediment thermal diffusivities ranging from 0.2 - 0.7 $\cdot 10^{-6}$ $\mathrm{m^2 s^{-1}}$. For this model a constant diffusivity of $\kappa = 0.5 \cdot 10^{-6}$ $\mathrm{m^2 s^{-1}}$ was used. Sediment temperatures were modeled to 1 m depth and initialized using the sand anchor observations. No heat fluxes were assumed to occur through the bottom boundary, while heat fluxes through the sediment-water interface were modeled as

$$Q_{mw} = h_{sw} \left(T_s - T_w\right) \tag{5.10}$$

where T_s and T_w are the sediment and water temperatures respectively. h_{sw} is the sediment-water heat transfer coefficient, with a constant value of 20 $\mathrm{WK^{-1} m^{-2}}$ used for this study. Values from $10 - 70$ $\mathrm{WK^{-1} m^{-2}}$ were also tested and had little effect. This is likely due to the fact that the modeled locations were inundated during the entire time period allowing the sediment-water interface to come into a thermal equilibrium.

The temperature T of the remnant water that would be available to runoff into D channel is estimated using the net heat flux Q_{net} as a function of time t

$$\frac{\partial T(x,t)}{\partial t} = \frac{Q_{net}(t)}{C_v d}, \tag{5.11}$$

where C_v is the volumetric heat capacity of seawater, and d is the depth of the water. The final temperature predictions $T(x,t)$ were obtained by time-integrating Eq. 5.11 for all t after the ebb has passed at given x value (i.e., once the flats are exposed and remnant water is left on the surface of the flats at a given location).

The model was applied at 11 vertical locations on the flat from 1.5 - 2.5 m above the channel mouth elevation and the tidal elevation from the sand anchor pressure gauge at the Aquadopp site was used to determine water depths at the modeled locations. We assumed a remnant water thickness $d = 0.01$ m, based on visual observations during fieldwork, in order to simulate the remnant water on the flat surface when the tidal elevation was below the flat elevation. The model was started at 00:00 31 March 2010, during a period of inundation prior to the IRCM observations and initialized with observed water and sediment temperatures of 9.8 °C, which were in equilibrium.

The model results for temperature and the heat fluxes are shown in Figure 5.9. The heat flux terms for the mid-flat site (at 2 m above D Channel mouth elevation) are representative of the whole system and are presented in Figure 5.9b. At the mid-flat site, Q_{net} begins negative (predicting cooling of remnant water) and transitions to positive (predicting warming of remnant water) during the drainage period. The key term for cooling remnant surface water is the long wave (blackbody) radiation Q_l, although some of the lost heat is replaced by warming from the positive exchange with the underlying mud (which has a large thermal mass and maintains 9.8 °C throughout most of the model time series). The key term for heating is solar radiation Q_s, which

becomes dominant after 09:00 .

The resulting estimates of remnant water temperature at representative locations on the flats are shown in Figure 5.9. The upper, mid, and lower flat elevations are at 2.5 m, 2 m, and 1.5 m above the channel mouth elevation. Water on the upper flats initially cools under negative heat flux, then warms later when solar radiation increases. The mid and lower flat locations begin to cool later than the upper flat location, because they are exposed later. All locations begin warming together, largely driven by solar radiation, at 08:00.

The temperature signal in the channel is expected to lag the temperature signal of remnant water on the flats by the travel time required to reach the channel mouth. This lag will vary with flat location and runoff speed. Likely, the water in the channel is mostly remnant water from the nearest (and most recently exposed) portion of the flats. For the O(0.5 ms^{-1}) flows observed in the channel, the lag time over a distance of 100 m is only 200 s, which cannot be distinguished from Figure 5.9. Lacking direct observations of the runoff velocities on the flats and in the runnels, we use a simple instantaneous mean of the modeled remnant water from all locations and compare to the observed temperatures at the same time. During the post-ebb period that is our focus (09:15-10:15), the modeled remnant water temperatures are similar at all locations, so the choice of position and associated time lag is not significant to the overall inference that channel drainage temperature is consistent with predictions for the temperature of remnant surface water.

The overall trend of cooling and then warming closely matches the observed drainage temperatures in D channel, which are highly variable relative to the constant Bear River channel water temperatures or constant mud temperatures (see Fig.

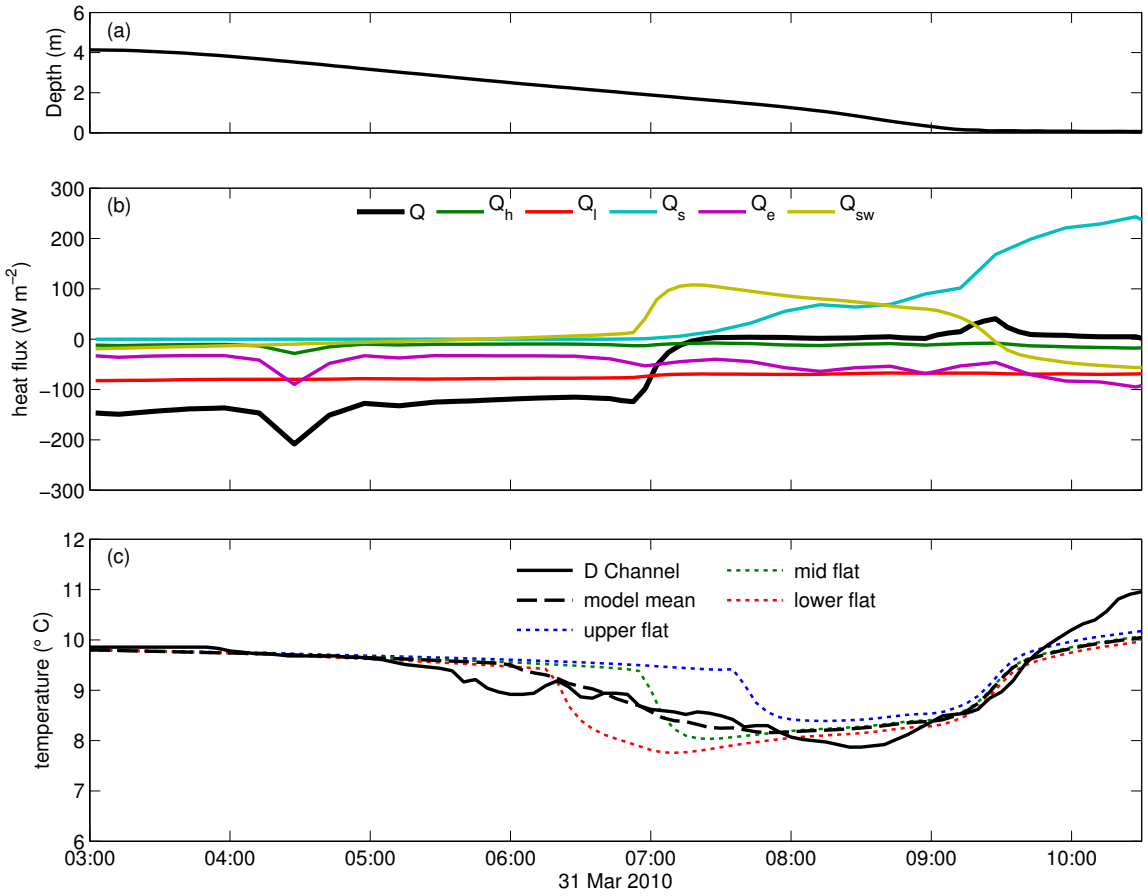

Figure 5.9 (a) Time series of water level, (b) terms in the heat flux model (colored lines), and (c) resulting predictions of remnant water temperatures at different locations on the flats. The mean from the model regions (dashed line) compares well with the measured temperature of water in D channel (solid line). The upper, mid, and lower flat are located at 2.5 m, 2 m, and 1.5 m above the D channel elevation.

5.3). If, instead, the channel drainage source was porewater, the drainage temperature would be closer to a constant 10.8 °C, which is the temperature observed from the buried (0.5 m) HOBO loggers within the mudflats. The heat flux model demonstrates that the temperature measurements are consistent with a thin film of water running off of the flats and undergoing the expected thermal changes associated with this runoff and eventual conveyance through D Channel.

5.5 Conclusions

Using a combination of in situ and remote measurements, we have quantified drainage in the channel of a natural tidal flat. The IRCM technique provides accurate measurements of surface velocity that compare well with in situ ADCP measurements. Parametric current profiles are fit to obtain estimates of volume flux along the channel, and the corresponding mean flows are assessed with the Gaukler-Manning equation. Temperature observations in the channel are consistent with predictions for the runoff of $\mathcal{O}(10^{-2}$ m) thick surface remnant water that cools after initial exposure and then warms via solar radiation.

The dynamics of the observed drainage were separated into two regimes: ebb tide and post-ebb discharge. The Manning-Gaukler equation for open channel flow accurately describes both of these regimes through variations in surface and bed slopes. During the ebb tidal flow, a decrease in tidal elevation causes an increasing water surface slope and thus increasing velocities. In the post-ebb discharge regime, flow is uniform (constant-depth) down a bed slope and velocity slowly decreases as water mass is lost from the flats. These results may be applied in future studies to estimate discharge in the absence of measurements.

Low tide discharge from mudflats is a mechanism for downstream transport of

material (and heat) that is often ignored, in part because it is difficult to measure. Although small, the long-term implication of this downstream transport may be significant in setting the morphology of the flat. Clearly, more study is necessary to understand the importance of post-ebb drainage. Future improvements would be to understand the spatial variability of remnant water on the flats, and to map pathways of the runoff through runnels and into channels. Additionally, detailed measurements of sediment concentrations during these periods would provide estimates of off-flat sediment flux.

Chapter 6

CONCLUSIONS AND OUTLOOK

This dissertation analyzed sediment and water column temperatures of tidal flats. Field observations of temperatures during summer and winter at Skagit Bay and Willapa Bay, WA, USA were reported. During the summer, sediment temperatures generally increase with daytime exposure of the tidal flats. Exposure during the winter causes decreases of the temperatures on the tidal flats. These observations were used to derive sediment thermal properties like diffusivity κ and a sediment-water heat exchange coefficient h_{sw}. Values for h_{sw} range from 5-20 W m^{-2} K^{-1} with the sandy Skagit Bay sites exhibiting slightly large values.

The field observations were then used to drive and test a cross-flat numerical model of tidal flat thermodynamics. The model results indicate that during July 2009, the sediment bed acted as a minor net source of heat at both study locations providing a total of 5 MJ m $^{-2}$ of heat energy to the water at Skagit Bay and 8 MJ m^{-2} at Willapa Bay. During the winter the sediment bed acted as a net sink, receiving 50 MJ m^{-2} of energy from the water at Skagit Bay and -11 MJ m^{-2} at Willapa Bay. Results at both locations were similar for each season, despite differences in diffusivity and conductivity at each site. The directionality of heat flux is based primarily on the phasing of maximum inundation and solar noon.

Processes during the flooding tide were then examined by phase-averaging the observational and modeled results. Alternate model runs were performed varying the

value of the light extinction coefficient from $K_d = 1$ m^{-1} to $K_d = 1000$ m^{-1} to simulate major variations in turbidity that would affect uptake of shortwave radiation. The high extinction coefficient runs were able to more accurately match the observational results of enhanced water column temperatures at the front edge indicating the importance of turbidity to the heat budget during these periods. When the model results are analyzed in a Lagrangian frame, heating at the edge of the front is found to be primarily due to solar radiation heating a thin layer of water at the front edge as opposed to heating by the sediment.

Finally ebb-tidal drainage was examined using a combination of in situ and remotely sensed observations in concert with the model. Despite the shallow flows, the IRCM provided accurate measurements of the surface velocities within the drainage channel. Volume fluxes were calculated and used to identify two dynamic regimes: the ebb tidal flow and post-ebb drainage. While both conditions represent open-channel flow, ebb-tidal friction velocities are influenced by the downstream elevations creating a backwater effect and decreasing the momentum fluxes. During the post-ebb drainage, however, uniform-depth open channel flow is maintained. Temperature observations in the channel were consistent with modeled results assuming surface runoff of water from atop the flat planform.

6.1 Sea level rise scenario

The conclusions of this dissertation raise interesting questions about tidal flat thermodynamics. The University of Washington Climate Impacts Group projects that local sea level rise due to anthropogenic climate change to be between 18 to 59 cm by the end of 2100 (Mote et al., 2008). They note however, that low-probability, high-impact scenarios should be taken into account when make long term decisions

and hence recommend using a local sea level rise of 55-120 cm for future scenarios. What would be the changes to tidal flat thermodynamics under these higher sea-level conditions?

As an example of what might happen during sea level rise, the cross-shore model was run for a sea level rise of 1 m simply by lowering the elevations at each location by 1 m. Figure 6.1 shows the results at Skagit Bay during the modeled July time period. The increase in sea level reduces the amount of flat area exposed and hence reverses the difference between the sediment and water temperatures in the middle portion of the flats. Water column temperatures from 1.25 to 3.75 km are now, on average, warmer than the sediment temperatures. This change also increase temperatures by about 1°C in the shallowest area of water and decreases sediment temperatures by a similar amount in the mid-flat region. The reversal in the difference between temperatures means that sediment-water heat exchanges are now reversed with the water column acting as a net source of heat to the sediment bed. This would be expected due to the reduction in the percentage of exposure that a location would experience.

During the winter, however, the changes are not as stark (Figure 6.2). The qualitative relationship remains the same with the sediment bed acting as a net heat sink. Temperatures at the shallower end of the flats are the most effective with about a 1°C difference in water temperatures at the up flat limit.

These results should, of course, be taken with some discretion, as a change in sea level would likely increas the accommodation space of the Skagit Delta and allow greater sedimentation to occur in the area of the flats, perhaps keeping up with sea level rise. Currently, most of the sediment carried by the Skagit River is deposited

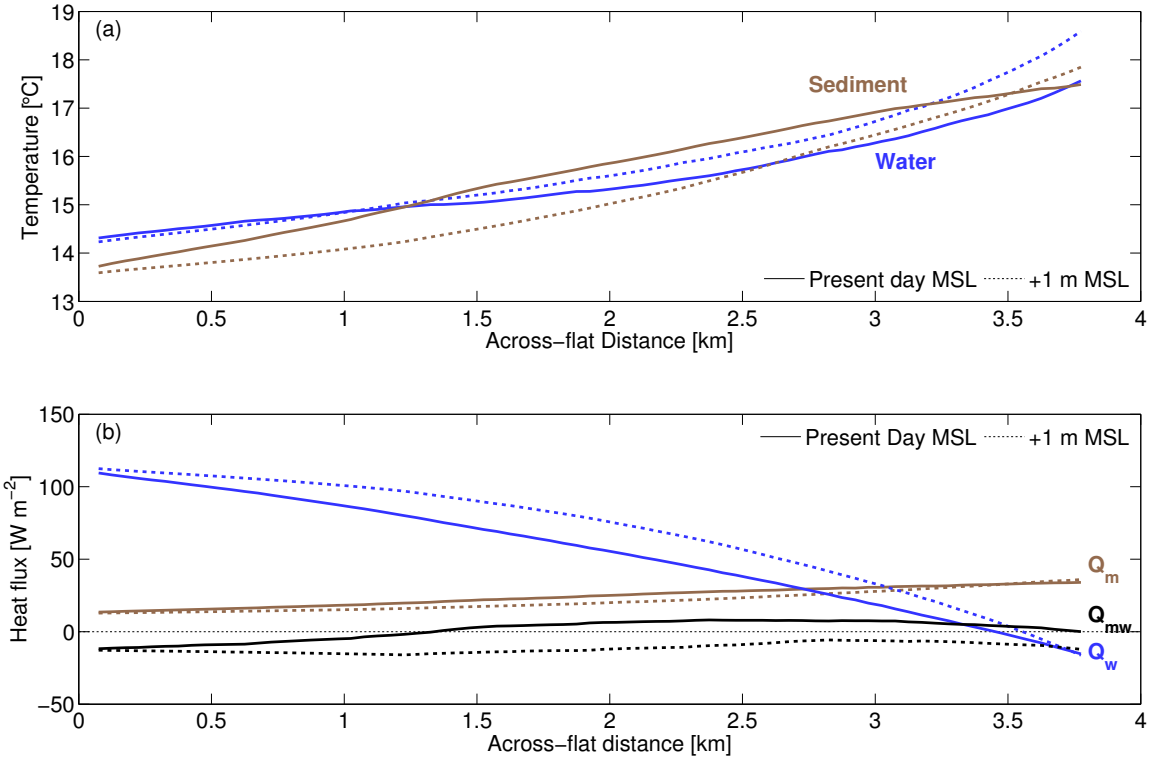

Figure 6.1 (a) Cross-flat profile of time-averaged (blue) water and (brown) sediment temperatures at Skagit Bay for 7-27 July. The solid lines are under the current bathymetry while the dotted lines assume a 1-m rise in sea level over 100 years. (b) Cross-flat profile of time-averaged (blue) total heat flux to the water (Q_w), (brown) total heat flux to the sediment surface Q_m, and (black) sediment-water heat flux Q_{mw}. Positive Q_{mw} indicates heat flux into the water column.

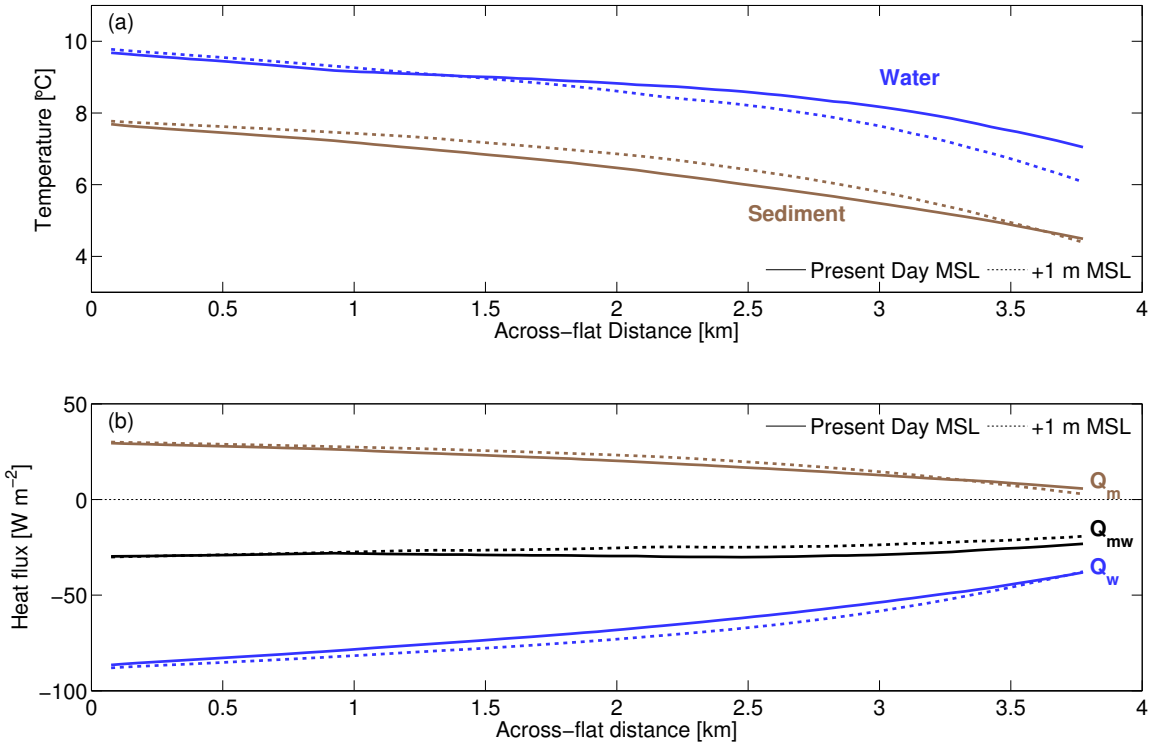

Figure 6.2 (a) Cross-flat profile of time-averaged (blue) water and (brown) sediment temperatures at Skagit Bay for 9-29 January. The solid lines are under the current bathymetry while the dotted lines assume a 1-m rise in sea level over 100 years. (b) Cross-flat profile of time-averaged (blue) total heat flux to the water (Q_w), (brown) total heat flux to the sediment surface Q_m, and (black) sediment-water heat flux Q_{mw}. Positive Q_{mw} indicates heat flux into the water column.

past the delta front in deep Whidbey Channel (Webster et al., 2012), but an increase in local sea level would allow some of that sediment to be deposited in the delta region with the increase in accommodation space. Of course sea level changes would likely also change the tidal curve as well. However, even considering these caveats, this "what-if" exercise provides an example of a system where the intertidal area has been greatly reduced and hence comparisons could be made with existing regions such as embayments where intertidal areas are smaller.

BIBLIOGRAPHY

Allen, J. R. L. (1985). Intertidal drainage and mass-movement processes in the Severn Estuary: rills and creeks (pills). *Journal of the Geological Society*, 142(5):849–861.

Amos, C. L. (1995). Siliclastic tidal flats. In Perillo, G. M. E., editor, *Geomorphology and Sedimentology of Estuaries*, pages 273–306. Elsevier, Amsterdam.

Anderson, F. and Howell, B. (1984). Dewatering of an unvegetated muddy tidal flat during exposure—Desiccation or drainage? *Estuaries*, 7(3):225–232.

Andrews, R. (1965). Modern sediments of Willapa Bay, Washington: A coastal plain estuary. Technical report, University of Washington.

Ashley, G. M. and Zeff, M. L. (1988). Tidal channel classification for a low-mesotidal salt marsh. *Marine Geology*, 82(1-2):17–32.

Banas, N., Hickey, B., MacCready, P., and Newton, J. (2004). Dynamics of Willapa Bay, Washington: A highly unsteady, partially mixed estuary. *J. Phys. Oceanogr.*, 34(11):2413–2427.

Bignami, F., Marullo, S., Santoleri, R., and Schiano, M. (1995). Longwave radiation budget in the Mediterranean Sea. *J. Geophys. Res.*, 100(C2):2501–2514.

Boldt, K. V., Nittrouer, C. A., and Ogston, A. S. (2013). Seasonal transfer and net accumulation of fine sediment on a muddy tidal flat: Willapa Bay, Washington. *Continental Shelf Research*.

Brunt, D. (1932). Notes on radiation in the atmosphere. I. *Q.J.R. Meteorol. Soc.*, 58(247):389–420.

Brutsaert, W. (2005). *Hydrology: An Introduction*. Cambridge Univ Press.

Cahill, B., Schofield, O., Chant, R., Wilkin, J., Hunter, E., Glenn, S., and Bissett, P. (2008). Dynamics of turbid buoyant plumes and the feedbacks on near-shore biogeochemistry and physics. *Geophys. Res. Lett.*, 35(10):L10605.

Campbell, G. S. and Norman, J. M. (1998). *An Introduction to Environmental Biophysics*. Springer, New York.

Chickadel, C. C. (2003). An optical technique for the measurement of longshore currents. *J. Geophys. Res.*, 108(C11):3364–.

Cho, Y.-K., Kim, M.-O., and Kim, B.-C. (2000). Sea fog around the Korean Peninsula. *Journal of Applied Meteorology*, 39(12):2473–2479.

Colijn, F. and de Jonge, V. (1984). Primary production of microphytobenthos in the Ems-Dollard Estuary. *Marine Ecology Progress Series*, 14(2):185–196.

Fagherazzi, S. and Mariotti, G. (2012). Mudflat runnels: Evidence and importance of very shallow flows in intertidal morphodynamics. *Geophys. Res. Lett.*, 39(14).

Friedrichs, C. T. (2012). Tidal flat morphodynamics: A synthesis. *Treatise on Estuarine and Coastal Science*, 3.

Gioia, G. and Bombardelli, F. (2002). Scaling and similarity in rough channel flows. *Phys. Rev. Lett.*, 88(1):6465.

Gouleau, D., Jouanneau, J., Weber, O., and Sauriau, P. (2000). Short-and long-term sedimentation on Montportail-Brouage intertidal mudflat, Marennes-Oleron Bay (France). *Continental Shelf Research*, 20(12-13):1513–1530.

Guarini, J., Blanchard, G., Gros, P., and Harrison, S. (1997). Modelling the mud surface temperature on intertidal flats to investigate the spatio-temporal dynamics of the benthic microalgal photosynthetic capacity. *Marine Ecology Progress Series*, 153:25–36.

Gutiérrez, J. and Iribarne, O. (2004). Conditional responses of organisms to habitat structure: an example from intertidal mudflats. *Oecologia*, 139(4):572–582.

Harrison, S. (1985). Heat exchanges in muddy intertidal sediments: Chichester harbour, West Sussex, England. *Estuarine, Coastal and Shelf Science*, 20(4):477–490.

Harrison, S. and Phizacklea, A. (1987). Temperature Fluctuation in Muddy Intertidal Sediments, Forth Estuary, Scotland. *Estuarine, Coastal and Shelf Science*, 24:279–288.

Holland, K., Holman, R., Lippmann, T., Stanley, J., and Plant, N. (1997). Practical use of video imagery in nearshore oceanographic field studies. *Oceanic Engineering, IEEE Journal of*, 22(1):81–92.

Incropera, F. P. and DeWitt, D. P. (2002). *Introduction to Heat Transfer*. John Wiley & Sons, New York, 4th edition.

Jerlov, N. G. (1976). *Marine Optics*. Elsevier, Amsterdam.

Johnson, R. G. (1965). Temperature variation in the infaunal environment of a sand flat. *Limnology and oceanography*, pages 114–120.

Jones, P. and McGilchrist, C. (1978). Analysis of hydrological recession curves. *Journal of Hydrology*, 36(3):365–374.

Kim, T.-W. and Cho, Y.-K. (2009). Heat flux across the surface of a macrotidal flat in southwest Korea. *J. Geophys. Res.*, 114(C7).

Kim, T.-W. and Cho, Y.-K. (2011). Calculation of heat flux in a macrotidal flat using FVCOM. *J. Geophys. Res.*, 116.

Kim, T.-W., Cho, Y.-K., and Dever, E. P. (2007). An evaluation of the thermal properties and albedo of a macrotidal flat. *J. Geophys. Res.*, 112.

Kim, T.-W., Cho, Y.-K., You, K.-W., and Jung, K. T. (2010). Effect of tidal flat on seawater temperature variation in the southwest coast of Korea. *J. Geophys. Res.*, 115.

Kleinhans, M. G., Schuurman, F., Bakx, W., and Markies, H. (2009). Meandering channel dynamics in highly cohesive sediment on an intertidal mud flat in the Westerschelde estuary, the Netherlands. *Geomorphology*, 105(3-4):261–276.

Le Hir, P., Roberts, W., Cazaillet, O., Christie, M., Bassoullet, P., and Bacher, C. (2000). Characterization of intertidal flat hydrodynamics. *Continental Shelf Research*, 20(12-13):1433–1459.

Losordo, T. M. and Piedrahita, R. H. (1991). Modelling temperature variation and thermal stratification in shallow aquaculture ponds. *Ecological modelling*, 54(3-4):189–226.

Lovell, M. A. (1985). Thermal conductivity and permeability assessment by electrical resistivity measurements in marine sediments. *Marine Geotechnology*, 6(2):205–240.

Mariotti, G. and Fagherazzi, S. (2011). Asymmetric fluxes of water and sediments in a mesotidal mudflat channel. *Continental Shelf Research*, 31(1):23–36.

May, P. W. (1986). A brief explanation of Mediterranean heat and momentum flux calculations. Technical Report NORDA Code 322, NSTL Station, Miss.

McBride, A., Wolf, K., and Beamer, E. (2006). Skagit Bay nearshore habitat mapping. *Skagit River System Cooperative, LaConner, WA*.

Miselis, J. L., Holland, K. T., Reed, A. H., and Abelev, A. (2012). Use of vertical temperature gradients for prediction of tidal flat sediment characteristics. *J. Geophys. Res.*, 117(C3).

Mote, P., Petersen, A., Reeder, S., Shipman, H., and Binder, L. W. (2008). Sea Level Rise in the Coastal Waters of Washington State. Technical report, University of Washington.

Nowacki, D. J. and Ogston, A. S. (2012). Water and sediment transport of channel-flat systems in a mesotidal mudflat: Willapa Bay, Washington. *Continental Shelf Research*, in press:1–51.

O'Brien, D., Whitehouse, R., and Cramp, A. (2000). The cyclic development of a macrotidal mudflat on varying timescales. *Continental Shelf Research*, 20(12-13):1593–1619.

Onken, R., Callies, U., Vaessen, B., and Riethmüller, R. (2007). Indirect determination of the heat budget of tidal flats. *Continental Shelf Research*, 27(12):1656–1676.

Pavel, V., Raubenheimer, B., and Elgar, S. (2012). Processes controlling stratification on the northern Skagit Bay tidal flats. *Continental Shelf Research*, pages 1–10.

Peterson, C., Scheidegger, K., Komar, P., and Niem, W. (1984). Sediment composition and hydrography in six high-gradient estuaries of the northwestern United States. *Journal of Sedimentary Research*, 54(1):86–97.

Piccolo, M. C., Perillo, G. M. E., and Daborn, G. R. (1993). Soil temperature variations on a tidal flat in Minas Basin, Bay of Fundy, Canada. *Estuarine, Coastal and Shelf Science*, 36(4):345–357.

Press, W. H., Teukolsky, S. A., and Vetterling, W. T. (2007). *Numerical Recipes*. The Art of Scientific Computing. Cambridge University Press, 3rd edition.

Ralston, D. and Stacey, M. (2005). Stratification and turbulence in subtidal channels through intertidal mudflats. *J. Geophys. Res.*, 110:C08009.

Ralston, D. and Stacey, M. (2007). Tidal and meteorological forcing of sediment transport in tributary mudflat channels. *Continental Shelf Research*, 27(10-11):1510–1527.

Rinehimer, J. P. and Thomson, J. M. (2013). Seasonal and tidal variations of heat fluxes on tidal flats. *Submitted to Journal of Geophysical Research*.

Rinehimer, J. P., Thomson, J. M., and Chickadel, C. C. (2013). Thermal observations of drainage from a mud flat. *Continental Shelf Research*, pages 1–11.

Stefan, H. G., Cardoni, J. J., Schiebe, F. R., and Cooper, C. M. (1983). Model of light penetration in a turbid lake. *Water Resources Research*, 19(1):109–120.

Thomson, J. M. (2010). Observations of thermal diffusivity and a relation to the porosity of tidal flat sediments. *J. Geophys. Res.*, 115(C5).

Thomson, J. M. and Jessup, A. (2009). A Fourier-based method for the distribution of breaking crests from video observations. *Journal of Atmospheric and Oceanic Technology*, 26(8):1663–1671.

Uncles, R. J. and Stephens, J. (2011). The Effects of Wind, Runoff and Tides on Salinity in a Strongly Tidal Sub-estuary. *Estuaries and Coasts*, 34(4):758–774.

Webster, K. L., Ogston, A. S., and Nittrouer, C. A. (2012). Delivery, reworking and export of fine-grained sediment across the sandy Skagit River tidal flats. *Continental Shelf Research*, pages 1–13.

Wells, J., Adams Jr, C., Park, Y., and Frankenberg, E. (1990). Morphology, sedimentology and tidal channel processes on a high-tide-range mudflat, west coast of South Korea. *Marine Geology*, 95(2):111–130.

Whitehouse, R., Bassoullet, P., Dyer, K., Mitchener, H., and Roberts, W. (2000). The influence of bedforms on flow and sediment transport over intertidal mudflats. *Continental Shelf Research*, 20(10-11):1099–1124.

Wood, R. G., Black, K. S., and Jago, C. F. (1998). Measurements and preliminary modelling of current velocity over an intertidal mudflat, Humber estuary, UK. *Geological Society, London, Special Publications*, 139(1):167–175.

Yanagi, T., Sugimatsu, K., Shibaki, H., Shin, H.-R., and Kim, H.-S. (2005). Effect of tidal flat on the thermal effluent dispersion from a power plant. *J. Geophys. Res.*, 110(C3):C03025.